UNIVERSITY OF CALIFORNIA,
IRVINE

Molecular Design and Synthesis of Ligand-to-Ligand Charge-Transfer Complexes of Ni(II) and Ru(II) Using Redox-Active Ligands

DISSERTATION

submitted in partial satisfaction of the requirements
for the degree of

DOCTOR OF PHILOSOPHY

in Chemistry

by

Lindsay Ann Cameron

Dissertation Committee:
Professor Alan F. Heyduk, Chair
Professor Andrew S. Borovik
Professor Jenny Y. Yang

2017

DEDICATION

To

My Mom, Avery, Isaac, Harper, Caleb,
Otis, and Mini

TABLE OF CONTENTS

LIST OF FIGURES

LIST OF TABLES

LIST OF SCHEMES

LIST OF CHARTS

ACKNOWLEDGEMENTS

There is a long list of people I would like to acknowledge each playing a critical role in my journey to this moment. Thank you Palermo, for being Palermo. Mike and Terry Mueller, my employers during my post-bac, thank you for all your encouragement, acting as my surrogate parents, and giving me the freedom (with income) to focus on my studies. Dr. Michael Nantz, thank you for inspiring me through organic chemistry; Dr. Chris Burns, thank you for pushing me to apply out of state; the Disability Resource Center at UofL, thank you for giving me a safe place; Professor Aaron Esser-Khan, thank you for being my advocate; Professor Andy Borovik thank you for seeing me and accepting me; Professor Alan Heyduk, thank you for seeing me and challenging me; Dr. Wes Kramer, Dr. Janice Wong, Dr. Elaine Seraya, and Dr. Aaron Hollas thank you for your support and comradery; Dr. Afshin Pourezza thank you for helping me to see; Vince, thank you for giving me a boat home; and finally, Mini and Otis, thank you for being a part of my team!

CURRICULUM VITAE

Lindsay Ann Cameron

Education

University of California - Irvine, Irvine, California
PhD, Chemistry, 2017
PhD Dissertation: *Molecular Design and Synthesis of Ligand-to-Ligand Charge- Transfer Complexes of Ni(II) and Ru(II) Using Redox-Active Ligands.*

University of Louisville, Louisville, Kentucky
Post baccalaureate, Chemistry, 2012

University of Louisville, Louisville, Kentucky
Bachelor of Fine Arts, Photography; Minor, Art History, 2005

Research Experience

University of California - Irvine, Irvine, California,
Graduate Research Advisor: Professor Alan F. Heyduk, PhD.

- Conducted discovery and end use analysis to design molecular light harvesters for early-stage solar energy conversion research.
- Designed, implemented, and optimized synthetic processes to synthesize redox-active ligands and transition metal coordination compounds to enable the above research.
- Mastered air/moisture-free and inert atmosphere methods in order to synthesize, manipulate, and study non-innocent coordination compounds. This includes Schlenk line, high vacuum line, and glove box techniques.
- Elucidated complicated electronic and molecular structures using a broad range of analytical techniques: absorption, emission, and fluorescence spectroscopies; cyclic and differential pulse voltammetry; density functional theory (DFT); nuclear magnetic resonance (NMR) and electron paramagnetic resonance (EPR) spectroscopies; and X-ray crystallography.
- Collected, analyzed, and communicated complex data results to a wide range of audiences from PhD scientist panels and industry professionals to high school students.
- Mentored and advised undergraduate and junior graduate members on designing experiments, performing lab techniques, analyzing, organizing, and presenting data.
- Maintained laboratory equipment including glove boxes, vacuum pumps, and solvents systems.
- Managed chemical and supply inventory in the laboratory.
- Interacted with sales representatives to negotiate best prices for chemicals, equipment, and supplies.

Publications

1. **Lindsay A. Cameron**, Joseph W. Ziller, and Alan F. Heyduk, "Donor-Acceptor Complexes of Ru(II) Using Redox-Active Ligands" **2017**, *manuscript in preparation.*
2. **Lindsay A. Cameron**, Joseph W. Ziller, and Alan F. Heyduk, "Near-IR absorbing donor–acceptor ligand-to- ligand charge-transfer complexes of nickel(II)" Chemical Science, **2016**, 7, 1807-1814.
3. **Lindsay A. Cameron** and Alan F. Heyduk, "Redox-Active Ligands" AccessScience, McGraw-Hill Education, **2015**.
4. Wesley W. Kramer, **Lindsay A. Cameron**, Ryan A. Zarkesh, Joseph W. Ziller, and Alan F. Heyduk,"Donor–Acceptor Ligand-to-Ligand Charge-transfer complexes of nickel(II)" Inorganic Chemistry, **2014**, 53 (16), pp 8825–8837.

Presented Works

Lindsay A. Cameron and Alan F. Heyduk, "Exploring Ligand-to-Ligand Charge-Transfer (LL′CT) Transitions of Ni(II) Coordination Complexes", ACS National Meeting, San Diego, 2016 (*Oral Communication*).

Lindsay A. Cameron and Alan F. Heyduk, "Using Redox-Active Ligands to Design New Charge-Transfer Dyes Based on the (donor)Ni^{II}(acceptor) Motif", Southern California Inorganic Photochemistry Conference, Catalina Island, CA, 2014 (*Oral Communication*).

Lindsay A. Cameron and Alan F. Heyduk, "Using Redox-Active Ligands to Design New Charge-Transfer Dyes Based on the (donor)Ni^{II}(acceptor) Motif", ACS National Meeting, San Francisco, 2014 (*Oral Communication*).

Lindsay A. Cameron and Alan F. Heyduk, "Designing New (donor)M(acceptor) Dyes", Southern California Inorganic Photochemistry Conference, Catalina Island, CA, 2013 (*Oral Communication*).

Teaching Experience

University of California - Irvine, Department of Chemistry

- Teaching Assistant *(Laboratory),* Advanced Inorganic Lab 2017;
- Head Teaching Assistant *(Lecture),* Graduate Inorganic Spectroscopy, 2017, S 2015;
- Head Teaching Assistant *(Lecture),* Honors General Chemistry, 2014, 2015;
- Head Teaching Assistant *(Lecture),* General Chemistry, 2015;
- Teaching Assistant *(Lecture),* General Chemistry, 2012, 2014, and 2016;
- Teaching Assistant *(Lecture),* Inorganic Chemistry, 2013;
- Teaching Assistant *(Laboratory),* General Chemistry Lab, 2013.

Professional Experience

Wound Partners, LLC Louisville, KY **2007-2012**

Office Manager: Repeatedly promoted during tenure with Wound Partners, culminating in responsibilities for coordinating all office functions and supervising a team of five administrative professionals.

- Managed schedules, organized office functions, and oversaw daily operations of office.
- Developed efficiency-enhancing workflow/process improvements that made it possible to accommodate increasing responsibilities necessitated by staff reductions.
- Oversaw all accounting transactions including Payroll.

Palermo Viejo Restaurant Louisville, KY **2002-2007**

Front of House Manager; Head Server

- Managerial responsibilities included recruiting, hiring, training and the supervision of 10+ employees.

Honors and Awards

- Public Impact Fellow, University of California, 2014;
- Orange County American Chemical Society, High School Awards Dinner, Keynote Speaker, 2015;
- Michael E. Gebel Award – Recipient, University of California, 2014;
- STEMS Undergraduate Teaching Fellowship – Recipient, University of Louisville, 2012;
- New Beginnings Scholarship – Recipient, University of Louisville, 2010–2012;
- Sister Cities of Louisville Tamale, Ghana Scholarship – Recipient, University of Louisville, 2007.

ABSTRACT OF THE DISSERTATION

Molecular Design and Synthesis of Ligand-to-Ligand Charge-Transfer Complexes of Ni(II) and Ru(II) Using Redox-Active Ligands

By

Lindsay Ann Cameron

Doctor of Philosophy in Chemistry

University of California, Irvine, 2017

Professor Alan F. Heyduk, Chair

The work described in this dissertation focuses on the rationale behind the design and synthesis of ligand-to-ligand (LL′CT) charge-transfer chromophores supported by redox-active ligands. The molecular chromophores reported herein are meant to interest scientists in materials chemistry, physics, and chemical engineering that wish to employ molecular photosensitizers in photovoltaics and/or in artificial photosynthetic systems.

Chapter 1 provides background information on redox-active ligands, their role in non-innocent coordination compounds, the importance of photo-induced excited-states, and demonstrates the ability to tune excited-state properties through molecular design.

Chapter 2 introduces four Ni(II) square-planar LL′ CT chromophores that are a part of a larger group of square-planar Ni(II) complexes originally published together. These complexes posses HOMO and LUMO orbitals that are localized on the redox-active ligands and that their energies can be controlled independently through chemical modification to the catecholate donor and diimine acceptor.

Chapter 3 describes new Ni(II) square-planar donor-acceptor (D-A) chromophores designed absorb near-IR photons and access excited-state oxidation potentials capable of electron injection into metal oxide (semiconductor) surfaces. Bipyridyl-type acceptor ligands are employed to maintain a LUMO at high energy. Incorporation of the strongly

reducing amidophenolate donor ligand is meant to destabilize the HOMO energy and push the LL'CT absorption into the NIR (λ_{max}: 890 and 970 nm). According to the electro- and spectrochemical data the (amidophenolate)Ni(acceptor) dyes reported in herein are estimated to access excited-state oxidation potentials potent enough to populate the conduction band of TiO_2 (-0.7 V vs. SCE).

Chapter 4 details the investigation of two square-planar Ni(II) D-A LL′CT dyes from Chapter 3 that are equipped with carboxyl anchoring groups for tethering to metal oxide surfaces. Upon optical excitation, the dyes reported herein maintain their excited-state reductive potency. Preliminary binding studies on TiO_2 thin films suggest successful dye adsorption but film degradation occurred once exposed to air. Although the air sensitivity of the dye-functionalized film is problematic, future precautions such as air-free studies can be made in order to test their efficacy to inject electrons into large band gap semiconductors.

Chapter 5 introduces and investigates three six-coordinate D-A Ru(II) charge-transfer dyes with the general formula: (donor)Ru($N_2N_2^q$) [donor = 2 Cl^-, $(catB_4)^{2-}$ and $(cat)^{2-}$]. The co-planar arrangement of donor and acceptor orbitals was achieved through the use of the tetradentate, redox-active, N,N'-bis-(3-dimethylaminopropyl)-4,5-dimethoxy-benzene-1,2-diiminoquinone, ($N_2N_2^q$). These new octahedral D-A Ru(II) charge-transfer complexes demonstrate that the tetradentate $N_2N_2^q$ acceptor ligand, when coordinated to a d^6 metal ion, allows for the co-planar installation of redox-active donor ligand. Furthermore, the lowest energy transitions of the complexes reported herein are heavily dependent on the identity of the donor ligand, suggesting it is LL′CT in nature. Thus far, our findings suggest that the optical and ground-state redox properties of dyes based on a d^6 metal ion and the $N_2N_2^q$ ligand can be tuned through ligand modification. This may open up new areas of research where, instead of a precious heavy metal, such as ruthenium, the earth abundant Fe(II) ion could be used to realize a truly robust and tunable earth abundant charge-transfer photosensitizer.

Chapter 1

Introduction

1.1 Redox-Active Ligands

Oxidation–reduction (redox) reactions are a fundamental type of chemical reaction that is critical to the bond-making and bond-breaking events that drive almost all chemical transformations.[1,2] In nature, many reactions that are important to life are multi-electron redox reactions. For example, in land plants, sunlight is stored in chemical bonds by photosynthesis, which splits water into O_2 and H_2 as NADPH (nicotinamide adenine dinucleotide phosphate) via a four-electron process.[3] The reverse process, respiration, uses O_2 and four electrons to synthesize ATP as an energy source in cells.[4] Nitrogen fixation (ammonia synthesis)[5], C–H bond functionalization[6], and CO_2 reduction[7] are all multi-electron redox reactions carried out in nature, and each of these processes is facilitated by enzymes that contain first row transition metals such as Mn, Fe, Co, Ni, Cu, and Zn. Because first row transition metals typically react by one-electron pathways, nature often includes redox-active cofactors to expand their reactivity to allow these important multi-electron processes to occur.[8,9] In synthetic inorganic chemistry, transition metal coordination compounds equipped with redox-active ligands can be used to achieve the same goal: enable multi-electron reactivity with a metal ion that is prone to one-electron pathways.[1,10] In inorganic photochemistry, redox-active ligands play a critical role in photo-induced electron transfer reactions because, in many cases, at least one of the photo-active frontier molecular orbitals (pFMOs) is localized on the ligand.[11] This association gives them a particular importance towards the realization of sustainable solar energy conversion strategies whereby multi-electron processes are required to transform greenhouse gasses and other stable molecules (e.g. H_2O and CO_2) into energy-rich fossil-fuel surrogates.[12-16]

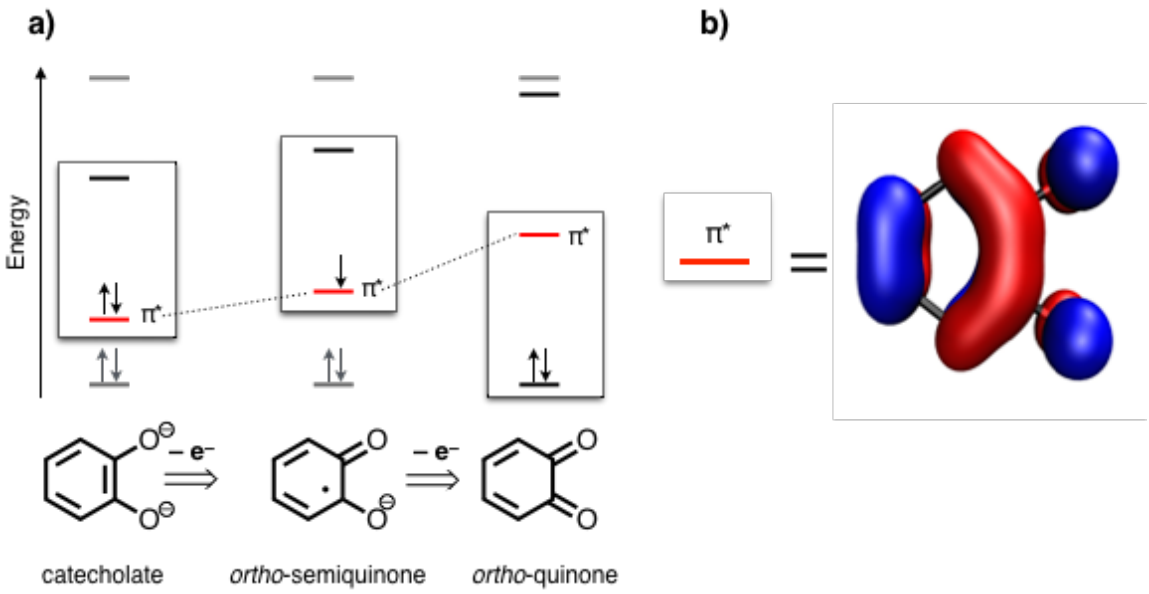

Figure 1.1 a) Lewis structures and frontier molecular orbital diagrams of the available oxidation states of the dioxolene class of redox-active ligands and b) Pov-Ray rendering of the π* molecular orbital.

Just as transition metals can change oxidation state by the addition or removal electrons, redox-active ligands can change oxidation state when coordinated to a metal ion.[1,10,17-19] Perhaps the archetypical redox-active ligand set is that of dioxolene family, where dioxolene represents a benzene-1,2-oxo ligand in one of three possible oxidation states: $[catecholate]^{2-}$, $[semiquinonate]^{-}$, and quinone.[20-22] Lewis structures of the accessible oxidation states of the dioxolene family are shown in **Figure 1.1a**. The ability of dioxolene-type ligands and other like it to access multiple redox isomers can be rationalized by inspection of their frontier molecular structures. According to the Kohn–Sham molecular orbital diagrams in **Figure 1.1a**, the HOMO (Highest Occupied Molecular Orbital) of the $[catecholate]^{2-}$ ligand has both π and π* character. Removal of one electron from this orbital produces the radical [*ortho*-semiquinonate]$^{-}$ ligand. Removal of the second electron from this orbital produces the *ortho*-quinone ligand. Thus, as illustrated by the Pov-Ray

rendering in **Figure 1.1b**, the HOMO of [catecholate]$^{-2}$ is the LUMO of the *ortho*-quinone ligand. Moreover, changing the electron count of a redox-active orbital does not cause significant structural changes to the ligand itself. For example, across the catecholate/semiquinonate/quinone series, the hybridization of the carbon atoms do not change with changes to the oxidation state. In principle, the structural uniformity that is maintained across the redox series enables transitions between each oxidation state to be reversible and each isomer isolable when bound to a transition metal ion.[20,23]

Chart 1-1 Common redox-active ligand motifs.

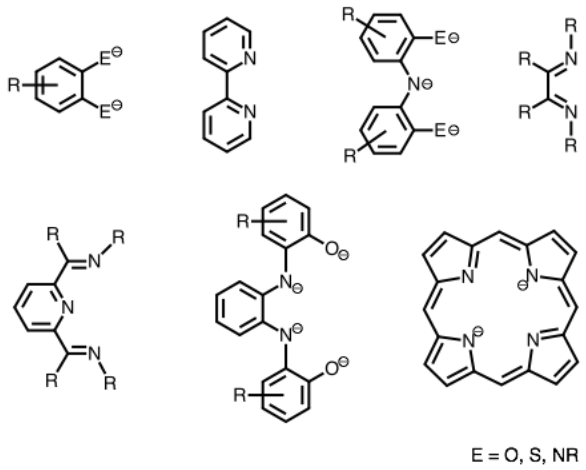

Redox-active ligands are usually derived from catecholate or α-diimine fragments and some common examples are shown in **Chart 1.1.** Bidentate, tridentate, and tetradentate redox-active ligands can be constructed by combining multiple catecholate, amidophenolate, or α-diimine fragments into a single ligand.[24-26] Their structural versatility can be leveraged to achieve a desired coordination environment or structural arrangement. Additionally, the electronic structure can be manipulated through incorporation of different heteroatoms and/or variation of the R groups to achieve desired electronic properties. [27]

1.2 Redox-Active Ligands in Non-innocent Coordination Complexes

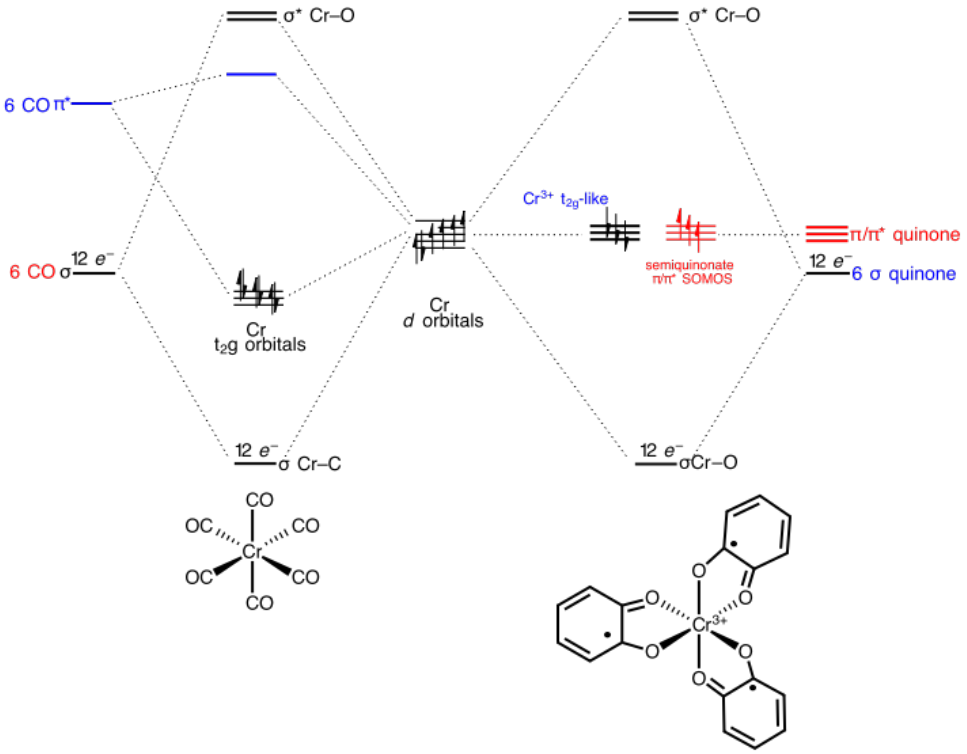

Figure 1.2 Frontier molecular orbital diagrams of $CrCO_6$ and Cr(sq)$^{2-}$ reproduced from Ref: *J. Phys. Chem.* **1992**, *96* (5), 2129–2141.

Coordination compounds that contain redox-active ligands are often described as 'non-innocent', where assignment of the metal oxidation state is not obvious and often determined experimentally. [28] "Non-innocence" in coordination chemistry is observed when the frontier orbitals of a redox-active ligand are spatially proximate and energetically similar to the frontier d orbitals of the transition metal. An example of this is shown in **Figure 1.2** which compares the molecular orbital diagrams of two chromium complexes, $Cr(CO)_6$ and Cr(semiquinonate)$_3$. [29,30] Assignment of the metal oxidation state for $Cr(CO)_6$ is straightforward. Carbon monoxide is a neutral, "L-type" ligand with the empty CO π* orbitals energetically isolated from the filled t_2g-like orbitals of the octahedral chromium

center. Thus, the homoleptic hexacarbonyl complex is best described as neutral with a d^6 chromium(0) center.[31] The Cr(semiquinonate)$_3$ is prepared by the reaction between $Cr(CO)_6$ and three ortho-quinones that proceeds with a color change from the pale yellow of the hexacarbonyl starting material to the dark red-purple of the product. [32] The product has the stoichiometry of one chromium atom to three dioxolene ligands and can take on multiple oxidation state descriptions. Two obvious assignments would be Cr^0(quinone)$_3$, where the metal maintains a d^6 electron count and all three ligands stay in the quinone oxidation state; or Cr^{VI}(catecholate)$_3$, where the metal is oxidized to a d^0 ion and all three ligands are reduced to the [catecholate]$^{-2}$ oxidation state. The experimental data suggests the formation of Cr^{III}(semiquinonate)$_3$, where chromium(0) is oxidized to chromium(III) and the three *ortho*-quinone ligands are reduced by one electron to the [*ortho*-semiquinoate]. Evaluation of the experimentally observed intraligand bond distances in the crystal structure confirmed the latter assignment and displayed an average C-O bond lengths of 1.30 Å, which is intermediate between those of coordinated catecholates (1.36 Å) and quinones (1.22 Å). Quinoid-type distortion of the six-membered carbon rings was also observed by showing two alternating short C=C bonds (1.33 and 1.36 Å) and four longer C–C single bonds (average 1.45 Å). Finally, Density Functional Theory calculations helped elucidate the frontier electronic structure illustrated in **Figure 1.2**: three [*ortho*-semiquinoate]$^-$ ligand π radicals (S_{rad} = ½), antiferromagnetically coupled to a central chromium(III) ion (S_{Cr} = 3/2), generating the overall diamagnetic ground state (S = 0). [33]

Traditionally, chemists have relied on precious metals, such as platinum and rhodium, to catalyze bond-making and bond-breaking transformations, as they are predisposed to multi-electron reactivity.[34-36] More recent efforts have aimed to replace

these precious metals with less expensive, earth abundant metals.[17,26,37,38] Drawing inspiration from nature, redox-active ligands have been incorporated into coordination complexes with earth abundant metal ions in an effort to realize multi-electron redox reactivity in both stoichiometric and catalytic processes.[1,10,39,40] In photochemical processes, redox-active ligands can play a critical role in photo-induced electron transfer reactions, because at least one of the photo-active frontier molecular orbitals (pFMOs) is usually localized on a redox-active ligand.[11,41-44] A classical example of this is the $Ru(bpy)_3^{2+}$ family of photosensitizers.

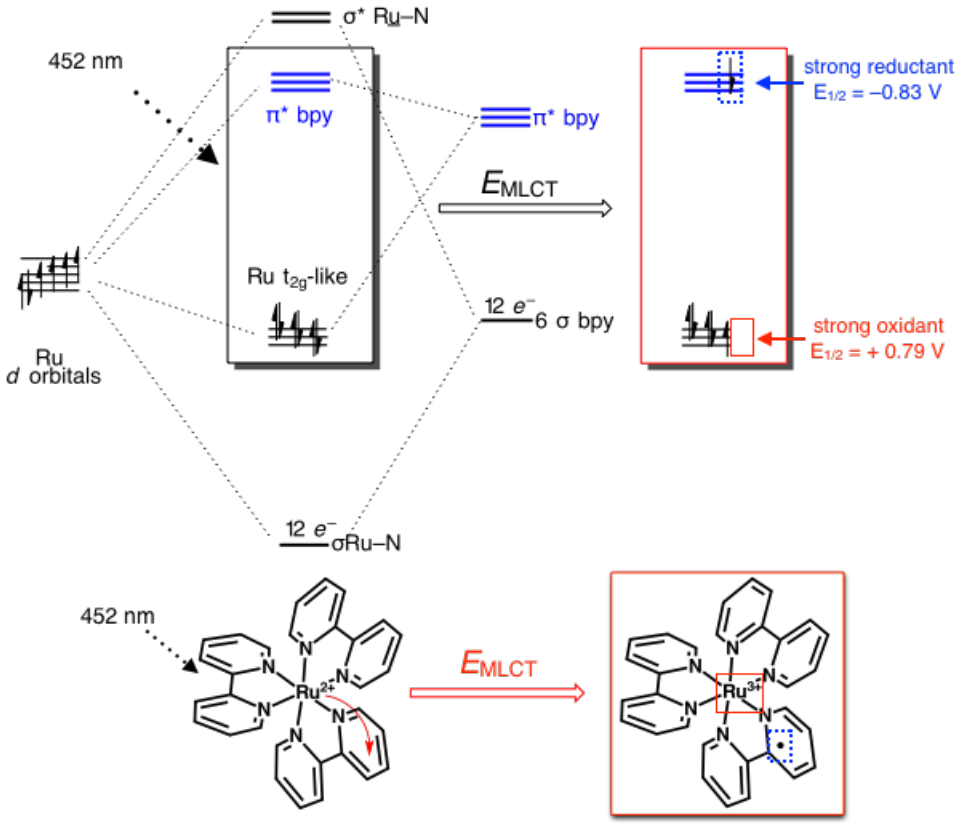

Figure 1.3 Frontier molecular orbital diagram of $Ru(bpy)_3^{2+}$.

Figure 1.3 shows the frontier molecular orbital diagram of the quintessential photosensitizer, tris(2,2'-bipyridine)ruthenium(II) dication, $[Ru(bpy)_3]^{2+}$. The redox-active

bipyridine ligands have π* orbitals that are electronically inserted below the e_g*-like orbitals of the ruthenium center.[45] Excitation of a visible photon (λ_{max} = 452 nm, ε = 13,000 M^{-1} cm^{-1}) promotes an electron from the filled t_{2g}-like orbitals of the ruthenium center to the low-lying π* orbitals on the redox-active bipyridine ligand. This metal-to-ligand charge-transfer (MLCT) transition generates a short-lived photo-induced singlet excited-state, ^{1}MLCT. [46] The charge-separated excited-state: ^{1}MLCT = $[Ru^{III}(bpy)(bpy^{\bullet -})]^{2+}$ is a result of a light-induced shift of electron density from the metal center to the ligand and is a species with entirely different properties compared with those of the ground-state molecule. In particular, the molecule is both a stronger reductant and a stronger oxidant. In fact, it is the strong excited-state redox potentials of $[Ru(bpy)_3]^{2+}$ that have famously made it one of the most utilized photosensitizers in electron transfer reactions. [46-49]

1.3 Estimating the Redox Potentials of the Excited-State

Photo-excited reactants have been widely used in the study of electron transfer because their excited-states are better oxidants and reductants than their ground-state counterparts.[50-52] In the most basic sense, if the lifetime of the excited-state is long enough, the photo-excited dye* can interact with another species, B and undergo the following electron transfer reactions:

$$Dye + h\nu \rightarrow Dye^* + B \rightarrow Dye^+ + B^- \quad \text{oxidative electron transfer} \quad (1)$$

$$Dye + h\nu \rightarrow Dye^* + B \rightarrow Dye^- + B^+ \quad \text{reductive electron transfer} \quad (2)$$

The ability and efficacy of a photosensitizer to drive these processes is governed by its redox potentials in the excited-state. The oxidation and reduction potentials of the excited-state, or the ability of the excited molecule to reduce or oxidize another species, can be derived directly from the observable ground-state electrochemical potentials and the

energy difference between the HOMO and LUMO orbitals.[48] This correlation, illustrated in **Scheme 1-1**, can be made only when the orbitals involved in the optical transitions and redox processes are the same.

Scheme 1-1 Relationship between ground-state electrochemical potentials, HOMO-LUMO gap, and excited-state redox potentials reproduced from Ref [53].

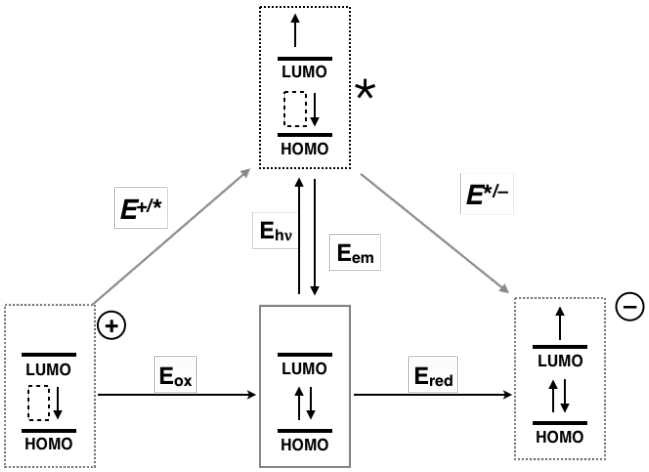

Considering **Scheme 1-1**, the ground state of a molecular dye (electron configuration: $[HO^2LU^0]$) can undergo a one electron oxidation to generate the monocationic species, $[HO^1LU^0]^+$; a one electron reduction to generate the monoanionic species, $[HO^2LU^1]^-$; or photo-excitation to generate the short-lived electronic excited-state, $[HO^1LU^1]^*$. The oxidation and reduction potentials of the excited-state can be estimated by utilizing the relationship shown in **Scheme 1-1** to derive the following equations:

$$E^{+/*} = E_{ox} - h\nu \qquad \textbf{(Eq. 3)}$$

$$E^{*/-} = E_{red} + h\nu \qquad \textbf{(Eq. 4)}$$

The excited-state oxidation potential ($E^{+/*}$, **Eq. 3**) is the potential at which the photo-excited molecule, $[HO^1LU^1]^*$ will reduce another species. $E^{+/*}$ corresponds to the $[LUMO]^{0/-}$

redox couple, when the HOMO has been oxidized by one electron, E_{ox} is the $[HOMO]^{+/0}$ redox couple in the ground state, and hν is the energy of the photon absorbed. The excited-state reduction potential ($E^{*/-}$, **Eq. 4**) is the potential at which the photo-excited molecule, $[HO^1LU^1]^*$ will oxidize another species. Where $E^{*/-}$ specifically corresponds to the $[HOMO]^{+/0}$ redox couple when the LUMO has been reduced by one electron, E_{red} is the $LUMO^{0/-}$ ground state redox couple, and hν is the energy difference between the orbitals giving and receiving the electron (in eV). [53]

A coordination compound that yields a potent excited-state through excitation by visible photons can be utilized as a photosensitizer to fuel important chemical reactions that are not driven by visible light excitation. Furthermore, the ability to estimate the excited-state redox potentials of a chromophore is a useful tool when designing photosensitizers for applications in solar energy conversion schemes and photo-catalysis. [14,54-59]

1.4 Ligand-to-Ligand Charge Transfer (LL′CT) Transitions

The discussion of photo-induced charge separation in photosensitizers is frequently restricted to those between the central metal and the ligands. However, the metal may also facilitate interaction *between* the ligands. In fact, metal complexes of the type $L_{red}–M–L_{ox}$, where L_{red} = an electron-rich redox-active donor ligand and L_{ox} = electron-poor redox-active acceptor ligand have garnered considerable attention as charge-transfer photosensitizers in recent years.[60-64] Classified according to the loci of donor and acceptor sites, ligand-to-ligand charge-transfer (LL′CT) chromophores are of particular interest because their ligand-localized frontier molecular orbitals often give rise to intense low-energy transitions in the visible region of the solar spectrum.[65] Moreover, because the

frontier molecular orbitals are ligand-localized, the energy of these orbitals (and consequently their optical and ground-state redox properties) are easily tuned through chemical modification of the donor and acceptor ligands. [61]

A LL'CT transition occurs if one ligand has a filled orbital (HOMO, donor) that is high in energy, and another ligand has an empty orbital (LUMO, acceptor) that is low in energy. The donor and acceptor orbitals must be arranged co-planar to one another in order to maximize the electronic coupling between the two. Square-planar coordination environments supply the best arrangement for the particular juxtaposition. Furthermore, considering the *d* orbital splitting in a square-planar ligand field, a d^8 electron count for the metal ion should provide the most redox inert metal center, while providing a closed shell electronic environment. It should be no surprise that square-planar LL'CT complexes are classically exemplified using group ten metal ions in their +2 oxidation state such as Ni(II), Pd(II), and Pt(II). [66-68]

Square-planar donor acceptor complexes of platinum(II) are well established in the literature, particularly, examples that combine catecholate[69], dithiolate[64,70], or amidophenolate[71] donor ligands with bipyridine[72] or phenanthroline[73] acceptor ligands. Some relevant examples are shown in **Chart 1-2**. **Table 1-1** lists the energy of their band maxima, ground-state redox and estimated excited-state potentials. These complexes are typical examples of square-planar coordination compounds possessing lowest energy electronic transitions that are mainly LL'CT in nature. For example, considering complexes with the same bpy^{t}Bu$_2$ acceptor ligand (top row, **Chart 1-2**), the oxidation potentials for the three complexes become more negative as the donor ligand changes from $(mnt)^{2-}$ to $(tdt)^{2-}$to $(ap)^{2-}$. This trend is mirrored in the absorption spectra where the highest energy

transition belongs to (mnt)Pt(bpy^{t}Bu$_2$) and the lowest belongs to (ap)Pt(bpy^{t}Bu$_2$). Because all three complexes possess the same metal ion and acceptor ligand, it can be established that the HOMO resides predominantly on the donor ligand and its energy can be tuned by changing the heteroatoms or by increasing conjugation within the ligand-backbone. Furthermore, using **Eq. 3**, we can relate the ground-state oxidation potentials (E_{ox}) and the energy of the emission maxima (E_{em}) of (mnt)Pt(bpy^{t}Bu$_2$) and (tdt)Pt(bpy^{t}Bu$_2$) to estimate the reducing capability of these dyes in the excited-state. Aligning with the trend in the ground-state potentials, (tdt)Pt(bpy^{t}Bu$_2$) is estimated to be the stronger excited-state oxidant of the two. [70]

Chemical manipulation to the backbone of the α-diimine acceptor ligand by incorporation of electron-withdrawing functional groups or by increasing the conjugation affects the energies of the LUMO orbitals analogously. These perturbations manifest in the electrochemical data displaying less negative reduction potentials than the non-functionalized derivatives. For example, (tdt)Pt(bpy^{t}Bu$_2$) possess a ground-state first reduction potential at –1.91 V vs. $[Cp_2Fe]^{+/0}$. When the α-diimine acceptor ligand is equipped with two functional groups capable of tethering to metal oxide surfaces (as is the case with (tdt)Pt(bpy^{COOEt}), **Table 1-1**) the equivalent redox event shifts almost +300 mV to –1.60 V. This anodic shift in the first reduction potential can be attributed to the lowering of the LUMO orbital by incorporation of the electron-withdrawing ester functionalities.

Chart 1-2 Examples of square-planar (donor)Pt^{II}(acceptor) charge-transfer complexes. [69, 70, 71]

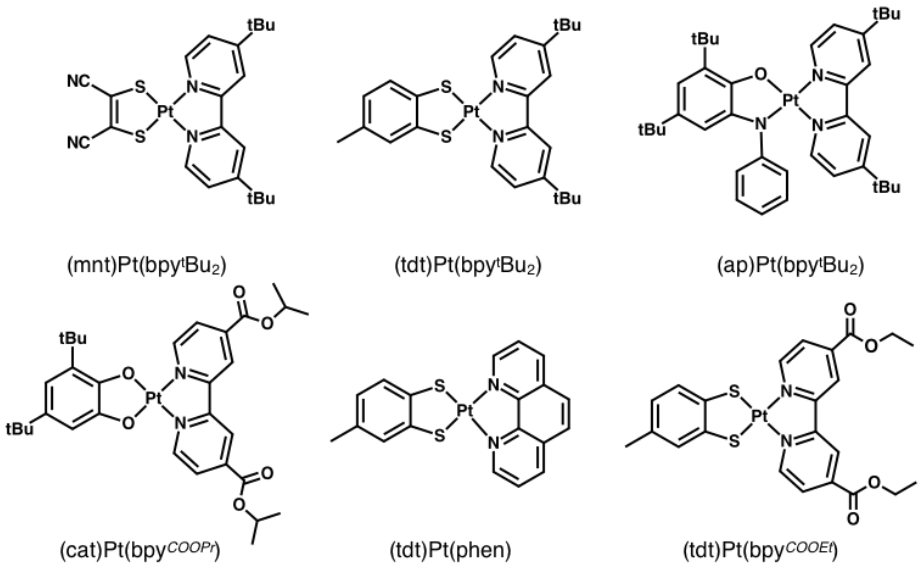

Table 1-1 Relevant Optical and Electrochemical Data for Square-Planar Complexes of Pt(II).

			$E^{o\prime}$/ V vs. $[Cp_2Fe]^{+/0}$			
	λ_{max} /nm (eV)	E_{em} /eV	E_{red}	E_{ox}	$E^{*/-}$	$E^{+/*}$
(mnt)Pt(bpy^{t}Bu$_2$)[70]	497 (2.5)	2.04	–1.91	0.30	0.13	–1.7
(tdt)Pt(bpy^{t}Bu$_2$) [70]	563 (2.2)	1.93	–2.04	–0.25	–0.19	–2.2
(ap)Pt(bpy^{t}Bu$_2$)[71]	780 (1.6)	*NA*	–1.90	–0.	NA	NA
(cat)Pt(bpy^{COOPr}) [69]	700 (1.8)	*NA*	–1.37	–0.03	NA	NA
(tdt)Pt(phen)[70]	580 (2.1)	1.84	–1.96	–0.26	–0.12	–2.1
(tdt)Pt(bpy^{COOEt}) [70]	680 (1.8)	1.58	–1.60	–0.228	–0.02	–1.81

Strong metal-ligand π interactions between platinum and the softer dithiolate ligands result in significant metal contribution to the composition of the HOMO. This significant metal contribution to the HOMO suggests the lowest energy transitions as mixed-metal-ligand-to-ligand charge-transfer (MMLL'CT) transition[74,75] rather than the LL′CT observed in the Ni(diimine)(dithiolate) complexes first reported by Dance[76]and later by Vogler. [77] Nevertheless, derivatives are emissive in solution owing to a large spin–orbit

coupling contribution from platinum that facilitates intersystem crossing to a long-lived ^{3}MMLL'CT excited state. The long-lived ^{3}MMLL'CT excited state of these complexes allows them to be used as photosensitizers either in homogeneous solution (bimolecular electron or energy transfer)[73] or covalently linked to an electron collector (intramolecular electron transfer).[78] It must be stated however, that photo-induced electron transfer into the conduction band of TiO_2 has been measured to take place on a femtosecond time-scale.[79] The rapid charge injection measured for complexes that are tethered to TiO_2 by carboxyl functional groups suggests that a long-lived excited-state may not be a fundamental requirement when designing photosensitizers for charge injection. The development of less-costly alternatives to these noble-metal sensitizers is particularly important regarding the realization of cost-effective sustainable energy.

1.5 Contributions of the Research of this Dissertation

The work described in this dissertation focuses on the rationale behind the design and synthesis of charge-transfer chromophores with lowest energy transitions that are ligand-to-ligand charge transfer (LL'CT) in nature. Through the use of redox-active ligands, co-planar arrangement of donor and acceptor orbitals, and ligand-to-ligand charge-transfer (LL'CT) excited-states, the chromophores described in this dissertation are designed to meet the strict criteria of an effective charge-transfer chromophore. These requirements are: (1) a HOMO-LUMO gap of 1.0 to 2.5 eV to allow strong absorption of light in the most intense portion of the solar spectrum, (2) tunable redox properties so that electron-injecting dyes are powerful excited-state reductants and hole-injecting dyes are powerful excited-state oxidants, (3) a strong and exploitable direction of charge transfer (dipolar

ground-state), (4) an excited-state capable of rapid electron or hole injection into an electrode or catalyst center, (5) long-term stability under normal photochemical conditions, and (6) an easy synthesis from inexpensive and readily-abundant elements and ligands. Currently no molecular dye satisfies all of these criteria.[80]

The current chapter is meant to provide background information in the topic of redox-active ligands, their role in non-innocent coordination compounds, the importance of photo-induced excited-states, and to illustrate the ability to tune excited-state properties through molecular design.

Chapter 2 will introduce a series of square-planar donor-acceptor (D-A) LL′CT dyes with the general formula: (donor)Ni^{II}(acceptor) where donor = 9,10 phenanthrenediolate, $(pdiol)^{2-}$ and acceptor = (N,N'-bis(2,4,6-trimethylphenyl)-2,3-butanediimine, bdi; N,N'-bis(2,4,6-trimethylphenyl)-acenaphthenediimine, adi; and N,N'-bis(2,4,6-trimethylphenyl)-9,10-phenanthrenediimine, pdi) The juxtaposition of donor catecholate and acceptor diimine ligands in these complexes manifest intense LL'CT bands throughout the visible and near-IR portions of the spectrum. Electrochemical and spectroscopic data show the energy of the charge-transfer bands and the ground state redox potentials are heavily dependent on the identity of the ligands. This work showed that the energy of the ligand-localized HOMO and LUMO orbitals can be controlled independently of one another by chemical modification to the catecholate donor and diimine acceptor ligands, respectively.

Chapter 3 leverages the tunable nature LL′CT transitions to target near-IR absorbing dyes capable of accessing potent excited-state oxidation potentials. The use of bipyridyl-type acceptor ligands maintains a LUMO at high energy, exemplified by the negative reduction potentials. Incorporation of the amidophenolate donor ligand destabilizes the

HOMO energy and pushes the LL'CT absorption well into the NIR (λ_{max}: 890 and 970 nm. According to the electro- and spectrochemical data the (amidophenolate)Ni(acceptor) dyes reported in Chapter 3 are estimated to be potent excited-state reductants ($E^{+}/*(^{1}LL'CT$) = ‑1.3 and ‑1.4 V vs. SCE) through NIR photons (1.4 and 1.3 eV).

Chapter 4 explores the optical and electrochemical characteristics of two D-A Ni(II) LL'CT dyes introduced in Chapter 3 that have been functionalized with carboxyl anchoring groups for tethering to metal oxide surfaces. The bipyridine acceptor ligand of (cat)Ni(bpy) and (ap)Ni(bpy) is functionalized with two carboxyl anchoring groups at 4 and 4' positions for tethering to a metal oxide surface.. Upon optical excitation, the dyes are potent excited-state reductants and should be able to populate the conduction band of TiO_2. Although dyes reported herein appear to adsorb on the surface of a TiO_2 thin film, the resulting sensitized films degraded once exposed to air and rendered electron injection studies impossible. Although the air sensitivity of these dyes is problematic, future precautions such as air-free studies can be made in order to test their efficacy to inject electrons into large band gap semiconductors.

Chapter 5 introduces three six-coordinate D-A Ru(II) charge-transfer dyes with the general formula: (donor)Ru($N_2N_2^q$) [donor = 2 Cl^-, $(catB_4)^{2-}$ and $(cat)^{2-}$]. The co-planar arrangement of donor and acceptor orbitals was achieved through the use of the tetradentate, redox-active, N,N'-bis-(3-dimethylaminopropyl)-4,5-dimethoxy-benzene-1,2-diiminoquinone, ($N_2N_2^q$). The lowest energy transition red-shifts from 600 to 780 nm (0.41 eV) when the donor is varied from the electron withdrawing $(catBr_4)^{2-}$ to the electron donating $(cat)^{2-}$. These new octahedral D-A Ru(II) charge-transfer complexes demonstrate that the tetradentate $N_2N_2^q$ acceptor ligand, when coordinated to a d^6 metal ion, allows for

the co-planar installation of redox-active donor ligand. Future studies should be conducted in order to further elucidate complicated the nature of the lowest energy transition.

1.6 References

(1) Lyaskovskyy, V.; de Bruin, B. *ACS Catal.* **2012,** *2*, 270-279
(2) Kaim, W.; Schwederski, B. *Coord. Chem. Rev.* **2010**, *254* 1580–1588
(3) McConnell, I.; Li, G.; Brudvig, G. W. *Chemistry & Biology* **2010**, *17* (5), 434–447.
(4) Walker, J. E. *Biochem. Soc. Trans.* **2013**, *41* (1), 1–16.
(5) Bazhenova, T. A.; Shilov, A. E. *Coord. Chem. Rev.***1995**, *144*, 69–145.
(6) Eremin, D. B.; Ananikov, V. P. *Coord. Chem. Rev.* **2017**, *346*, 2–19.
(7) Williams, C. A.; Collatz, G. J.; Wang, H.; Prentice, I. C.; Canadell, J. G.; Raupach, M.; Keenan, T. F. *Nature Comm.* **2016**, *7*, 13428.
(8) Bozic-Weber, B.; Constable, E. C.; Housecroft, C. E. *Coord. Chem. Rev.* **2013**, *257* (21-22), 3089–3106.
(9) Andreini, C.; Bertini, I.; Cavallaro, G.; Holliday, G. L.; Thornton, J. M. *J Biol Inorg Chem* **2008**, *13* (8), 1205–1218.
(10) Praneeth, V. K. K.; Ringenberg, M. R.; Ward, T. R. *Angew. Chem. Int. Ed.* **2012**, *51* (41), 10228–10234.
(11) Weinstein, J. A. In *Applied Photochemistry*; Springer Netherlands: Dordrecht, 2013; pp 105–148.
(12) Cook, T. R.; Dogutan, D. K.; Reece, S. Y.; Surendranath, Y.; Teets, T. S.; Nocera, D. G.
(13) Garcia, C. G.; de Lima, J. F.; Murakami Iha, N. Y. *Coord. Chem. Rev.* **2000**, *196* (1), 219–247.
(14) McCusker, J. K. *Science* **2001**, *293* (5535), 1599–1601.
(15) Gonçalves, L. M.; de Zea Bermudez, V.; Ribeiro, H. A.; Mendes, A. M. *Energy Environ. Sci.* **2008**, *1* (6), 655.
(16) Hardin, Brian E, Henry J Snaith, and Michael D McGehee. *Nature Photonics* **2012**, *6* (3). 162–69.
(17) Luca, O. R.; Crabtree, R. H. *Chem. Soc. Rev.* **2013**, *42* (4), 1440–1459.
(18) Di Zhu; Thapa, I.; Korobkov, I.; Gambarotta, S.; Budzelaar, P. H. M. *Inorg. Chem.* **2011**, *50* (20), 9879–9887.
(19) Carter, S. M.; Sia, A.; Shaw, M. J.; Heyduk, A. F. *J. Am. Chem. Soc.* **2008**, *130* (18), 5838–5839.
(20) Daniel E Wheeler; Jorge H Rodriguez, A.; McCusker, J. K. *J Phys. Chem. A.* **1999**; Vol. 103, pp 4101–4112.
(21) Vlček, A. *Coord. Chem. Rev.s* **2010**, *254* (13-14), 1357.
(22) Pop, F.; Avarvari, N. *Coord. Chem. Rev.* **2017**, *346*, 20–31.
(23) Brown, S. N. *Inorg. Chem.* **2012**, *51* (3), 1251–1260.
(24) Bachmann, J.; Nocera, D. G. *J. Am. Chem. Soc.* **2005**, *127* (13), 4730–4743.
(25) Szigethy, G.; Heyduk, A. F. *Dalton Trans.* **2012**, *41* (26), 8144.
(26) Suzanne C Bart; Emil Lobkovsky; Eckhard Bill, A.; Chirik, P. J. *pubs.acs.org*.
(27) Cipressi, J.; Brown, S. N. *Chem. Commun.* **2014**, *50* (59), 7956–7959.
(28) Szilagyi, R. K. *Structural Origins of Noninnocent Coordination Chemistry*; John Wiley

& Sons, Ltd.
(29) Kunze, K. L.; Davidson, E. R. *J. Phys. Chem.* **1992**, *96* (5), 2129–2141.
(30) Vlček, A. *Inorg. Chem.* **1986**, *25* (4), 522–526.
(31) Shufler, S. L.; Sternberg, H. W.; Friedel, R. A. *J. Am. Chem. Soc.* **1956**, *78* (12), 2687–2688.
(32) Smídova, I.; Vlček, A., Jr; Vlcek, A. A. *Inorganica Chimica Acta* **1982**, *64*, L63–L64.
(33) Buchanan, R. M.; Claflin, J.; Pierpont, C. G. *Inorg. Chem.* **1983**, *22* (18), 2552–2556.
(34) Shen, M.; Leslie, B. E.; Driver, T. G. *Angew. Chem. Int. Ed.* **2008**, *47* (27), 5056–5059.
(35) Hurst, J. K.; Cape, J. L.; Clark, A. E.; Das, S.; Qin, C. *Inorg. Chem.* **2008**, *47* (6), 1753–1764.
(36) Eremin, D. B.; Ananikov, V. P. *Coord. Chem. Rev.* **2017**, *346*, 2–19.
(37) Chirik, P. J.; Wieghardt, K. *Science* **2010**, *327* (5967), 794–795.
(38) Heyduk, A. F.; Zarkesh, R. A.; Nguyen, A. I. **2011**, *50* (20), 9849–9863.
(39) Haneline, M. R.; Heyduk, A. F. *J. Am. Chem. Soc.* **2006**, *128* (26), 8410–8411.
(40) Lu, F.; Zarkesh, R. A.; Heyduk, A. F. *Eur. J. Inorg. Chem.* **2011**, *2012* (3), 467–470.
(41) Vogler, A.; Kunkely, H. *Comments on Inorganic Chemistry* **1997**, *19* (5), 283–306.
(42) Vogler, A.; Kunkely, H. *Comments on Inorganic Chemistry* **1990**, *9* (3-4), 201–220.
(43) Castellano, F. N. *Acc. Chem. Res.* **2015**, *48* (3), 828–839.
(44) Alstrum-Acevedo, J. H.; Brennaman, M. K.; Meyer, T. J. *Inorg. Chem.* **2005**, *44* (20), 6802–6827.
(45) Biner, M.; Buergi, H. B.; Ludi, A.; Roehr, C. *J. Am. Chem. Soc.* **1992**, *114* (13), 5197–5203.
(46) Juris, A.; Balzani, V.; Barigelletti, F.; Campagna, S.; Belser, P.; Zelewsky, von, A. *Coord. Chem. Rev.* **1988**, *84*, 85–277.
(47) Boyer, J. L.; Rochford, J.; Tsai, M.-K.; Muckerman, J. T.; Fujita, E. *Coord. Chem. Rev.* **2010**, *254* (3-4), 309–330.
(48) Reynal, A.; Forneli, A.; Palomares, E. *Energy Environ. Sci.* **2010**, *3* (6), 805–812.
(49) Mohammad K Nazeeruddin; Peter Péchy; Thierry Renouard; Shaik M Zakeeruddin; Robin Humphry-Baker; Pascal Comte; Paul Liska; Le Cevey; Emiliana Costa; Valery Shklover; Leone Spiccia; Glen B Deacon; Carlo A Bignozzi, A.; Grätzel, M.
(50) Balzani, V.; Bergamini, G.; Campagna, S.; Puntoriero, F. In *link.springer.com*; Topics in Current Chemistry; Springer Berlin Heidelberg: Berlin, Heidelberg, 2007; Vol. 280, pp 1–36.
(51) Williams, J. A. G. In *Masters of the Structural Aesthetic*; Topics in Current Chemistry; Springer Berlin Heidelberg: Berlin, Heidelberg, 2007; Vol. 281, pp 205–268.
(52) Sýkora, J.; Šima, J. *Coord. Chem. Rev.* **1990**, *107*, 1–212.
(53) Vlcek, A. A.; Dodsworth, E. S.; Pietro, W. J.; Lever, A. B. P. *Inorg. Chem.* **1995**, *34* (7), 1906–1913.
(54) Swierk, J. R.; Mallouk, T. E. *Chem. Soc. Rev.* **2013**, *42* (6), 2357–2387.
(55) Chowdhury, P.; Gomaa, H.; Ray, A. K. In *pubs.acs.org*; ACS Symposium Series; American Chemical Society: Washington, DC, 2013; Vol. 1124, pp 231–266.
(56) Zong, R.; Thummel, R. P. *J. Am. Chem. Soc.* **2005**, *127* (37), 12802–12803.
(57) Hanna, M. C.; Nozik, A. J. *J. Appl. Phys.* **2006**, *100* (7), 074510.
(58) Grätzel, M. *Inorg. Chem.* **2005,** *44*, 6841-6851
(59) Gust, D.; Moore, T. A.; Moore, A. L. *Acc. Chem. Res.* **2009**, *42* (12), 1890–1898.
(60) Cameron, L. A.; Ziller, J. W.; Heyduk, A. F. *Chem. Sci.* **2016**, *7* (3), 1807–1814.

(61) Kramer, W. W.; Cameron, L. A.; Zarkesh, R. A.; Ziller, J. W.; Heyduk, A. F. *Inorg. Chem.* **2014**, 140806135722006.
(62) Paw, W.; and, W. P.; Eisenberg, R. *Inorg. Chem.* **1997**, *36* (11), 2287–2293.
(63) Weinstein, J. A.; Tierney, M. T.; Davies, E. S.; Base, K.; Robeiro, A. A.; Grinstaff, M. W. *Inorg. Chem.* **2006**, *45* (11), 4544–4555.
(64) Connick, W. B.; Gray, H. B. *J. Am. Chem. Soc.* **1997**, *119* (48), 11620–11627.
(65) Wang, Y.; Hauser, B. T.; Rooney, M. M.; Burton, R. D.; Schanze, K. S. *J. Am. Chem. Soc.* **1993**, *115* (13), 5675–5683.
(66) Yang, J.; Kersi, D. K.; Giles, L. J.; Stein, B. W.; Feng, C.; Tichnell, C. R.; Shultz, D. A.; Kirk, M. L. *Inorg. Chem.* **2014**, *53* (10), 4791–4793.
(67) Latham, A. R.; Hascall, V. C.; Gray, H. B. *Inorg. Chem.* **1965**, *4* (6), 788–792.
(68) Billig, E.; Williams, R.; Bernal, I.; Waters, J. H.; Gray, H. B. *Inorg. Chem.* **1964**, *3* (5), 663–666.
(69) Scattergood, P. A.; Jesus, P.; Adams, H.; Delor, M.; Sazanovich, I. V.; Burrows, H. D.; Serpa, C.; Weinstein, J. A. *Dalton Trans.* **2015**.
(70) Cummings, S. D.; Eisenberg, R. *J. Am. Chem. Soc.* **1996**, *118* (8), 1949–1960.
(71) Sun, X.; Chun, H.; Hildenbrand, K.; Bothe, E.; Weyhermüller, T.; Neese, F.; Wieghardt, K. *Inorg. Chem.* **2002**, *41* (16), 4295–4303.
(72) Vogler, A.; Kunkely, H. *J. Am. Chem. Soc.* **1981**, *103* (6), 1559–1560.
(73) Zheng, B.; Sabatini, R. P.; Fu, W.-F.; Eum, M.-S.; Brennessel, W. W.; Wang, L.; McCamant, D. W.; Eisenberg, R. *Proc. Natl. Acad. Sci. U.S.A.* **2015**, *112* (30), E3987–E3996.
(74) Zuleta, J. A.; Bevilacqua, J. M.; Rehm, J. M.; Eisenberg, R. *Inorg. Chem.* **1992**, *31* (8), 1332–1337.
(75) Chakraborty, S.; Wadas, T. J.; Hester, H.; Schmehl, R.; Eisenberg, R. *Inorg. Chem.* **2005**, *44* (20), 6865–6878.
(76) Miller, T. R.; Dance, I. G. *J. Am. Chem. Soc.* **1973**, *95* (21), 6970–6979.
(77) Vogler, A.; Kunkely, H.; Hlavatsch, J.; Merz, A. *Inorg. Chem.* **1984**, *23* (4), 506–509.
(78) Zhang, J.; Du, P.; Schneider, J.; Jarosz, P.; Eisenberg, R. *J. Am. Chem. Soc.* **2007**, *129* (25), 7726–7727.
(79) Ellingson, R. J.; Asbury, J. B.; Ferrere, S; Ghosh, H.N.; Sprague, J. R.; Lian, T. A.; Nozik, A. J. *J. Phys. Chem. B.* **1998,** *102,* 6455-6458
(80) Robertson, N. *Angew. Chem. Int. Ed.* **2006**, *45*, 2338-45.

Chapter 2

The Modular Synthesis of Square-Planar Ni(II) LL′CT Complexes

2.1 Introduction

The design of coordination complexes for use as charge-transfer photosensitizers in solar energy conversion schemes is an area of intense research.[1-5] Currently, molecular photosensitizers used in photovoltaics[6-10] (dye-sensitized solar cells) and for photocatalyst centers[11-15] (artificial photosynthesis), often rely on precious metals centers such as ruthenium and platinum. While these photosensitizers have helped us understand the fundamental underpinnings of solar energy capture, their limitations hinder advancements within the field.[16] The inflexibility of a metal-localized HOMO in MLCT transitions results in limited control over the energy of the photoactive frontier molecular orbitals (pFMOs). Additionally, the use of rare and costly noble metals inhibits the realization of scalable and cost effective solar energy conversion strategies.[17] Donor-acceptor complexes based on ligand-to-ligand charge-transfer transitions (LL′CT) offer a promising and practical solution to these problems. In LL′CT dyes, the pFMOs are localized primarily on redox-active ligands, not the metal center, allowing for absolute control over the electrochemical and photo-physical properties of the sensitizer. With the limited involvement of the metal center in the formation of the charge-separated excited-state, noble metals may be replaced by first-row transition metals, as they too will be inconsequential to the potency of the excited-state. Our group's initial efforts towards this goal involved the synthesis and characterization of a series of square-planar donor-acceptor (D-A) LL′CT dyes of the general formula (donor)Ni^{II}(acceptor) where donor = 3,5-di-*tert*-butyl-catecholate, $(cat)^{2-}$; tetrachlorocatecholate, $(catCl_4)^{2-}$; and acceptor = (*N,N*'-bis(2,4,6-trimethylphenyl)-2,3-butanediimine, bdi; *N,N*'-bis(2,4,6-trimethylphenyl)-acenaphthenediimine, adi; and *N,N*'-bis(2,4,6-trimethylphen-yl)-9,10-phenanthrenediimine, pdi).[18] The d^8 nickel(II) metal ion

in these complexes provides a stable, closed-shell electronic configuration and the square-planar coordination environment enforces a coplanar arrangement of the donor and acceptor ligand. The juxtaposition of donor catecholate and acceptor α-diimine ligands in these complexes manifests intense LL'CT bands that can be tuned between 650 and 1240 nm (**Figure 2.1a**). The electrochemical properties of these dyes are dependent on the nature of the donor and acceptor ligand (**Figure 2.1b**). For example, complexes employing the electron-poor $(catCl_4)^{2-}$ donor ligand display the most positive oxidation potentials, regardless of the acceptor ligand. The complexes with the highly conjugated pdi acceptor ligand gave the least negative potentials, regardless of the donor identity.

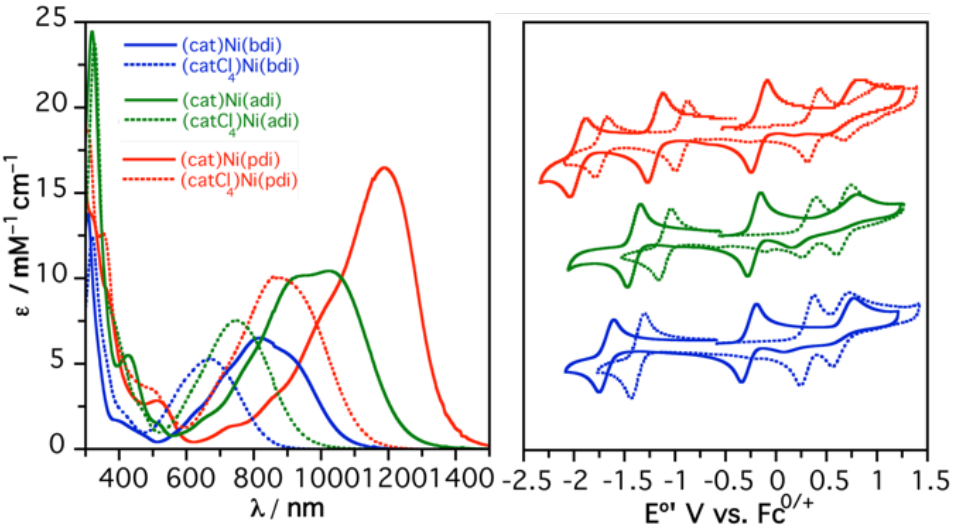

Figure 2.4 Solution UV–vis–NIR absorption spectra of (cat)Ni(diimine) complexes and $(catCl_4)$Ni(diimine) complexes in THF at 298 K (left) and Cyclic voltammetry plots for complexes (cat)Ni(diimine) complexes and $(catCl_4)$Ni(diimine) (right).[18]

This chapter details my efforts to expand on our initial series of nickel(II) LL'CT dyes by incorporating the highly conjugated donor ligand, 9,10 phenanthrenediolate, $(pdiol)^{2-}$ and a new acceptor ligand, 4,4'-di-*tert*-bipyridine (bpy^tBu_2) into the series. The

pairing of the conjugated $(pdiol)^{2-}$ ligand with the low-lying π* LUMO of the exo-cyclic α-diimine acceptor ligands (bdi, adi, pdi), allows us a more in-depth understanding of the range of tunability put forth by these systems. We expected that as the conjugation of the donor and acceptor ligand increases, the LL′CT transition would lose its charge-transfer character.[19]

This chapter will present the synthesis and characterization of a series of donor-acceptor LL′CT chromophores of square-planar nickel(II) centers with the general formulation (catecholate)Ni(diimine). The donor ligand, 9,10 phenanthrenediolate, $(pdiol)^{2-}$ is paired with four different α-diimine acceptor ligands: 4,4'-di-*tert*-bipyridine, bpy^{t}Bu$_2$; (*N,N*'-bis(2,4,6-trimethylphenyl)-2,3-butanediimine, bdi; *N,N*'-bis(2,4,6-trimethylphenyl)-acenaphthenediimine, adi; and *N,N*'-bis(2,4,6-trimethylphenyl)-9,10-phenanthrenediimine, pdi. Structural and spectroscopic data confirm these complexes fit the donor-metal-acceptor model with a dianionic donor ligand and a fully oxidized α-diimine acceptor ligand. UV-vis-NIR spectra of these complexes show intense LL'CT bands ranging from 680 to 1340 nm. Electrochemical studies show two, reversible α-diimine-localized, one-electron reduction events with potentials determined by the nature of the acceptor ligand. The oxidation events of the $(pdiol)^{2-}$ donor ligand appear within a potential range of 0.5 V and exhibit varying degrees of reversibility. The results reported herein establish a family of highly tunable charge-transfer dyes based on an earth abundant metal ion and readily available redox-active ligands.

2.2 Results and Discussion

2.2.1 Synthesis and Characterization

Square-planar donor-acceptor (D-A) charge-transfer dyes reported herein were prepared by leveraging the ability of phenanthrenedione to act as a two-electron oxidant when reacted towards a low-valent metal center.[20] The installation of the catecholate ligand, $(pdiol)^{2-}$ was achieved by a two-electron redox reaction between phenanthrenequinone and the Ni(0) synthon, $Ni(cod)_2$. The general method of preparation is illustrated in **Scheme 2-1**. Treatment of $Ni(cod)_2$, in a benzene or THF solution, with the corresponding α-diimine acceptor ligand affords the putative $(cod)Ni^0(diimine)$ intermediate, indicated by a drastic color change from yellow to dark red (**2.1** was purple). Subsequent addition of the phenanthrenequinone induces a two-electron oxidation of the Ni(0) intermediate to Ni(II), and a two-electron reduction of the phenanthrenequinone to the $(phenanthrenediolate)^{2-}$ or $(pdiol)^{2-\cdot}$ The desired square-planar donor-acceptor Ni(II) complexes, $(pdiol)Ni(bpy^tBu_2)$ (**2.1**), (pdiol)Ni(bdi) (**2.2**), (pdiol)Ni(adi) (**2.3**), and (pdiol)Ni(pdi) (**2.4**) were isolated as deeply colored microcrystalline solids in good yields and purity (77-88%).

Nickel complexes **2.1**–**2.4** are comprised of two different redox-active ligands tethered to a redox-active metal center, which leads to multiple possible oxidation state assignments. High-resolution single crystal X-ray diffraction studies were conducted on all members of the series. The oxidation state of the donor, acceptor, and metal center can be determined by evaluating key bond lengths within the ligand platform. **Figure 2-2** shows the ORTEP diagrams of **2.1**–**2.4** and **Table 2-1** lists their relevant bond distances. Each

complex within the series adopts the expected square-planar geometry, consistent with diamagnetic, d^8 nickel(II) metal centers with no regular distortion pattern within the series.[21,22]

Scheme 2-2 Synthetic route used to access (pdiol)Ni^{II}(acceptor) dyes (top) and the acceptor ligands used in this study (bottom).

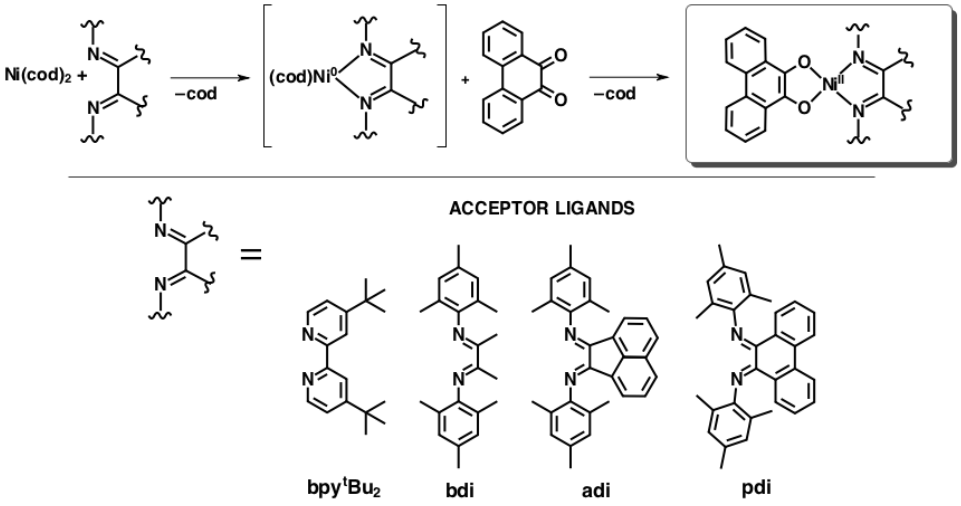

The bite angles of the $(pdiol)^{2-}$ and α-diimine ligands are consistent with O–Ni–O bites angles in the range of 87.1–89.8˚ and N–Ni–N bite angles in the range of 83.14–83.48°. Carbon-heteroatom bond distances are consistent with formal oxidation state assignments of dianionic catecholate ligands and neutral α-diimine ligands. For example, within the bipyridyl acceptor ligand of complex **2.1,** the C7(8)–N1(2) distances average 1.35 Å and the bridgehead C7–C8 distance measures 1.47 Å, and are identical to carbon nitrogen double bonds and C–C single bonds of previously reported neutral bipyridyl ligands.[23] For complexes with the exo-cyclic α-diimine acceptor ligands, **2.2** and **2.3** (bdi and adi), the average C=N bond distance measures 1.30 Å, and is fully consistent with formal carbon-nitrogen double bonds lengths.[18] For (pdiol)Ni(pdi) (**2.4**), the carbon-nitrogen bonds average 1.33 Å, which is slightly longer than the C–N distance observed in **2.2** and **2.3,** but

not long enough to indicate semiquinonate character (typically 1.35 Å).[24] The higher degree of conjugation in **2.4** associated with the phenanthrene backbone may result in delocalization of the π-bonds over the ligand resulting in elongated C=N bonds.

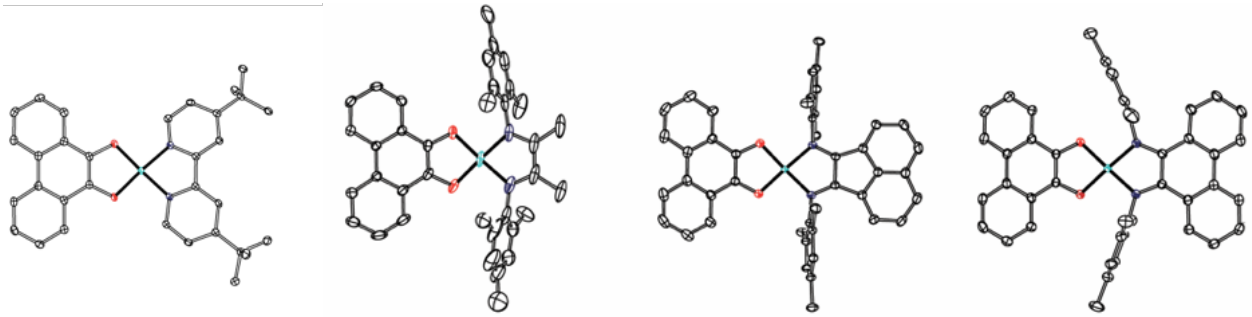

2.1 (pdiol)Ni(bpy^{t}Bu$_2$) **2.2** (pdiol)Ni(bdi) **2.3** (pdiol)Ni(adi) **2.4** (pdiol)Ni(pdi)

Figure 2.5 ORTEP diagrams of (pdiol)Ni(bpy^{t}Bu$_2$) (**2.1**), (pdiol)Ni(bdi) (**2.2**), (pdiol)Ni(adi) (**2.3**), and (pdiol)Ni(pdi) (**2.4**). Thermal ellipsoids are shown at 50% probability. Hydrogen atoms and non-coordinated solvent molecules (if present) have been omitted for clarity.

Table 2-2 Selected Bond Distances for Complexes **2.1**–**2.4**

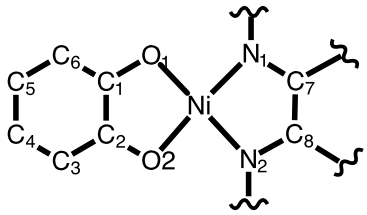

Bond Distances / Å

	2.1	**2.2**	**2.3**	**2.4**
Ni–O(1)	1.8380(14)	1.8274(17)	1.8219(11)	1.8328(11)
Ni–O(2)	1.8295(13)	1.8279(19)		1.8388(11)
Ni–N(1)	1.8782(16)	1.864(2)	1.8837(13)	1.8391(13)
Ni–N(2)	1.8782(16)	1.875(2)		1.8415(13)
O(1)–C(1)	1.353(2)	1.347(3)	1.34441(19)	1.3282(19)
O(2)–C(2)	1.343(2)	1.347(3)		1.3297(18)
C(1)–C(2)	1.372(3)	1.367(3)	1.378(3)	1.384(2)
C(2)–C(3)	1.428(3)	1.425(3)		1.432(2)
C(3)–C(4)	1.422(3)	1.422(3)		1.422(2)

	2.1	**2.2**	**2.3**	**2.4**
C(4)–C(5)	1.450(3)	1.456(3)	1.456(4)	1.466(2)
C(5)–C(6)	1.426(3)	1.421(3)	1.419(2)	1.422(2)
C(1)–C(6)	1.422(3)	1.429(3)	1.432(2)	1.434(2)
N(2)–C(8)	1.353(3)	1.304(3)	1.302(2)	1.332(2)
N(1)–C(7)	1.357(2)	1.301(4)		1.329(2)
C(7)–C(8)	1.470(3)	1.462(5)	1.461(3)	1.462(2)

Regarding the $(pdiol)^{2-}$ donor ligand, the average C–O distances for complexes **2.1**–**2.3** measure 1.35 Å which is within the range of 1.35–1.36 Å measured for C–O distances of the bis(catecholate) complex, $[Ni(cat)_2]^{2-}$.[22] Although complex **2.4** exhibits shorter C–O distances averaging 1.33 Å, they are still longer than observed 1.31 Å for the C–O bonds in bis(semiquinonate) complexes of Ni(II).[25] Overall, the crystallographic data are consistent with the formal assignment of nickel(II) ions coordinated to one dianionic catecholate ligand and one neutral diimine ligand. Complex **2.4** does present evidence of a higher degree of delocalization across the molecule by displaying longer C=N bonds in the acceptor ligand and shorter C–O bonds in the donor ligand.

Complexes **2.1**–**2.4** are diamagnetic in solution, consistent with their solid state structures, and indicative of closed-shell, square-planar nickel(II) complexes. Each complex shows sharp ^{1}H NMR resonances in the normal diamagnetic region when dissolved in the appropriate deuterated solvent (see Experimental). According to the solid-state structures, complexes **2.1**–**2.4** are C_{2v} symmetric and maintain this symmetry while in solution. For example, the two chemically equivalent *tert*-butyl groups of the bpy^{t}Bu$_2$ ligand in **2.1** appear as a singlet at 1.37 ppm and integrate to 18 protons. Likewise, the two chemically equivalent methyl groups along the acceptor backbone of complex (pdiol)Ni(bdi) (**2.2**)

appear as a single resonance at 1.74 ppm integrating to 6 protons. The methyl proton resonances of the mesityl groups in **2.2** translate to two sharp singlets at 2.40 and 2.48 ppm, integrate to 6 and 12 protons respectively, and correspond to the two equivalent methyl groups in the *para* positions and the four equivalent methyl groups in the *ortho* positions of the mesityl rings

2.2.2 Absorption Profiles

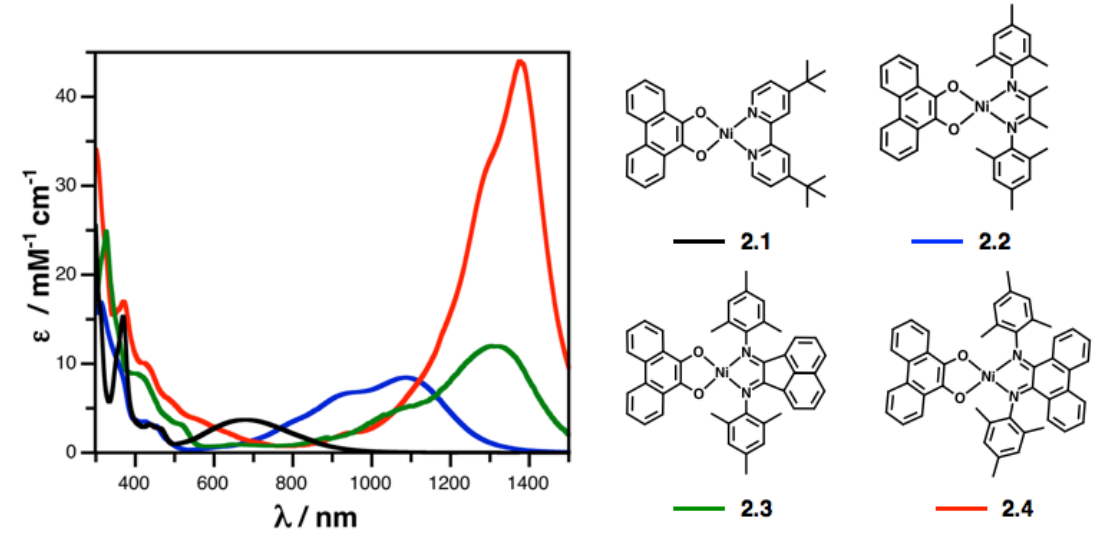

Figure 2.6 UV–vis–NIR data of **2.1**–**2.4** collected in THF solutions at 298 K

All nickel(II) donor-acceptor complexes in this series are highly colored in both the solid state and in solution reflecting their strong absorption properties in the visible region of the electromagnetic spectrum. The absorption spectra of complexes **2.1**–**2.4** in THF were collected from 300-1500 nm and are shown in **Figure 2.3**. The band maxima, extinction coefficients, $E_{LL'CT}$, and solvatochromic shift of each (pdiol)Ni^{II}(acceptor) complex are summarized in **Table 2-2**. Since the donor ligand is the same for every complex, we can

attribute the energies of the band maxima to the nature of the acceptor ligands. A trend can be denoted from the obvious decline in absorption energies in the order of bpy^{t}Bu$_2$ > bdi > adi > pdi. The greatest variation in energy is observed on going from **2.1** to **2.4** where a blue shift from 1380 nm (0.92 eV) to 680 nm (1.82 eV) occurs when the α-diimine is switched from the phenthrendiimine acceptor in **2.4** to bpy^{t}Bu$_2$ ligand in **2.1.** Swapping the endo-cyclic α-diimine in **2.1** for the exo-cyclic butane-diimine ligand in **2.2** causes a large (0.68 eV) red-shift of the λ_{max} to 1090 nm. Introducing conjugation into the backbone of the exo-cyclic α-diimine ligand, as is the case with the acenaphthene backbone of **2.3,** further red shifts the band maxima from 1090 nm (1.14 eV, complex **2.2**) to 1310 nm (0.95 eV).

Table 2-3 Selected Bond Distances For Complexes **2.1**–**2.4**

	λ_{max} / nm	ε / M^{-1} cm^{-1}	$E_{LL'CT}$ / eV	Solvatochromic Shift /SS
2.1	680	3826	1.329	0.48
2.2	1090	8500	0.96	0.17
2.3	1310	9920	0.821	0.07
2.4	1370	43 000	0.823	0

Finally, when the exo-cyclic backbone is fully conjugated, as is the case with the backbone of the pdi ligand in **2.4**, an additional red shift of 60 nm occurs (0.04 eV) to 1370 nm. By varying the acceptor ligand we were able to tune the lowest energy absorption by 0.92 eV. Switching from endo- to exo-cyclic α-diimine shrinks the HOMO-LUMO gap by 0.68 eV. Within the endo-cyclic subgroup of complexes (**2.2**–**2.4**) manipulation of the amount of conjugation across the acceptor backbone affords a tunable range of 0.24 eV.

2.2.3 Solvatochromism

The presence of two different redox-active ligands, where one is electron rich and the other is electron poor should result in a dipolar ground state and exhibit negative

solvatochromic behavior in polar solvents.[26,27] As the dielectric constant of the solvent decreases, the band maxima blue shifts to higher energy. In order to quantify the solvatochromic response and determine the strength of the ground-state dipole, the solvatochromic shift number (SS) was determined for each complex and listed in **Table 2.2**. The LL′CT excited-state energy was estimated from the low-energy onset of the absorption curve for each solvent, demonstrated in **Figure 2.4c.** Measurements of the complexes containing the exo-cyclic α-diimine ligands (complexes **2.2**–**2.4,** not shown) were taken in MeCN, DMF, THF, benzene, and toluene; the lowest energy transitions behaved almost uniformly and exhibited little-to-no solvatochromic shift (**Table 2.2**).

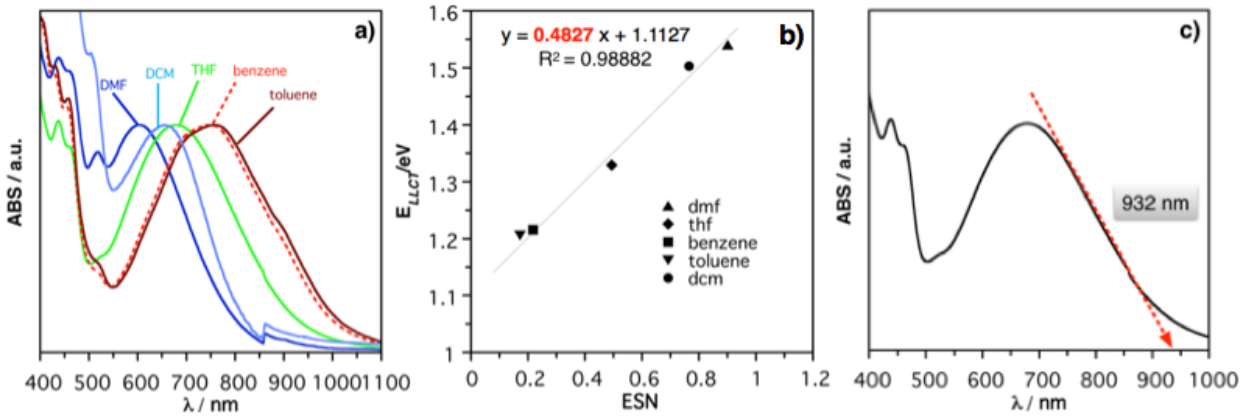

Figure 2.7 a) Normalized absorption spectra of (pdiol)Ni(bpy^{t}Bu$_2$) (**2.1**) in DMF, DCM, THF, benzene, and toluene; b) plot of the linear correlation between the energy of the charge-transfer state and empirical solvent number (ESN) onset LL′CT absorption versus the empirical solvent number for each solvent; c) estimation of the onset LL′CT absorption.

Complexes (pdiol)Ni(pdi) (**2.4**) and (pdiol)Ni(adi) (**2.3**) yielded negligible solvatochromic shift values of 0, and 0.07, respectively while complex, **2.2**, with the butane-diimine ligand, gave a slightly larger value of 0.17 (SS). In contrast, the energy of the charge-transfer transition of complex **2.1**, with the endo-cyclic α-diimine ligand, showed great dependence on the polarity of the solvent. **Figure 2.4a** shows the electronic absorption spectra of **2.1**

where, the λ_{max} is ~600 nm (2.0 eV) in MeCN and red shifts to ~780 nm in toluene. As the dielectric constant of the solvent increases, so does the energy of the charge-transfer band. To eliminate errors associated with changes in the intensity of different vibronic bands, the excited-state energies used in **Figure 2.4b** were estimated from the low-energy onset of the absorption curve as shown in **Figure 2.4c**. The slope of the line in **Figure 2.ba** gave a solvatochromic shift of 0.483 indicating that the polarity of the ground state can be described as dipolar, whereas the negligible SS values for **2.2**–**2.4** indicate the lack of dipole in the ground state.

2.2.4 Electrochemistry

The electrochemical behavior of compounds **2.1**–**2.4** was studied by cyclic voltammetry and differential pulse voltammetry, and both voltammograms are shown in **Figure 2.5.** The potentials, listed in **Table 2-3,** were recorded in THF solutions containing 0.10 M $[Bu_4N][PF_6]$ as the supporting electrolyte at a glassy-carbon working electrode. Bulk measurements (*) concluded that the initial event located on the left and right of the bulk material (denoted by *) corresponds to the first reduction ($E^{\circ\prime}_3$) and first oxidation ($E^{\circ\prime}_2$) events, respectfully.

All complexes displayed two one-electron reduction processes that appear to be fully reversible ($i_{pa}/i_{pc} \cong 1.0$) and correspond to the [α-diimino-semiquinonate•]$^-$/[α-diimine]^0 couple ($E^{\circ\prime}_3$) and [α-diimino-semiquinate•]$^-$/[α-diamino-quinonate]$^{2-}$ couple ($E^{\circ\prime}_4$). The potential of these events are heavily dependent on the nature of the acceptor ligand and display the trend discussed in the absorption spectroscopy where reduction potentials are more negative ongoing from pdi to bpy^{t}Bu$_2$. For example, the complex

containing the endo-cyclic α-diimine ligand, bpy^{t}Bu$_2$ (**2.1**) exhibited the most negative first and second reduction potentials of the series: –1.94 and –2.68 V vs. $[Cp_2Fe]^{+/0}$, respectively.

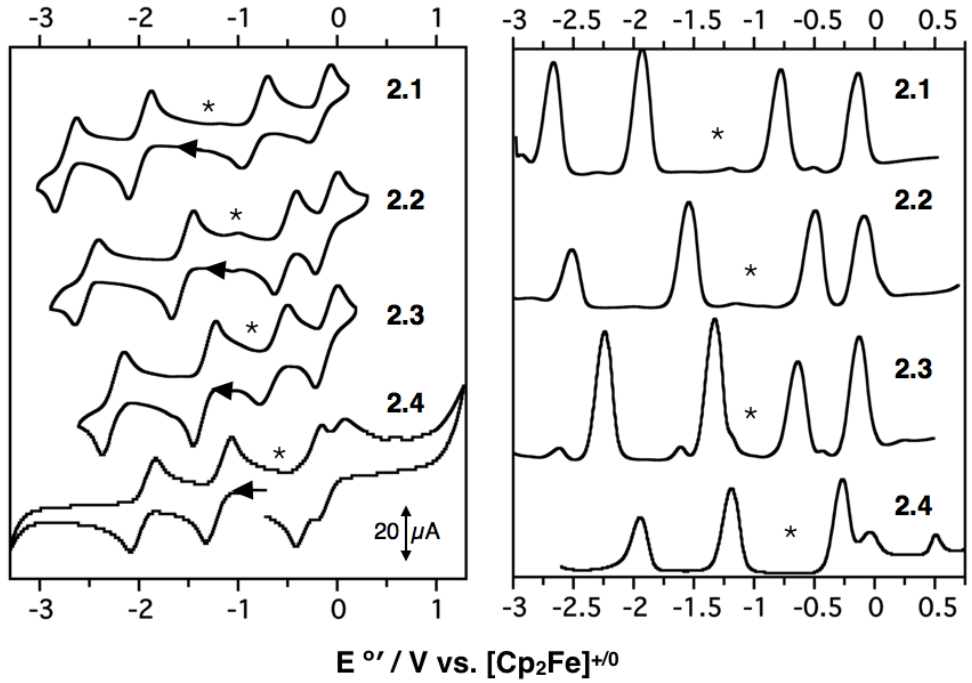

Figure 2.8 Cyclic voltammograms of (pdiol)Ni(bpy^{t}Bu$_2$) (**2.1**), (pdiol)Ni(bdi) (**2.2**), (pdiol)Ni(adi) (**2.3**), and (pdiol)Ni(pdi) (**2.4**) (left) and Differential pulse voltammograms **2.1–2.4** (right). Measurements taken as 1mM solutions in THF containing 0.1 M $[Bu_4N][PF_6]$ supporting electrolyte. Data were collected at a glassy carbon working electrode, with a platinum wire counter electrode, and a silver wire pseudo-reference electrode using a scan rate of 200 mV s^{-1}.

When the acceptor ligand is switched to the exo-cyclic butane-diimine ligand, as is the case with **2.2**, $E°'_3$ shifts anodically by 370 mV. Likewise, when conjugation is introduced into the diimine backbone, as is the case with **2.3,** another cathodic shift of 240 m V to –1.33 V vs. $[Cp_2Fe]^{+/0}$ occurs. The most conjugated exo-cyclic acceptor of the series, pdi is the easiest to reduce, exhibiting the most positive first (and second) reduction potential(s) of the series, –1.19 V vs. $[Cp_2Fe]^{+/0}$. The reduction potentials follow the same trend exhibited by the energy of the band maxima, that is, the exo-cyclic α-diimine acceptor (bpy^{t}Bu$_2$, **2.1**) has the highest energy LUMO, while the energies of the LUMOs residing on the endo-cyclic

α-diimines decrease with increasing conjugation. In total, the energy of the first reduction potential was tuned 0.75 V through variation of the acceptor ligand.

Table 2-4 Reduction Potentials (V vs. $[Cp_2Fe]^{+/0}$) for Complexes **2.1**–**2.4** at 298 K in THF Solution

	E°' / V vs $[Cp_2Fe]^{+/0}$				
	$E°'_1$ $[Ni]^{2+/1}$	**$E°'_2$ $[Ni]^{+/0}$**	**$E°'_3$ $[Ni]^{0/-}$**	**$E°'_4$ $[Ni]^{1-/2-}$**	**$E°'_2 - E°'_3$**
2.1	–0.141	–0.777	–1.93	–2.67	1.15
2.2	–0.15	–0.55	–1.57	–2.52	1.02
2.3	–0.13	–0.63	–1.33	–2.24	0.70
2.4	–0.04	–0.27	–1.19	–1.95	0.92

The first oxidation event ($E°'_2$) corresponds to the removal of an electron from the HOMO localized on the phenanthrenediolate ligand to generate the phenanthrene-seminquinonate donor. For each complex, this event appears within a range of potentials and with varying degrees of reversibility. (pdiol)Ni(bpy^{t}Bu$_2$) (**2.1**) shows a (generally) reversible first oxidation event that is the most negative of the series, with a potential of –0.72 V vs. $[Cp_2Fe]^{+/0}$, indicating that it is most easily oxidized. Complexes **2.2** and **2.3**, exhibit less negative first oxidation potentials at –0.55 and –0.63 V, respectively. While this event appears fully reversible for **2.2,** for **2.3** the return wave is broad and cathodically shifted. Complex **2.4**, exhibited the least negative potential corresponding to the first oxidation event at –0.27 V vs. $[Cp_2Fe]^{+/0}$. It appears fully reversible but almost overlaps with a second oxidation event beginning at –0.14 V vs. $[Cp_2Fe]^{+/0}$.

2.3 Summary

Four new nickel(II) square-planar donor-acceptor complexes have been described in this Chapter where the redox active phenanthrenediolate donor ligand, $(pdiol)^{2-}$ is

paired with a Ni(II) metal ion and perturbations of the LUMO orbital are investigated through the variation of four different α-diimine acceptor ligands. The synthetic method employed herein allows for the independent installation of the donor and acceptor ligands. Where the acceptor ligand is installed first and in its neutral form, the installation of the [donor^{cat}]$^{2-}$ involves a two-step redox reaction that twice oxidizes the Ni(0) synthon and twice reduces the phenanthrenequinone to phenanthrenediolate, (pdiol)$^{2-}$. The ligand field imposed by the square-planar geometry of the Ni(II) ion allows for the HOMO of the donor ligand, and the LUMO of the acceptor ligand to be electronically inserted above the filled and below the empty metal orbitals.

By systematically varying the electronic nature of the α-diimine acceptor ligand we were able to tune the energy of the LL'CT absorption a total of 0.90 eV and the first reduction potential by 0.75 V. The complex equipped with the endo-cyclic bpy^{t}Bu$_2$ acceptor, (pdiol)Ni(bpy^{t}Bu$_2$) (**2.1**) gave rise to HOMO and LUMO orbitals that are energetically well isolated from one another as indicated by exhibiting the highest energy LL'CT transition (1.82 eV) and the largest difference in potentials between the first oxidation and first reduction. The complexes with the exo-cyclic acceptors, **2.2**–**2.4** showed smaller HOMO-LUMO gaps as indicated by their red-shifted absorption profiles and less negative reduction potentials. Within the subgroup of endo-cyclic α-diimine acceptors, as the conjugation increases ingoing from bdi < adi < pdi, the energy of the LUMO is lowered; made evident by less negative reduction potentials following the same order. The trend observed in the electrochemical profiles is also observed in the absorption data where the energy of the LL'CT transitions decreased as such: bdi > adi > pdi. The extent of thermodynamic control over the energies of the frontier molecular orbitals was met with

the pdi ligand where the extended conjugation of the acceptor backbone lead to delocalization across the entire molecule and resulted in the loss of charge-transfer character in the lowest energy transition. Overall, a more comprehensive understanding of the modularity and degree of control over the spectroscopic and electrochemical parameters was made and will be employed in the chapters ahead.

2.4 Experimental

General Considerations. All compounds and reactions reported below show various levels of air- and moisture-sensitivity; therefore all manipulations were carried out using standard vacuum-line, Schlenk-line, and glovebox techniques. Solvents were sparged with argon before being deoxygenated and dried by passage through Q5 and activated alumina columns, respectively. To test for effective oxygen and water removal, aliquots of each solvent were treated with a few drops of a purple solution of sodium benzophenone ketyl radical in THF. The reagents: phenanthrenequinone, (Acros); 4,4'-di-*tert*-butyl-2,2'-bipyridine, bpy^{t}Bu$_2$ (Sigma); and Ni(cod)$_2$ (Strem) were reagent grade or better and used as received. The exo-cyclic α-diimine ligands: *N,N*'-bis(2,4,6-trimethylphenyl)-2,3-butanediimine (bdi)[28]; *N,N*'-bis(2,4,6-trimethylphenyl)acenaphthenediimine (adi)[29], and *N,N*'-bis(2,4,6-trimethylphenyl)-9,10-phenanthrenediimine (pdi)[30] were prepared according to published procedures.

Spectroscopic Measurements. NMR spectra were collected at 298 K on a BrukerAvance 400 MHz or 500 MHz spectrometer in dry, degassed, d_8-THF, C_6D_6, or $CDCl_3$. ^{1}H NMR spectra were referenced to tetramethylsilane (TMS) using the residual ^{1}H impurities of the deuterated solvent. All chemical shifts are reported using the standard δ

notation in parts per million; positive chemical shifts are to a higher frequency of TMS. Electronic absorption spectra were recorded with a PerkinElmer Lamda 900 UV-vis-NIR Spectrometer using one-centimeter path-length cells at ambient temperature (20-24 °C).

Electrochemical Methods. Electrochemical experiments were recorded on a Gamry Series G300 potentiostat/galvanostat/ZRA (Gamry Instruments, Warminster, PA) using a 3.0 mm glassy carbon working electrode, a platinum wire auxiliary electrode, and a silver wire pseudo-reference electrode. Reversibility of a redox process was judged based on the ratio of the anodic to the cathodic current being close to unity (ipa/ipc ≅ 1) for a given process. Electrochemical experiments were performed at ambient temperature (20-24 °C) in a nitrogen-filled glovebox using THF solutions containing 1 mM analyte and 100 mM $[NBu_4][PF_6]$ as the supporting electrolyte. All potentials are referenced to $[Cp_2Fe]^{+/0}$ using ferrocene or decamethylferrocene (−0.49 V vs $[Cp_2Fe]^{+/0}$)[26] as internal standards. Ferrocene and decamethylferrocene (Acros) were purified by sublimation under reduced pressure and tetrabutylammonium hexafluorophosphate (Acros) was recrystallized from ethanol three times and dried under vacuum.

X-ray Data Collection and Reduction. X-ray diffraction data for all complexes were collected on single crystals mounted on either a glass fiber or a cryoloop and coated with oil. Data were acquired using a Bruker SMART APEX II diffractometer at 143 K using Mo Kα radiation (λ = 0.71073 Å). The APEX2[27] program package was used to determine unit-cell parameters and for data collection. The raw frame data were processed using SAINT[28] and SADABS[29] to yield the reflection data file. Subsequent refinement cycles were carried out using the SHELXTL program suite.[30] Analytical scattering factors for neutral atoms were

used throughout the analyses.[31] ORTEP diagrams were generated using ORTEP-3 for Windows.[32] Diffraction data for **2.1**–**2.4** is given in **Table 2-4.**

Table 2-5 Diffraction Data for Complexes **2.1–2.4**

	(pdiol)Ni(bpy^{t}Bu$_2$) **2.1**	(pdiol)Ni(bdi) **2.2**	(pdiol)Ni(adi) **2.3**	(pdiol)Ni(pdi) **2.4**
empirical formula	$C_{32}H_{32}N_2O_2Ni$	$C_{36}H_{36}N_2O_2Ni$	$C_{44}H_{36}N_2O_2Ni$	$C_{46}H_{38}N_2O_2Ni\bullet$ ¼(C_6H_6)
formula weight	535.29	587.38	683.46	729.02
crystal system	Monoclinic	Monoclinic	Monoclinic	Triclinic
space group	$P2_1/n$	$P2_1/n$	C2/c	P Ī
a/ Å	16.0397(17)	11.5185(7)	17.5572(17)	11.7093(6)
b/ Å	9.7965(10)	14.8995(9)	23.260(2)	19.2228(10)
c/ Å	17.3067(18)	17.7806(10)	8.5639(8)	20.4554(11)
α/deg	90.00	90.00	90.00	105.1048(7)
β/deg	107.6518(13)	91.4097(7)	109.2445(12)	103.0242(7)
γ/deg	90.00	90.00	90.00	107.2972(7)
V /Å^3	2591.4(5)	3050.6(3)	3301.9(5)	4008.5(4)
Z	4.00	4.00	4.00	4.00
refl collected	45818	33246.00	18153.00	49543.00
indep refl	9470	6725	4182.00	19320.00
R_1	0.0393	0.05	0.04	0.04
wR_2	0.09	0.11	0.10	0.10

Synthesis of (pdiol)Ni(bpy^{t}Bu$_2$) (**2.1**): Complex **2.1** was prepared by treating Ni(cod)$_2$ (0.069g, 0.25 mmol, 1 equiv) with one equivalent of 4,4'-di-*tert*-butyl bipyridine (0.067g, 0.25 mmol, 1 equiv) to generate a dark purple solution. The (cod)Ni(bpy^{t}Bu$_2$) intermediate was then treated with one equivalent of 9,10 phenanthrenequinone (0.052 g, 0.25 mmol, 1 equiv) and stirred for 8 hours. The resulting dark green solution was filtered and the precipitate washed with cold pentane to yield **2.1** as an evergreen solid (95 mg,

71% yield). ^{1}H NMR (400 MHz, $CDCl_3$) δ 8.94 = (d, *J* = 5.7 Hz, 2H), 8.19 (d, *J* = 8.31 Hz, 2H), 8.11 (d, *J* = 7.92 Hz, 2H), 7.51 (s, 2H), 7.44 (t, *J* = 15.0, 7.14, 2H), 7.40 (d, *J* = 5.37, 2H) 7.26 (t, *J* = 14.8, 7.68, 2H), 1.37 (s, 18H). ^{13}C NMR (126 MHz; $CDCl_3$) δ/ ppm: 163.1 (*C*=N), 152.9 (*C*–O), 149.2 (aryl–*C*), 147.0 (aryl–*C*), 128.9 (aryl–*C*), 124.5(aryl–*C*), 124.2 (aryl–*C*), 122.3(aryl–*C*), 120.4 (aryl–*C*), 119.7 (aryl–*C*), 116.8 (aryl–*C*), 135.4 (–*C*(CH_3)$_3$), 130.3 (–C(*C*H_3)$_3$). UV-vis-NIR [THF; λ_{max}/nm (ε/M^{-1} cm^{-1})]: 680 (3826), 370 (15963).

Synthesis of (pdiol)Ni(bdi) (**2.2**). Complex **2.2** was prepared using *N,N*'-bis(2,4,6-trimethylphenyl)-2,3-butanediimine (160 mg, 0.5 mmol, 1 equiv), $Ni(cod)_2$ (138 mg, 0.5 mmol, 1 equiv), and 9,10-phenanthrenequinone (104 mg, 0.5 mmol, 1 equiv) in benzene. The product was isolated as a green microcrystalline solid and purified by recrystallization with THF and pentane and subsequent washing with cold pentane to yield a forest green microcrystalline solid (189 mg, 64% yield). X-ray quality crystals were grown by vapor diffusion of pentane into a solution of **2.2** in THF. ^{1}H NMR (500 MHz; d_8-THF) δ/ppm: 1.74 (*s*, 6H), 1.74 (*s*, C=N-Me, 6H), 2.40 (*s*, p-Me, 6H), 2.48 (*s*, *o*-Me, 12H), 7.05 (*m*, 8H), 7.36 (*d*, J= 7.8, 2H), 8.27 (*d*, J = 7.9, 2H). ^{13}C NMR (126 MHz; d_8-THF) δ/ ppm: 169.2 (*C*=N(CH_3)), 151.6 (*C*–O), 143.0 (aryl–*C*), 137.0 (aryl–*C*), 131.7 (aryl–*C*), 129.5 (aryl–*C*), 129.3 (aryl–*C*), 129.1 (aryl–*C*), 125.5 (aryl–*C*), 125.0 (aryl–*C*), 122.6 (aryl–*C*), 121.4 (aryl–*C*), 120.6 (aryl–*C*), 21.6 (*p*-*C*H_3), 19.1 (*o*-*C*H_3), 17.8 (*C*=N(CH_3)). Anal. Calcd for $C_{36}H_{36}N_2O_2Ni$: C, 73.61; H, 6.18; N, 4.77. Found: C, 73.23; H, 6.13; N, 4.46. UV–vis–NIR [THF; λ_{max}/nm (ε/M^{-1} cm^{-1})]: 420 (3500), 1090 (8500).

Synthesis of (pdiol)Ni(adi) (**2.3**). Complex **2.3** was prepared using *N,N*′-bis(2,4,6-trimethylphenyl)-acenaphthenediimine (104 mg, 0.25 mmol, 1 equiv), $Ni(cod)_2$ (69 mg, 0.25 mmol, 1 equiv), and 9,10-phenanthrenequinone (52 mg, 0.25 mmol, 1 equiv) in

benzene. The product was isolated as a brownish green solid. X-ray quality crystals of **2.3** were obtained by layering a THF solution of the complex with pentane (70 mg, 47% yield). ^{1}H NMR (500 MHz; d_8-THF) δ/ppm: 2.47 (*s*, *p*–Me, 6H), 2.61 (*s*, *o*–Me, 12H), 6.81 (*s*, 2H), 7.16 (*m*, 8H), 7.29 (s, 1H), 7.45 (*s*, 2H), 7.51 (*s*, 2H), 8.32 (*s*, 2H). ^{13}C NMR (126 MHz; d_8-THF) δ/ppm: 166.3 (*C*=N), 152.2 (*C*–O), 142.6 (aryl–*C*), 142.1 (aryl–*C*), 136.7 (aryl–*C*), 131.6 (aryl–*C*), 131.4 (aryl–C), 129.9 (aryl–*C*), 129.3 (aryl–*C*), 128.8 (aryl–*C*), 128.1 (aryl–*C*), 127.3 (aryl–*C*), 125.5 (aryl–*C*), 124.6 (aryl–*C*), 122.3 (aryl–*C*), 121.9 (aryl–*C*), 121.7 (aryl–*C*), 120.0 (aryl–*C*), 20.5 (*p*–*C*H$_3$), 17.9 (*o*–*C*H$_3$). UV–vis–NIR [THF; λ_{max}/nm (ε/M^{-1} cm^{-1})]: 328 (25 054), 1310 (9920).

Synthesis of (pdiol)Ni(pdi) (**2.4**). Complex **2.4** was prepared using N,N′-bis(2,4,6-trimethylphenyl)-9,10-phenanthrenediimine (180 mg, 0.25 mmol, 1 equiv), Ni(cod)$_2$ (69 mg, 0.25 mmol, 1 equiv), and 9,10-phenanthrenequinone (52 mg, 0.25 mmol, 1 equiv) in benzene. Recrystallization with benzene and pentane yielded the product as a dark brown/amber microcrystalline solid (150 mg, 85% yield). Layering a benzene solution of **2.4** with pentane resulted in the precipitation of X-ray quality crystals. ^{1}H NMR (400 MHz; C$_6$D$_6$) δ/ppm: 2.39 (*s*, o-Me, 6H,), 2.50 (*s*, p-Me, 12H), 6.83 (*t*, J = 7.8, 2H), 7.05 (*s*, 4H,), 7.08–7.14 (*m*, 4H), 7.32 (*t*, J = 7.5, 2H), 7.83 (*d*, *J* = 8.4, 2H), 7.79 (*d*, J= 8.6, 2H), 7.97 (*d*, J = 7.8, 2H), 8.08 (*d*, J = 8.1, 2H). ^{13}C NMR (126 MHz; C$_6$D$_6$) δ/ppm: 161.2 (*C*–O), 154.0 (*C*=N), 147.5 (aryl–*C*), 136.2 (aryl–*C*), 133.3 (aryl–*C*), 131.1 (aryl–*C*), 128.9 (aryl–*C*), 128.8 (aryl–*C*), 128.6 (aryl–*C*), 128.4 (aryl–*C*), 128.4 (aryl–*C*), 127.9 (aryl–*C*), 126.6 (aryl–*C*), 126.0 (aryl–*C*), 125.7 (aryl–*C*), 124.6 (aryl–*C*), 123.2 (aryl–*C*), 122.4 (aryl–*C*), 21.6 (p-*C*H$_3$), 19.6 (*o*-*C*H$_3$). Anal. Calcd for C$_{46}$H$_{38}$N$_2$O$_2$Ni: C, 77.87; H, 5.40; N, 3.95. Found: C, 77.55; H, 7.30; N, 3.62. UV–vis–NIR [THF; λ_{max}/nm (ε/M^{-1} cm−1)]: 370 (1600), 1370 (43 000).

2.5 References

(1) Zhao, Y.; Liang, W. *Chem. Soc. Rev.* **2012**, *41*, 1075.
(2) McCusker, J. K. *Science* **2001**, *293*, 1599–1601.
(3) Balzani, V.; Bergamini, G.; Campagna, S.; Puntoriero, F. Photochemistry and Photophysics of Coordination Compounds: Overview and General Concepts. Topics in Current Chemistry; Springer Berlin Heidelberg: Berlin, Heidelberg, 2007; Vol. 280, pp. 1–36.
(4) Nozik, A. J. *Annu. Rev. Phys. Chem.* **1978**, *29*, 189–222.
(5) Hagfeldt, A.; Grätzel, M. *Acc. Chem. Res.* **2000**, *33*, 269-277.
(6) O'Regan, B.; Grätzel, M. *Nature* **1991**, *353*, 737–740.
(7) Islam, A.; Sugihara, H.; Hara, K.; Singh, L. P.; Katoh, R.; Yanagida, M.; Takahashi, Y.; Murata, S.; Arakawa, H.; Fujihashi, G. *Inorg. Chem.***2001**, *40*, 5371–5380.
(8) Preat, J.; Jacquemin, D.; Perpète, E. A. *Energy Environ. Sci.* **2010**, *3*, 891–904.
(9) Zhang, S.; Yang, X.; Numata, Y.; Han, L. *Energy Environ. Sci.* **2013**, *6*, 1443.
(10) Grätzel, M. *Inorg. Chem*. **2005**, *44*, 6841-6851.
(11) McConnell, I.; Li, G.; Brudvig, G. W. *Chemistry & Biology* **2010**, *17*, 434–447.
(12) Gust, D.; Moore, T. A.; Moore, A. L. *Acc. Chem. Res.* **2009**, *42*, 1890–1898.
(13) Gong, Z.-Y.; Duan, S.; Tian, G.; Zhang, G.; Jiang, J.; Luo, Y. *J. Phys. Chem. A* **2016**, *120*, 3547–3553.
(14) Chakraborty, S.; Wadas, T. J.; Hester, H.; Schmehl, R.; Eisenberg, R. *Inorg. Chem.* **2005**, *44*, 6865–6878.
(15) Alstrum-Acevedo, J. H.; Brennaman, M. K.; Meyer, T. J. *Inorg. Chem.* **2005**, *44*, 6802–6827.
(16) Hanna, M. C.; Nozik, A. J. *J. Appl. Phys.* **2006**, *100*, 074510.
(17) Cook, T. R.; Dogutan, D. K.; Reece, S. Y.; Surendranath, Y.; Teets, T. S.; Nocera, D. G. *Chem. Rev.* 2010, 10, 6474-6502 (18) Kramer, W. W.; Cameron, L. A.; Zarkesh, R. A.; Ziller, J. W.; Heyduk, A. F. *Inorg. Chem.* **2014**, 140806135722006.
(19) Vogler, A.; Kunkely, H. *Comments on Inorganic Chemistry* **1990**, *9*, 201–220.
(20) Pierpont, C. G.; Downs, H. H.; Rukavina, T. G. *J. Am. Chem. Soc.* **1974**, *96*, 5573–5574.
(21) Bhattacharya, S.; Pierpont, C. G. *Inorg. Chem.* **1992**, *31*, 35–39.
(22) Brown, S. N. *Inorg. Chem.* **2012**, *51*, 1251–1260.
(23) Biner, M.; Buergi, H. B.; Ludi, A.; Roehr, C. *J. Am. Chem. Soc.* **1992**, *114*, 5197–5203.
(24) Muresan, N.; Chlopek, K.; Weyhermüller, T.; Neese, F.; Wieghardt, K. *Inorg. Chem.***2007**, *46*, 5327–5337.
(25) Abakumov, G. A.; Cherkasov, V. K.; Bubnov, M. P.; Éllert, O. G.; Rakitin, Y. V.; Zakharov, L. N.; Struchkov, Y. T.; Saf'yanov, Y. N. *Russ Chem Bull* **1992**, *41*, 1813–1818.
(26) Manuta, D. M.; Lees, A. J. *Inorg. Chem.* **1986**, *25*, 3212–3218.
(27) Cummings, S. D.; Eisenberg, R. *J. Am. Chem. Soc.* **1996**, *118*, 1949–1960.

Chapter 3

Near-IR Absorbing Ni(II)(bipyridyl) LL′CT Complexes Supported By the Redox-Active Amidophenolate Donor Ligand

3.1 Introduction

Over the course of millennia nature has developed highly complex photosystems to utilize as much of the visible solar spectrum as efficiently as possible in order to fuel important chemical reactions. Within these photosystems, multiple light harvesters or chromophores are tuned to absorb specific wavelengths. Where some chromophores absorb high-energy light in the blue and violet regions (380-500 nm), others absorb lower-energy red and NIR photons (620-1000 nm). For example, the primary photosynthetic pigment used in land plants, Chlorophyll *a*, absorbs photons around 680 nm while it's complimentary pigment; Chlorophyll *b* absorbs photons of shorter wavelengths (400-500 nm, **Figure 3.1**, green trace). These natural dyes in Photosystem II work in tandem to harness enough photon energy to power crucial chemical reactions such as water oxidation and NADP+ reduction.[1,2]

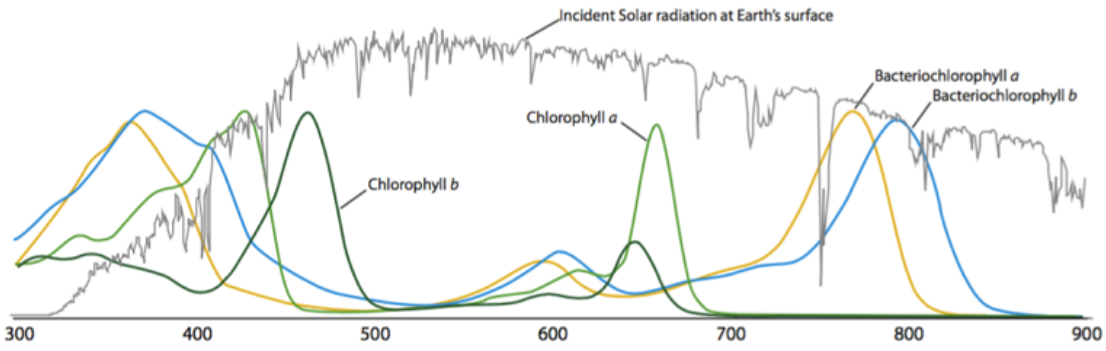

Figure 3.1 Solar spectrum utilization by natural chromophores. Figure taken from Ref. 1

Anaerobic photosynthetic light harvesters such as bacteriochlorophyll *a* and *b* (**Figure 3.1**, yellow and blue trace) are designed utilize even lower-energy light to drive anaerobic processes such as trans membrane proton translocation.[1,2] The light harvesting dyes nature has developed appears to follow certain criteria: 1) the λ_{max} of the dye should

absorb within an area of peak photon flux, and 2) the onset of the lowest energy absorption (E_{hv}) should align with the longest wavelength available within the limitation that the photon absorbed must have enough energy to fuel the desired chemical reactions.[2] In our efforts to design LL′CT dyes relevant to enhancing the scalability and efficiency of solar energy conversion strategies, we look to nature's design for inspiration. Where nature has learned to employ earth abundant metal ions to enhance light-harvesting throughout the visible region and into the near-infrared (NIR), we too can design coordination complexes of non-precious metal ions that utilize NIR photons to access potent excited-states.[3-5] Complexes based on LL′CT transitions provide a promising platform to realize such a dye. Earth-abundant donor-acceptor LL′CT chromophores can be designed to act as a potent excited-state reductant through the correct choice of metal ion, donor and acceptor ligand.

A strongly reducing NIR photosensitizer can be realized through the optimization of the thermodynamic parameters discussed in Chapter 1, specifically the energy of the photon absorbed and the dye's excited-state oxidation potential ($E^{+/*}$).[6] A 'red-absorbing' photosensitizer should absorb photons as low as 1.0 eV to access excited state reduction potential capable of performing important electron transfer reactions, such as electron injection into large band-gap semiconductors.

Given that bipyridyl-type ligands are known to inject electrons into the conduction band of TiO_2,[7-9] for this series of LL′CT dyes, we chose 4,4'-di-*tert*-butyl-2,2'-bipyridine (bpy^tBu_2) and 1,10-phenanthroline (phen) to be acceptor ligands. The redox-active amidophenolate ligand was chosen as the donor. Amidophenolates can be viewed as a hybrid between *ortho*-phenylenediamines and catecholate derivatives with their specific

structures, 2,4-di-*tert*-butyl-6-((2,6-diisopropylphenyl)amidophenolate $(ap)^{2-}$ and phenanthren-9,10((2,6-diisopropylphenyl)amidophenolate) $(ap^{Ph})^{2-}$, shown in **Chart 3–1.**

Chart 3-1 a) The accessible oxidation-states of the amidophenolate donor ligand and b) specific amidophenolate ligands used in this study.

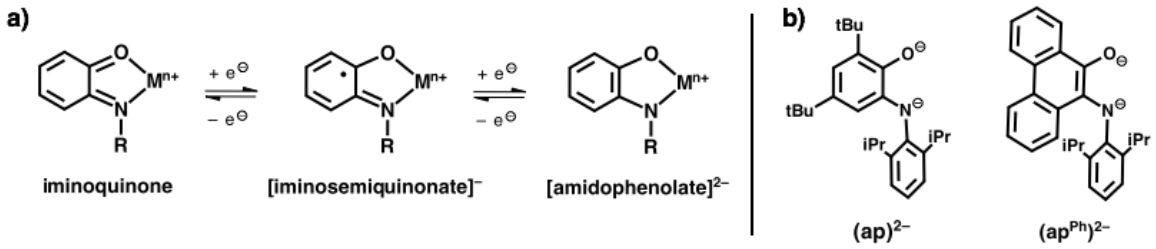

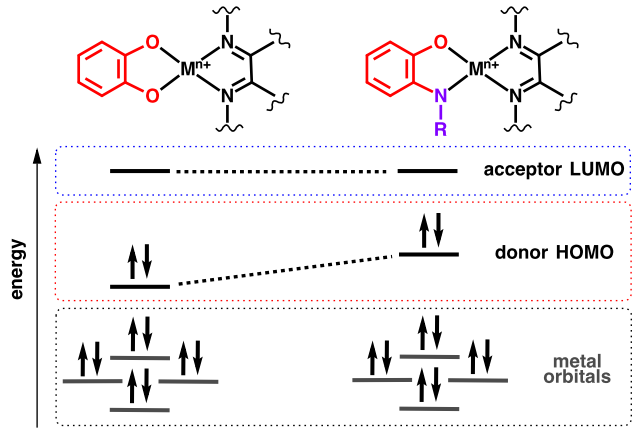

Figure 3.2 Qualitative molecular orbital diagram of catecholate vs. amidophenolate donor-acceptor complexes.

Derivatives of these ligands have been thoroughly studied in our lab and others where it has been shown they can coordinate to a transition metal ion in their dianionic, monoanionic, and neutral forms.[10-13] They have redox chemistry analogous to catecholates and *ortho*-phenylenediamines. Electrochemical studies of $[Ru(ap)(bpy)_2]^{2+}$ complexes conducted by Lever et al. demonstrated the strong reducing power of the amidophenolate ligand by showing for every oxygen atom replaced with a nitrogen atom, the ligand reduction potential became 0.5 V more negative. The observed cathodic shift was

attributed to the amido-based HOMO being higher in energy when compared to the catecholate-centered HOMO in analogous complexes, and is illustrated in **Figure 3.2**. Based on the observed perturbations to the HOMO orbital, NIR or 'red absorbing' dyes can be realized by the incorporation of a strongly reducing amidophenolate as the donor ligand.[14]

To examine the effects the $(ap)^{2-}$ and $(ap^{Ph})^{2-}$ have on the photo-physical and electrochemical properties of square planar Ni(II)bipyridyl dyes, this chapter will discuss the synthesis, characterization, and experimental analysis of donor-acceptor LL'CT chromophores with the general formula: (amidophenolate)Ni^{II}(bipyridyl) where amidophenolate = $(ap)^{2-}$ and $(ap^{Ph})^{2-}$; and bipyridyl = 4,4'-di-*tert*-butyl-2,2'-bipyridine (bpy^tBu_2) and 1,10-phenanthroline (phen). These new square-planar dyes were examined against a catecholate derivative in order to quantify perturbations on the HOMO by the amidophenolate ligands and estimate the redox potentials of the excited-state.

3.2 Results and Discussion

3.2.1 Synthesis and Structural Characterization

Donor-acceptor (D-A) nickel(II) complexes were prepared by utilizing the ability of *ortho*-quinones and *ortho*-iminoquinones to act as two-electron oxidants.[15] As discussed in Chapter 2, installation of the catecholate ligand is achieved by a two electron oxidation of the Ni(0) synthon upon addition of the donor in its neutral quinone form. Following this example, and shown **Scheme 3-1**, a new family of charge-transfer complexes were synthesized through treatment of $Ni(cod)_2$ with the bipyridyl acceptor to generate the putative (cod)$nickel^0$(bipyridyl) intermediate. Subsequent addition of the $donor^q$ ligand resulted in a two-electron oxidation of Ni(0) to Ni(II) and a two- electron reduction of

donor^{q} to (donor^{cat})$^{2-}$. The redox reaction was indicated by a drastic color change from dark purple to deep green (complex **3.1** was blue) and afforded the square planar nickel complexes: (cat)Ni(bpy^{t}Bu$_2$) (**3.1**), (ap)Ni(bpy^{t}Bu$_2$) (**3.2**), (ap)Ni(phen) (**3.3**), and (ap^{Ph})Ni(bpy^{t}Bu$_2$) (**3.4**) in good yields (66-81%).

Scheme 3-1 Synthetic route used to access (donor)Ni^{II}(bipyridyl) dyes (top) and the donor and acceptor ligands used in this study (bottom).

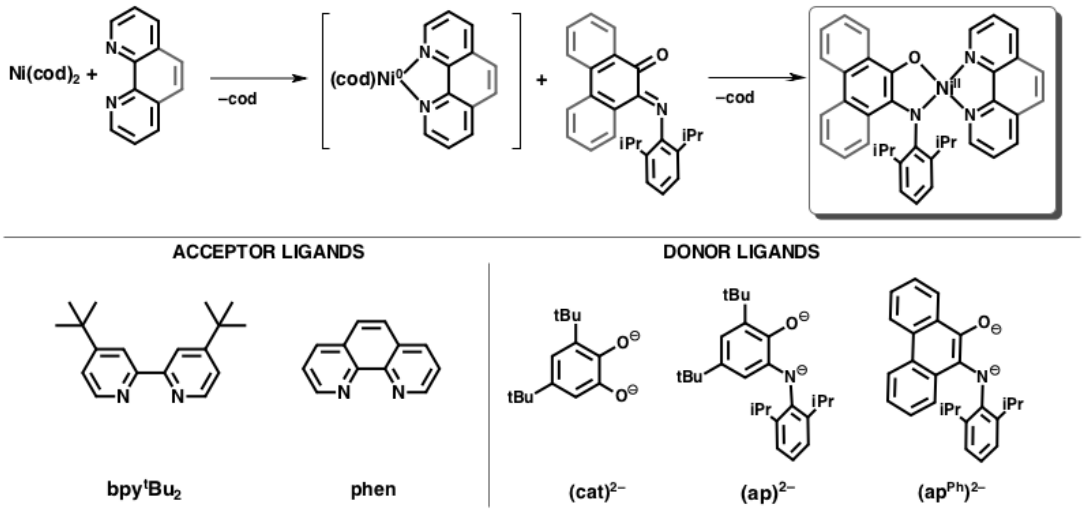

High-resolution single-crystal X-ray diffraction studies were used to confirm gross structural features and to make unambiguous oxidation-state assignments of the nickel ion, donor ligand, and acceptor ligand. **Figure 3.4** shows the ORTEP diagrams of complexes **3.1**–**3.4** and **Table 3-1** lists their relevant bond distances. Each complex within the series adopted the expected square-planar geometry, consistent with diamagnetic, d^8 nickel(II) metal centers. Regarding the donor ligands, the amidophenolate O–Ni–N bite angles within complexes **3.2** and b measure 86°. The catecholate ligand of **3.1** expectedly deviates from the above trend displaying a wider O–Ni–O bite angle of 89°.

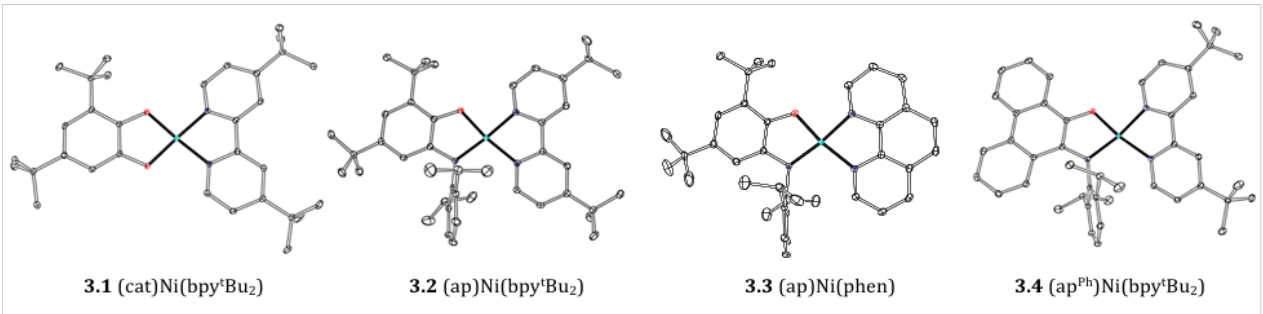

Figure 3.3 ORTEP diagrams of **3.1–3.4.** Thermal ellipsoids are shown at 50% probability. Hydrogen atoms and non-coordinated solvent molecules (if present) have been omitted for clarity.

Table 3-1 Selected Bond Distances (Å) for **3.1–3.4**, including the Metrical Oxidation State (MOS).[13]

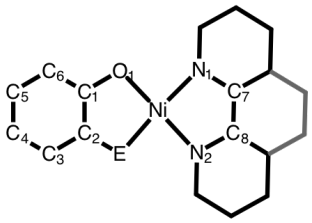

Bond Distances / Å

	3.1	**3.2**	**3.3**	**3.4**
Ni-O(1)	1.8227(11)	1.8329(17)	1.874(14)	1.8212(8)
Ni-E	1.8273(11)	1.868(2)	1.8583(17)	1.8798(10)
Ni-N(1)	1.8804(14)	1.908(2)	1.9105(17)	1.9048(10)
Ni-N(2)	1.8868(13)	1.942(2)	1.9497(17)	1.9350(10)
O(1)-C(1)	1.3574(18)	1.360(3)	1.349(2)	1.3401(14)
E-C(2)	1.3538(18)	1.389(3)	1.394(3)	1.3936(14)
C(1)-C(2)	1.407(2)	1.404(3)	1.402(3)	1.3871(16)
C(2)-C(3)	1.390(2)	1.398(3)	1.395(3)	1.4537(16)
C(3)-C(4)	1.400(2)	1.387(4)	1.395(3)	1.4374(16)
C(4)-C(5)	1.400(2)	1.390(4)	1.391(3)	1.4512(17)
C(5)-C(6)	1.405(2)	1.411(3)	1.402(3)	1.4222(17)
C(1)-C(6)	1.408(2)	1.392(3)	1.398(3)	1.4224(16)
N(2)-C(8)	1.3569(19)	1.346(3)	1.369(3)	1.3496(15)
N(1)-C(7)	1.3614(19)	1.358(3)	1.360(3)	1.3659(15)
C(7)-C(8)	1.471(2)	1.459(3)	1.417(3)	1.4692(16)
MOS	**–1.90**	**–1.89**	**–1.86**	**N/A**

The donor in **3.4**, $(ap^{Ph})^{2-}$ displays the widest O–Ni–E bite angle of the series at 92°. Complexes with the same bpy^{t}Bu$_2$ acceptor ligand (**3.1**, **3.2**, and **3.4**) show consistent N–Ni–N bite angles ranging from 82–83°. The more conjugated phenanthroline (phen) acceptor ligand in **3.3** has a slightly wider N–Ni–N bite angle of 84°. Regardless, all measured bite angles indicate nearly square planar geometry.

The oxidation state of the donor, acceptor, and metal center can be determined by evaluating key bond lengths within the ligand platform. For example, the LUMO of each molecule is localized on the π* orbital of the acceptor ligand, therefore population of the LUMO would cause a contraction of the bridgehead C(7)–C(8) bond length and an elongation of the C–N distances when compared to neutral forms of the ligands, which are 1.45 Å and 1.36 Å, respectively. The acceptor ligands of **3.1, 3.2**, and **3.4** show an average bridgehead C(7)–C(8) bond distance of 1.46 Å and an average C–N distance of 1.36 Å coinciding with a fully oxidized, neutral bipyridyl.[16] We expect similar results if the LUMO of **3.3** was populated. As such, the phenanthroline acceptor ligand in **3.3** exhibits a bridgehead C(7)–C(8) length of 1.42 Å and an average C–N distance of 1.36 Å, coinciding with an acceptor ligand in its neutral form.[17] The donor ligands in each complex show C–O distances of 1.34–1.36 A˚ and C–N distances of 1.39 A˚. Both are longer than observed C=O distances of 1.23 Å and C=N distances of 1.27 Å for neutral quinone ligands and are consistent with carbon–hetero single bonds observed in dianionic catecholate and amidophenolate ligands.[18] These values for both the catecholate and amidophenolate ligands are consistent with fully reduced, dianionic donor ligands.

In addition to direct bond distance comparison, the oxidation state of the donor was confirmed by determining the metrical oxidation state (MOS) value of **3.1**–**3.3**.[13] Due to the

extensive crystallographic database of redox-active amidophenolate and catecholate ligands in unambiguous oxidation states compiled by Brown et al., the qualitative correlation between bond length and oxidation state can be made quantitative.[13] The MOS assignment gives a single calculated value that describes the oxidation state of the donor ligands. For example, a donor with an MOS value of –1.6 is considered to be in catecholate form; donors with MOS values between –1.5 and –0.5 are indicative of the semiquinonate oxidation state; and a MOS value of –0.5 or below indicate a quinone oxidation state. As such, the calculated MOS value for the catecholate ligand in **3.1** is –1.90. The MOS values for the $(ap)^{2-}$ ligand in **3.2** and **3.3** is –1.89 and –1.86, respectively. Complex **3.4** with the $(ap^{Ph})^{2-}$ was excluded from the studies of Seth Brown and therefore its MOS could not be derived.[13] The available structural data strongly supports a (donor)Ni^{II}(bipyridyl) electronic structure for **3.1**, **3.2**, **3.3**, and **3.4**, with either a dianionic catecholate or amidophenolate ligand acting as the electron-rich donor and a neutral bpy^{t}Bu$_2$ or phenanthroline ligand acting as the electron-poor acceptor.

Consistent with a d^8 metal center and square planar geometry, complexes **3.1–3.4** are diamagnetic, and thus the formation of the desired complexes can be confirmed by ^{1}H and ^{13}C NMR spectroscopies. The ^{1}H NMR spectrum of (cat)Ni(bpy^{t}Bu$_2$) **3.1** shows a sharp singlet for the *tert*-butyl proton resonances of the bpy^{t}Bu$_2$ ligand where there should be two, due to the unsymmetrical nature of 3,5-di-*tert*-butyl-1,2-catecholate ligand. Neither a high field NMR spectrometer or lower acquisition temperatures were able to resolve the *tert*-butyl resonance, however, the Cs symmetry was apparent in ^{13}C NMR. Complex **3.1** showed clear evidence of the methyl and tertiary carbons in their expected regions. Complexes **3.2**–**3.4** showed sharp and well resolved resonances for the aromatic protons of

the donor and acceptor ligands. The isopropyl groups of each give rise to a septet near 4.5 ppm for the methine proton and a pair of doublets near 1.2 and 1.3 ppm for the chemically different methyl protons, consistent with the Cs symmetry. In contrast, the *tert*-butyl resonances of the bpy^{t}Bu$_2$ ligand in **3.2** appear as two broad singlets (0.72 and 0.91 ppm). Likewise, the *tert*-butyl resonances of **3.4** appear as a single broad peak at 0.89 ppm. The broadness of **3.2**'s resonances and the fact that **3.4** only showed once resonance where there should have been two prompted us to investigate the fluxional behavior of the bpy^{t}Bu$_2$ using variable-temperature (VT) ^{1}H NMR spectroscopy.

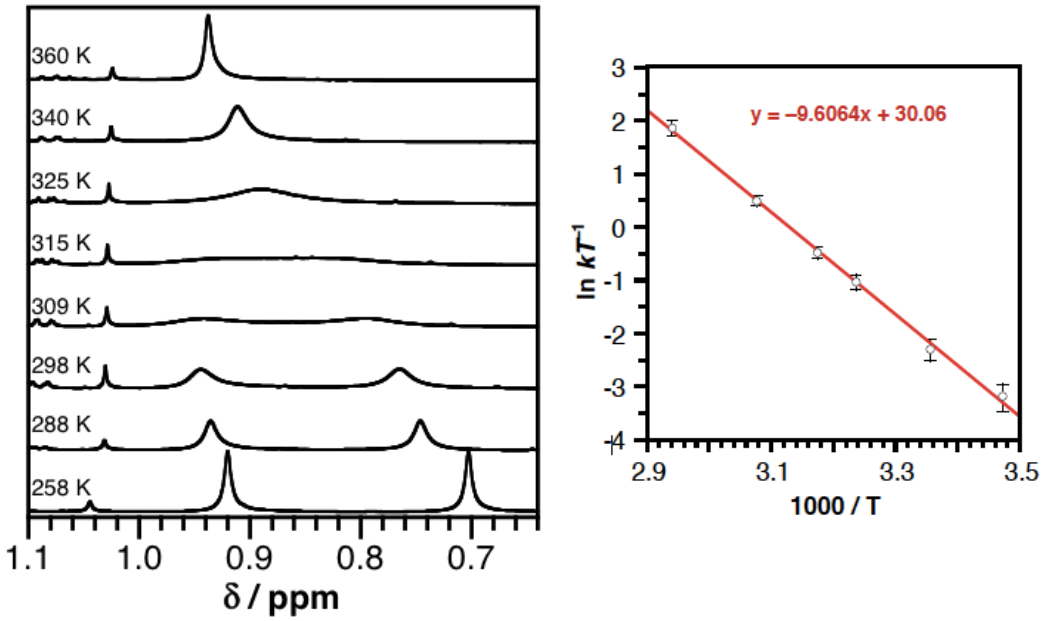

Figure 3.4 Partial ^{1}H NMR spectra (500 MHz) of (ap)Ni(bpy^{t}Bu$_2$) (**3.2**) in toluene-d_8 showing the *tert*-butyl proton resonances of the bpy^{t}Bu$_2$ acceptor ligand over the temperature range 258–360K (left) and Eyring plot (right).

The ^{1}H NMR spectra of the *tert*-butyl groups of the (bpy^{t}Bu$_2$) ligand of **3.2** in toluene-d_8 over the temperature range 258–360 K are shown in **Figure 3.4,** *left*. A linear temperature correction for this chemical shift at each temperature was applied and a transverse relaxation time (T2) of 0.08 s was estimated from the peak-width at half

maximum. First-order rate constants for the exchange were estimated between 288 K and 340 K and these values were used to construct an Eyring plot (**Figure 3.4,** *right*) that yielded transition state energies of $\Delta H‡ = 19.1 \pm 1.5$ kcal mol^{-1} and $\Delta S‡ = 12 \pm 5$ cal mol^{-1} K^{-1} for **3.2** and $\Delta H‡ = 17.6 \pm 1.4$ kcal mol^{-1} and $\Delta S‡ = 15 \pm 5$ cal mol^{-} K^{-1} for **3.4**. While such activation parameters are often attributed to ligand dissociation processes, reactions between **3.2** and excess 2,2'bipyridine indicate that complete dissociation of the acceptor ligand is not responsible for the dynamic behavior observed in the VT NMR experiments. Instead, we think the dynamic behavior is likely an intramolecular isomerization process. One possibility would be a molecular twist to a tetrahedral transition state. A second possibility would be for the dissociation of one arm of either the donor or the acceptor ligand to give a three-coordinate intermediate (without complete loss of the ligand). At elevated temperatures, isomerization by either process could be fast enough that the two sides of the bpy^{t}Bu$_2$ ligand are equivalent on the NMR timescale.

3.2.1 Electrochemistry

The ground-state redox properties of the nickel(II) charge-transfer complexes were probed by cyclic voltammetry. **Figure 3.5** shows the cyclic voltammograms for each complex and **Table 3-2** summarizes their electrochemical potentials for two one-electron reductions and two one-electron oxidations. All potentials are reported relative to the $[Cp_2Fe]^{+/0}$ couple using an internal standard. As expected, all complexes show similar potentials for the first reduction ($E°'_3$ $[Ni]^{0/-}$) averaging, –2.05 V and second reduction process ($E°'_4$ $[Ni]^{-1/-2}$) averaging –2.77 V, as such negative potentials are characteristic of

bipyridine and phenanthroline ligands.[19] In contrast, the first oxidation potential for every complex, $E^{\circ\prime}_2$ $[Ni]^{+/0}$, is highly sensitive to the identity of the donor ligand.

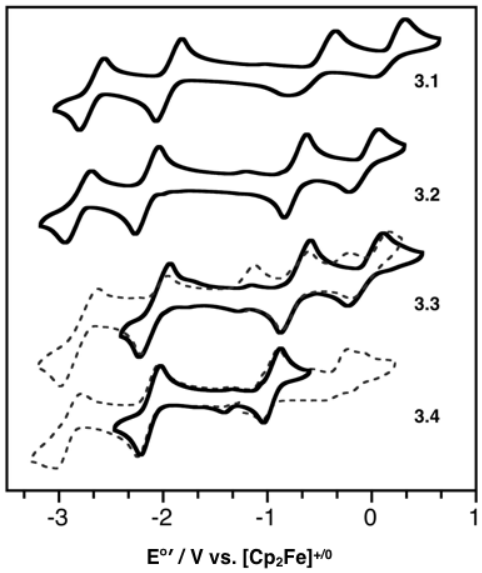

Figure 3.5 Cyclic voltammograms of (cat)Ni(bpy^{t}Bu$_2$) (**3.1**), (ap)Ni(bpy^{t}Bu$_2$) (**3.2**), (ap)Ni(phen) (**3.3**), and (ap^{Ph})Ni(bpy^{t}Bu$_2$) (**3.4**), as 1 mM solutions in THF containing 0.1 M $[Bu_4N][PF_6]$ supporting electrolyte. Data were collected at a glassy carbon working electrode, with a platinum wire counter electrode, and a silver wire pseudo-reference electrode using a scan rate of 200 mV s^{-1}.

Table 3-2 Electrochemical Data of Complexes **3.1–3.4**. Conditions described in caption of Figure 3.7.

	$E^{\circ\prime}$ / V vs $[Cp_2Fe]^{+/0}$				
	$E^{\circ\prime}_1$ $[Ni]^{2+/1}$	$E^{\circ\prime}_2$ $[Ni]^{+/0}$	$E^{\circ\prime}_3$ $[Ni]^{0/-}$	$E^{\circ\prime}_4$ $[Ni]^{1-/2-}$	$E^{\circ\prime}_2 - E^{\circ\prime}_3$
3.1	0.13	–0.46	–2.01	–2.76	1.54
3.2	–0.07	–0.73	–2.15	–2.80	1.42
3.3	–0.04	–0.69	–2.00	–2.71	1.31
3.4	–0.07	–0.90	–2.05	–2.80	1.15

Complex **3.1**, (cat)Ni(bpy^{t}Bu$_2$), with the catecholate donor ligand, is the most difficult to oxidize with an $E^{\circ\prime}_2$ of –0.46 V vs. $[Cp_2Fe]^{+/0}$. This oxidation is only partially reversible, as the return wave is both broad and cathodically shifted. Replacing one oxygen of the catecholate with a nitrogen in **3.2**–**3.4**, results in a cathodic shift of the first oxidation $E^{\circ\prime}_2$

by 270 mV to –0.73 V, whereas the more conjugated phenanthroline backbone of **3.4** shifts $E°'_2$ even further to –0.90 V. Unlike **3.1**, the first oxidation of all three amidophenolate complexes shows good reversibility (ipc/ipa ≅ 1), possibly due to the bulky 2,6-$C_6H_3{}^iPr_2$ groups of the amidophenolate ligands providing steric protection from coordinating solvent molecules to the oxidized cation. The ground state redox potentials observed for these complexes display the general trend that the bipyridyl ligands influence the reduction potentials and the nature of the donor ligand influences the oxidation potentials. The difference between the first oxidation and reduction ($E°'_2 - E°'_3$) is a good estimate of the thermodynamic HOMO–LUMO gap. Shown in **Table 3-2**, the trend in $E°'_2 - E°'_3$ for complexes discussed in this chapter adapts with changes to the donor ligand, that is, incorporation of the amidophenolate makes the donor ligand easier to oxidize and shrinks the HOMO-LUMO gap by (up to) 400 mV.

3.2.2 Absorption Profiles

Complexes **3.1**–**3.4** are deeply colored in both the solid state and in solution, reflecting strong absorptive properties in the visible region of the electromagnetic spectrum. **Figure 3.6** shows the absorption spectra of **3.1**–**3.4** collected as solutions in THF at 298 K. The band maxima (λ_{max}), estimated excited-state energy ($E_{LL'CT}$), extinction coefficients (ε), and solvatochromic shift value (SS)[6] of each complex are summarized in **Table 3-3**. A notable feature of these complexes is the intense, low-energy absorption band that displays intensity throughout the visible (400-750 nm) and the NIR portion (750-1300 nm) of the solar spectrum. The highest energy absorption belongs to (cat)Ni(bpy^{t}Bu$_2$), with a λ_{max} of 620 nm and a weak extinction coefficient of 3600 M^{-1} cm^{-1}.

Complexes **3.2** and **3.3** showed extinction coefficients of 6200 and 8200 M^{-1} cm^{-1}, respectively. The lowest energy absorption belongs to (ap^{Ph})Ni(bpy^{t}Bu$_2$) (**3.4**) which has a band maximum of 950 nm and an extinction coefficient of 8100 M^{-1} cm^{-1}.

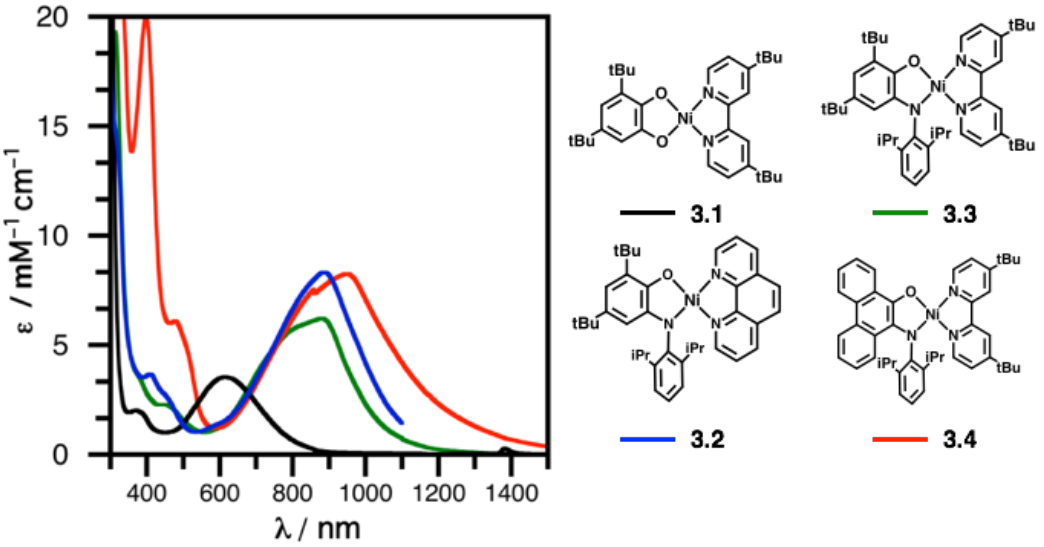

Figure 3.6 UV–vis–NIR spectra of (cat)Ni(bpy^{t}Bu$_2$) (**3.1**), (ap)Ni(bpy^{t}Bu$_2$) (**3.2**), (ap)Ni(phen) (**3.3**), and (ap^{Ph})Ni(bpy^{t}Bu$_2$) (**3.4**), in THF at 298 K.

A notable characteristic of these absorption profiles is the influence the donor ligand has on the energy of the band maxima. For example, **3.1**, **3.2**, and **3.4** all possess the same acceptor ligand and metal center yet their band maxima range from 620-970 nm (0.72 eV). Complex **3.1**, with the $(cat)^{2-}$ donor ligand shows a band maximum of 620 nm (~2 eV). When one of the oxygen donor atoms is replaced with a nitrogen as is the case with $(ap)^{2-}$ in complexes **3.2** and **3.3**, the band maxima red-shifts to 900 nm (1.34 eV).

Table 3-3 UV–vis–NIR Absorption Data of Complexes **3.1–3.4** in THF at 298 K.

Complex	λ_{max} / nm	ε / M^{-1} cm^{-1}	$E_{LL'CT}$ / eV	Solvatochromic shift
3.1	620	3600	1.52	0.45
3.2	890	6200	1.12	0.16

Complex	λ_{max} / nm	ε / M^{-1} cm^{-1}	$E_{LL'CT}$ / eV	Solvatochromic shift
3.3	900	8200	1.13	0.15
3.4	970	8100	0.95	0.19

This 0.62 eV shift in the lowest energy absorption can be attributed to perturbing the energy of the HOMO by incorporation of a less electronegative atom such as nitrogen; a concept covered in Section 3.1. Based on comparisons to the spectra of previously reported (donor)Ni^{II}(acceptor) complexes these absorptions are assigned as LL′CT transitions, owing to dominant contributions from the donor and acceptor ligands and minimal contributions from the nickel center (also see computations in Section 3.2.4). This trend in the optical LL′CT band energy is also observed in the electrochemical ground-state potentials discussed in the previous section.

3.2.3 Solvatochromic Behavior

The unsymmetrical ground state caused by the presence of two different redox-active ligands where one is electron rich and the other is electron poor should yield a dipolar ground state and exhibit negative solvatochromic response to polar solvents. **Figure 3.7a** shows the normalized absorption spectra of (cat)Ni(bpy^{t}Bu$_2$) (**3.1**) in a variety of solvents that vary in polarity. The LL′CT absorption of complex **3.1** is ~690 nm in toluene and ~520 nm in acetonitrile. As the dielectric constant of the solvent decreases, the band maxima blue shifts to lower energy, indicating a stabilization of the polar ground state. In order to quantify the solvatochromic response and determine the strength of the ground-state dipole, the solvatochromic shift number (SS) was determined for each

complex and listed in **Table 3-3.** The LL′CT excited-state energy was estimated from the low-energy onset of the absorption curve for each solvent, demonstrated in **Figure 3.7b.**

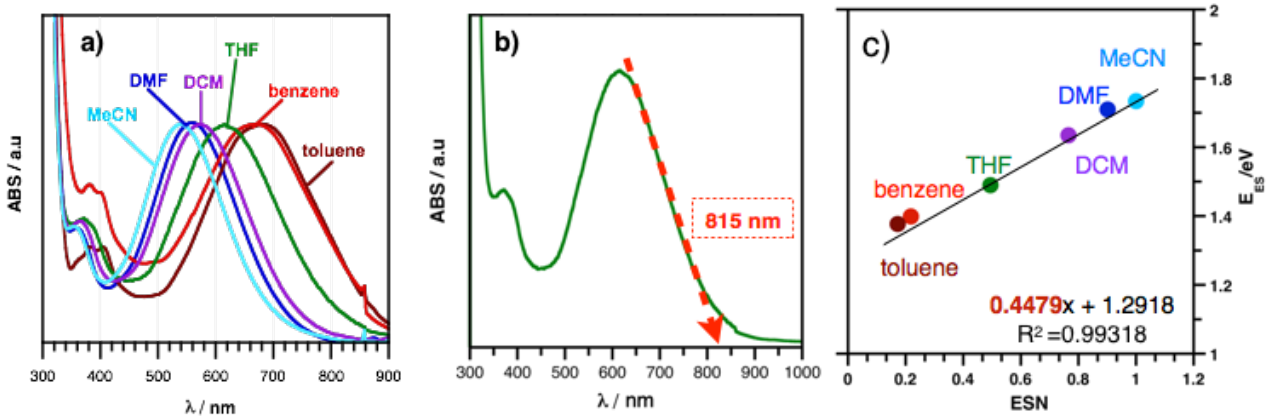

Figure 3.7 a) Normalized absorption spectra of (cat)Ni(bpy^{t}Bu$_2$) (**3.1**) in a variety of solvents, b) estimation of the onset LL′CT absorption, and c) plot of the onset LL′CT absorption versus the empirical solvent number for each solvent.

The SS number was extrapolated from the slope of the line generated by plotting the $E_{LL'CT}$ of each solvent vs. Einsenberg and Cummings' empirical solvent number (ESN)[6], **Figure 3.7c** According to the analysis, all four complexes exhibit a negative solvatochromic response with **3.1** exhibiting the largest shift of 0.41 and complexes **3.2–3.4** exhibiting similar shifts of ~0.1.

3.2.4 Computational Studies: Density Functional Theory

Density Functional Theory (DFT) computations were conducted to model the electronic properties of complexes **3.1**–**3.4**. The single-crystal structures were used as the starting point for geometry optimizations, which were initially refined at the TPSS/SVP level of theory. Subsequent structural refinements were carried out using the TZVP basis set for all atoms. The computational results were then vetted by a comparison of the

calculated optimized bond lengths with the experimental X-ray data. Agreement between the calculated and experimental data is a reliable indicator of the dependability of the computational methods (functional and basis set) and their calculated results. The computed bond lengths agreed well with the solid-state structures with the Ni–O, Ni–N, and intraligand bond distances within 0.02 Å of the solid-state data.

Table 3-4 Metal and Ligand Contributions to the HOMO and LUMO Orbitals of Complexes **3.1–3.4** as Determined by Mulliken Population Analysis.

	Percentage Contribution					Dipole moment/ Debye
	Orbital	**Ni**	**Donor**	**Acceptor**	**Energy / eV**	
3.1	LUMO	8.1	10.9	**80.9**	–2.91	10.5
	HOMO	5.8	**79.1**	15.0	–3.68	
3.2	LUMO	8.2	14.4	**77.4**	–2.82	8.9
	HOMO	7.2	**74.2**	18.6	–3.56	
3.3	LUMO	8.7	14.9	**76.4**	–2.94	7.3
	HOMO	7.0	**73.2**	19.8	–3.68	
3.4	LUMO	10.4	15.3	**74.3**	–2.78	8.9
	HOMO	8.7	**72.0**	19.2	–3.48	

Figure 3.8 shows the frontier Kohn–Sham orbital diagrams for complexes **3.1**, **3.2**, and **3.4** along with POV-Ray renderings of the HOMO and LUMO orbitals. **Table 3-4** contains the energies of these orbitals as well as the percent contribution of the metal, donor and acceptor ligands as determined by Mulliken population analysis. For all the complexes the HOMO is comprised of mostly donor ligand (72-79%) and only 6-9% metal and 15-20% acceptor ligand. The inverse is true for the LUMO orbitals where the acceptor ligand contributes the most (74-80%), the metal contributes 8-10%, and the donor contributes the least (10-15%). (cat)Ni(bpytBu2) was calculated to have the greatest ground-state dipolar moment of 10.5 Debye, in agreement with the population analysis. Complexes **3.2** and **3.4** were calculated to be less dipolar than **3.1** but still strongly dipolar

at 8.9 Debye. The smallest dipolar ground state was calculated to be complex **3.3**, at 7.39 Debye. This computational result suggests the HOMO and LUMO orbitals are mainly localized on the redox-active donor and acceptor ligand, respectfully while the Ni(II) center contributes only 6-10%, thus supporting the assignment of complexes **3.1**–**3.4** as donor-acceptor chromophores.

Kohn-Sham orbital diagrams for complexes **3.1**, **3.2**, and **3.4** show the HOMO is relatively high in energy and well isolated from other molecular orbitals. This is consistent with the electrochemical data covered in Section 3.2.1 where **3.1–3.4** are oxidized at modest potentials. Additionally, the LUMO and complex **3.1** is also well isolated from higher-energy orbitals, but interestingly, this is not the case with **3.2**–**3.4.** Unlike in **3.1,** the LUMO+1 of **3.2**–**3.4** lies close in energy to the LUMO. The LUMO+1 is predominantly dx^2–y^2 and M–L σ* in character, suggesting that there is a weaker ligand field imposed on the nickel centers in **3.2**–**3.4** than the nickel center in **3.1**. Consistent with both the spectroscopic and electrochemical data above, the calculated HOMO–LUMO gap decreases along the series **3.1** > **3.2** = **3.3** > **3.4**, though the magnitude of the decrease is smaller for the computation than for either measurement.

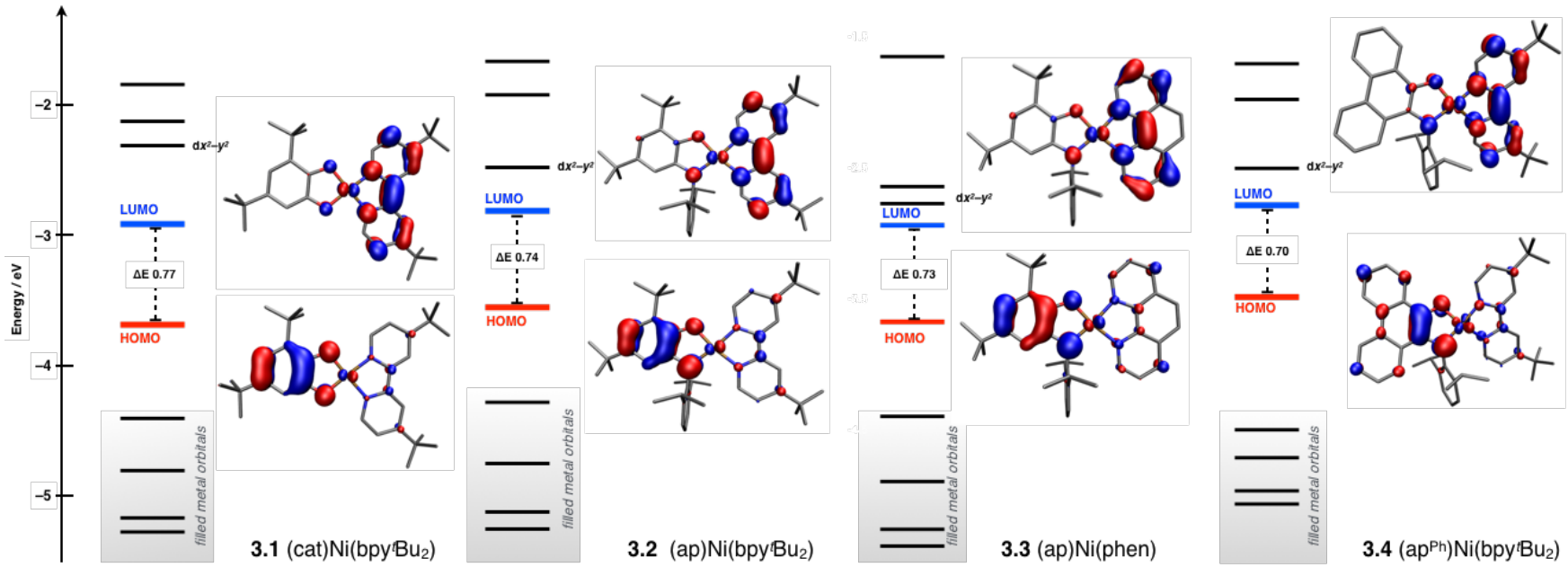

Figure 3.8 Frontier Kohn-Sham orbital diagram for (cat)Ni(bpy^{t}Bu$_2$) (**3.1**), (ap)Ni(bpy^{t}Bu$_2$) (**3.2**), (**a**p)Ni(phen) (**3.3**), **and** (ap^{Ph})Ni(bpy^{t}Bu$_2$) (**3.4**) as determined by DFT computations at the TPSS/TZVP level of theory.

3.3 Summary

By leveraging the tunable nature of LL′CT transitions, new charge-transfer chromophores have been developed with ligand localized redox events, intense absorption into the near-IR, and strong ground-state dipole moments. These complexes were constructed using a non-precious metal and readily accessible donor and acceptor ligands. The electrochemistry revealed redox potentials that are heavily dependent on the nature of the donor and acceptor ligands. The LUMO localized on the bipyridyl-type ligands, gives rise to negative reduction potentials ($E^{0/-}$). Incorporation of the strongly reducing amidophenolate donor caused a 0.35 V ± 100 mV cathodic shift in oxidation potentials when compared to the catecholate-based dye. The absorption data mirrored the trend in the electrochemistry: switching from $(cat)^{2-}$ to $(ap)^{2-}$ or $(ap^{Ph})^{2-}$ ligand destabilizes the HOMO and pushes the LL′CT absorption into the NIR (λ_{max} : 890, 900, and 970 nm, respectively). The dipole moment of the ground state was evaluated experimentally though solvatochromic measurements and computationally via DFT calculations. Each complex exhibits a negative solvatochromic shift indicative of a dipolar ground state. Complex **3.1** possesses the greatest solvatochromic shift (0.4) and greatest calculated dipole moment, 10.9 Debye. Complexes with the amidophenolate ligands shows a slightly smaller solvatochromic shifts of ~0.16 and smaller calculated dipole moments (~8.36).

The excited-state potentials of these (donor)Ni(acceptor) complexes can be estimated by relating the ground state potentials to the onset of lowest energy absorption, discussed in detail in Chapter 1. **Scheme 3-2** summarizes the estimated excited-state redox potentials for complexes **3.1**–**3.4**. According to the electro- and spectro-chemical data, the

(amidophenolate)Ni(bipyridyl) complexes (**3.2**–**3.4**) are estimated to access excited-states with potentials of $E^{+/*}(^1LL'CT)$ = –1.3 V vs. SCE and $E^{*/-}(^1LL'CT)$ = –0.5 V vs. SCE.

Scheme 3-2 Estimated excited-state redox potentials (V vs. SCE) for **3.1–3.4**.

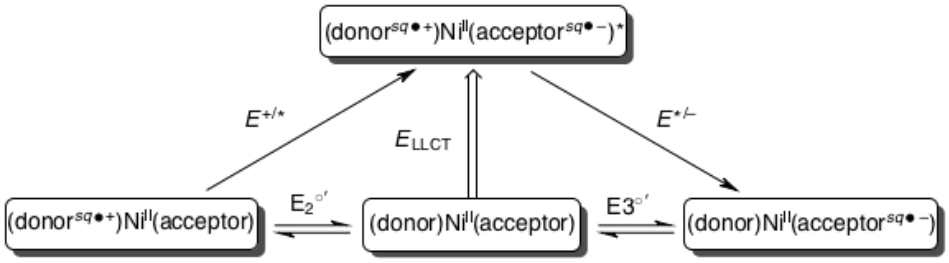

Complex	$E^{+/*}$ / V vs SCE	$E^{*/-}$ / V vs SCE
(cat)Ni(bpy^{t}Bu$_2$) (**3.1**)	–1.42	+0.07
(ap)Ni(bpy^{t}Bu$_2$) (**3.2**)	–1.29	–0.47
(ap)Ni(phen) (**3.3**)	–1.26	–0.31
(ap^{Ph})Ni(bpy^{t}Bu$_2$) (**3.4**)	–1.29	–0.54

The (cat)Ni(bpy^{t}Bu$_2$) dye is estimated to access excited-state potentials of $E^{+/*}$ ($^1LL'CT$) = –1.42 V vs. SCE and $E^{*/-}(^1LL'CT)$ = +0.07 V vs. SCE. The strength of these excited states potentials can be understood by comparing them to the quintessential MLCT photosensitizer, $[Ru(bpy)_3]^{2+}$, which is a potent excited state reductant with $E^{+/*}(^1MLCT)$ = –1.2 V vs. SCE upon absorption of a 2.5 eV photon (500 nm).[19,20] All dyes discussed in this chapter are estimated to be as strong, and in some cases, stronger excited-state reductant than $[Ru(bpy)_3]^{2+}$. The ability of these D-A LL′CT dyes to access high electron injection potentials at the expense of NIR light suggest that first row transition metals may be viable alternative to precious metals in solar energy conversion strategies. Charge-transfer complexes with properties like **3.1**–**3.4** are ideal candidates for incorporation into dye-sensitized solar cells (DSSCs), where binding of the dye to the TiO_2 surface provides an

intramolecular pathway for fast charge injection. In DSSCs incorporating $[Ru(bpy)_3]^{2+}$-type dyes, charge injection from the bpy π* orbital into the conduction band of TiO_2 occurs on the sub-picosecond timescale.[21,22] Given that **3.1**–**3.4** use the same bipyridyl π* acceptor orbital, similarly rapid charge-injection rates should be possible for these dyes. To further develop this family of dyes, derivatives must be prepared that incorporate carboxylate linkers capable of binding to nanocrystalline TiO_2, a topic covered in Chapter 4.

3.4 Experimental

General Considerations. All compounds and reactions reported below show various levels of air- and moisture-sensitivity, so all manipulations were carried out using standard vacuum-line, Schlenk-line and glovebox techniques. Solvents were sparged with argon before being deoxygenated and dried by passage through Q5 and activated alumina columns, respectively. To test for effective oxygen and water removal, aliquots of each solvent were treated with a few drops of a purple solution of sodium benzophenone ketyl radical in THF. The reagents $Ni(cod)_2$ (Strem), 3,5-di-*tert*-butyl-1,2-quinone (Aldrich), and 4,4'-di-*tert*-butyl-2,2'-bipyridine (Aldrich) were reagent grade or better and used as received. The iminoquinones, 3,5-di-tert-butyl(2,6-diisopropylphenyl)-*ortho*-iminoquinone and 9,10-(2,6-diisopropylphenyl)iminophenanthrenquinone were prepared according to literature procedures.[27,28] Elemental analyses were performed on a PerkinElmer series II 2400 CHNS analyzer.

Spectroscopic Measurements. NMR spectra were collected at 298 K on a BrukerAvance 400 MHz or 500 MHz spectrometer in dry, degassed C_6D_6 or $CDCl_3$. ^1H and ^{13}C NMR spectra were referenced to tetramethylsilane (TMS) using the residual ^1H and ^{13}C

impurities of the deuterated solvent.[29] All chemical shifts are reported using the standard δ notation in parts per million; positive chemical shifts are to a higher frequency of TMS. Electronic absorption spectra were recorded with a PerkinElmer Lamda 900 UV-vis-NIR Spectrometer using one-centimeter path-length cells at ambient temperature (20-24 °C).

Electrochemical Methods. Electrochemical experiments were recorded on a Gamry Series G300 potentiostat/galvanostat/ZRA (Gamry Instruments, Warminster, PA) using a 3.0 mm glassy carbon working electrode, a platinum wire auxiliary electrode, and a silver wire pseudo-reference electrode. Reversibility of a redox process was judged based on the ratio of the anodic to the cathodic current being close to unity ($i_{pa}/i_{pc} \cong 1$) for a given process. Electrochemical experiments were performed at ambient temperature (20-24 °C) in a nitrogen-filled glovebox using THF solutions containing 1 mM analyte and 100 mM $[NBu_4][PF_6]$ as the supporting electrolyte. All potentials are referenced to $[Cp_2Fe]^{+/0}$ using ferrocene or decamethylferrocene (−0.49 V vs $[Cp_2Fe]^{+/0}$)[30] as internal standards. Ferrocene and decamethylferrocene (Acros) were purified by sublimation under reduced pressure and tetrabutylammonium hexafluorophosphate (Acros) was recrystallized from ethanol three times and dried under vacuum.

X-ray Data Collection and Reduction. X-ray diffraction data for all complexes were collected on single crystals mounted on either a glass fiber or a cryoloop and coated with oil. Data were acquired using a Bruker SMART APEX II diffractometer at 143 K using Mo Kα radiation (λ = 0.71073 Å). The APEX2[31] program package was used to determine unit-cell parameters and for data collection. The raw frame data were processed using SAINT[32] and SADABS[33] to yield the reflection data file. Subsequent refinement cycles were carried out using the SHELXTL program suite.[34] Analytical scattering factors for neutral atoms were

used throughout the analyses.[35] ORTEP diagrams were generated using ORTEP-3 for Windows.[36] Diffraction data for **3.1**–**3.4** are given in the **Table 3-5**.

Density Functional Theory Computations. Calculations were performed in the Molecular Modeling Facility in the Department of Chemistry at UC Irvine. Calculations were performed employing Meta-GGA functional TPSS.[37] Geometry optimizations were initiated using a split-valence plus polarization basis set (def2-SVP)[38] and further refined using the polarized triple-ζ basis set def2-TZVP.[39] Structures obtained from single-crystal X-ray diffraction experiments were used as the starting points for geometry optimizations; no molecular symmetry was imposed. For complexes **3.1**, **3.3**, and **3.4**, molecular geometries and orbital energies were evaluated self-consistently to tight convergence criteria (energy converged to 0.1 μHartree, maximum norm of the Cartesian gradient ≤ 10−4 a.u.). For complex **3.2**, ultra tight convergence criteria (0.01 μHartree, maximum norm of the Cartesian gradient ≤ 10−6 a.u.) yielded a single imaginary frequency (–6 cm^{-1}) that was identified as numerical noise upon vibrational analysis. Mulliken population analyses were obtained at TPSS/TZVP theory level; the contour values were 0.03 for the molecular orbital plots. All calculations were performed using the quantum chemistry program package TURBOMOLE.[40,41]

General Iminoquinone Synthesis. 2,4-di-*tert*-butyl-2,6-diisopropylphenyl-iminoquinone (iq) and 2,6-diisopropylphenyl-imino-phenanthrenquinone (iq^{ph}) were prepared according to literature procedures.[27,28]

Synthesis of (cat)Ni(bpy^{t}Bu$_2$) (3.1). A benzene solution of a $Ni(cod)_2$ (140 mg, 0.50 mmol, 1.0 equiv) and 3,5-bis(*tert*-butyl)-1,2-benzoquinone (110 mg, 0.50 mmol, 1.0 equiv) was stirred at ambient glovebox temperature for one hour. Solid 4,4'-di-*tert*-butyl-

2,2'-bipyridine (130 mg, 0.50 mmol, 1.0 equiv) was then added to the solution and stirring was continued for 2 days. The volume of the resulting dark blue solution was reduced to ¼ and 10 ml of pentane was added to yield the product as a deep blue crystalline solid in 80% yield (220 mg). X-ray quality crystals were grown by vapor diffusion of diethyl ether into a solution of **3.1** in benzene. ^{1}H NMR (400 MHz, $CDCl_3$) δ/ppm: 1.26 (*s*, 9H), 1.40 (*s*, 18H), 1.47 (*s*, 9H), 6.34 (*d*, J = 2.1 Hz, 1H), 6.55 (*d*, J = 2.2 Hz, 1H), 7.36 (*m*, 1H), 7.47 (*d*, J= 5.7 Hz, 1H), 7.48, 7.65 (*s*, 2H), 8.63 (*d*, J = 5.7 Hz, 1H), 8.71 (*d*, J = 5.7 Hz, 1H). ^{13}C NMR (126 MHz, $CDCl_3$,) δ/ppm: 163.3 (*C*=N), 160.9 (*C*–O), 160.7 (*C*–O), 156.9 (aryl–*C*), 153.1 (aryl–*C*), 149.7 (aryl–*C*), 149.5 (aryl–*C*), 136.6 (aryl–*C*H), 133.0 (aryl–*C*H), 123.0 (aryl–*C*H), 122.6 (aryl–*C*H), 120.6 (aryl–*C*H), 118.2 (aryl–*C*H), 116.6 (aryl–*C*H), 109.5 (aryl–*C*H), 109.2 (aryl–*C*H), 35.5 (*C*–$(CH_3)_3$) , 34.2 (*C*–$(CH_3)_3$), 33.9 (*C*–$(CH_3)_3$), 32.1 ((–*C*$H_3)_3$), 30.6 ((–*C*$H_3)_3$), 30.3 ((–*C*$H_3)_3$). Anal. Calcd. for $C_{32}H_{44}N_2O_2Ni$: C, 70.21; H, 8.10; N 5.12. Found: C, 70.09; H, 8.15; N, 5.05 %. UV-vis-NIR (THF) λ_{max}/nm (ε/M^{-1} cm^{-1}): 370 (2000), 620 (3600).

Synthesis of (ap)Ni(bpytBu2) (3.2). A benzene solution of a $Ni(cod)_2$ (140 mg, 0.50 mmol, 1.0 equiv) and 3,5-di-tert-butyl(2,6-diisopropylphenyl)-ortho-iminoquinone (190 mg, 0.50 mmol, 1.0 equiv) was stirred at ambient glovebox temperature for one hour. Solid 4,4'-di-*tert*-butyl-2,2'-bipyridine (130 mg, 0.50 mmol, 1.0 equiv) was then added to the solution and stirring was continued for 2 days. The solvent was stripped from the resulting dark yellow-green solution and the solid residue was dissolved in toluene, diluted with pentane, and chilled to −35 °C. The precipitated solid was collected by filtration, washed with cold pentane, and dried under reduced pressure to obtain the desired product as a black crystalline solid in 66% yield (220 mg). X-ray quality crystals were obtained from concentrated solution of **3.2** in benzene. ^{1}H NMR (500 MHz, C_6D_6) δ/ppm: 0.72 (br *s*,

9H), 0.91 (br *s*, 9H), 1.26 (*d*, J = 6.9 Hz, 6H), 1.30 (*d*, J = 6.9 Hz, 6H), 1.51 (*s*, 9H), 2.01 (*s*, 9H), 4.59 (*m*, 2H), 6.27 (*d*, J = 2.1 Hz, 1H), 6.59 (*s*, 1H,), 6.88 (br s, 2H), 6.95 (*d*, J = 2.1 Hz, 1H), 7.14 (*d*, J = 1.6 Hz, 2H), 7.42 (*d*, J = 6.7, 2H), 7.48 (*m*, 1H), 9.79 (*s*, 1H). ^{13}C NMR (101 MHz, C6D6,) δ/ppm: 160.9 (N=*C*), 160.7 (aryl–*C*), 155.9 (*C*–O), 155.1 (*C*–N), 154.2 (aryl–*C*), 152.1 (aryl–*C*), 150.1 (br, N–*C*H), 149.9 (aryl–*C*(ipp), 147.7 (aryl–*C*), 137.2 (aryl–*C*), 131.5 (aryl–*C*), 128.4 (aryl–*C*H, 125.8 (diip aryl–*C*H), 125.1 (diip aryl–*C*H), 123.5 (aryl–*C*), 123.4 (aryl–*C*), 122.2 (aryl–*C*), 121.4 (aryl–*C*), 116.6 (aryl–*C*), 116.1 (aryl–*C*), 109.2 (aryl–*C*H), 108.5 (aryl–*C*H), 35.1 (ap–*C*(CH_3)3), 34.7 (*C*(CH_3)$_3$), 32.8 (C(*C*H_3)$_3$), 31.0 (C(*C*H_3)$_3$), 29.9 (br, C(*C*H_3)$_3$), 29.6 (br, C(*C*H_3)$_3$), 28.2 (*C*H(CH_3)$_2$), 24.9 (CH(*C*H_3)$_2$), 24.4 (CH(*C*H_3)$_2$). Anal. Calcd. for $C_{44}H_{61}N_3ONi$: C, 74.78; H, 8.70; N, 5.95. Found: C, 74.52; H, 8.60; N, 5.41%. UV-vis-NIR (THF) λ_{max}/nm (ε/M^{-1} cm^{-1})]: 310 (19600), 890 (6200).

Synthesis of (ap)Ni(phen) (3.3). Complex **3.3** was prepared by treatment of a Ni(cod)$_2$ (140 mg, 0.50 mmol, 1 equiv) THF solution with one equivalent of 1,10-phenanthroline (90 mg, 0.50 mmol, 1 equiv) to generate a dark green solution. After 20 minutes of stirring, the putative (cod)Ni(phen) intermediate was then treated with a chilled solution of iq (190 mg, 0.50 mmol, 1 equiv) and stirred for 2 days. The volume of the resulting dark green solution was reduced, pentane was added, and cooled to –35 ºC. The solid was collected over a frit and washed with cold pentane to yield 3 as a deep evergreen microcrystalline solid. (230 mg, 73% yield). (500 MHz, C_6D_6) δ/ppm: δ/ppm 1.16 (*d*, J= 6.5 Hz, 6H), 1.22 (*d*, J= 6.3 Hz, 6H), 1.51 (9H,), 1.98 (*s*, 9H), 4.53 (*m*, J= 6.1, 2H), 6.31 (*s*, 1H), 6.42 (*s*, 1H), 6.69 (*s*, 1H), 6.78 (*s*, 2H), 6.97 (*m*, 2H), 7.00 (*s*, 1H), 7.07 (*s*, 1H), 7.38 (*d*, J= 7.3, 2H), 7.44 (*t*, J= 7.6, 1H), 9.76 (*s*, 1H). ^{13}C NMR (126 MHz, C_6D_6,) δ/ppm: 163.3 (*C*=N), 160.9 (*C*–O), 160.7 (*C*–O), 156.9 (aryl–*C*), 153.1 (aryl–*C*), 149.7 (aryl–*C*), 149.5 (aryl–*C*), 136.6

(aryl–*C*H), 133.0 (aryl–*C*H), 123.0 (aryl–*C*H), 122.6 (aryl–*C*H), 120.6 (aryl–*C*H), 118.2 (aryl–*C*H), 116.6 (aryl–*C*H), 109.5 (aryl–*C*H), 109.2 (aryl–*C*H), 35.5 (*C*–$(CH_3)_3$) , 34.2 (*C*–$(CH_3)_3$), 33.9 (*C*–$(CH_3)_3$), 32.1 ((–*C*$H_3)_3$), 30.6 ((–*C*$H_3)_3$), 30.3 ((–*C*$H_3)_3$). Anal. Calcd. for $C_{38}H_{45}N_3ONi$: C, 73.80; H, 7.33; N, 6.79. Found: C, 73.52; H, 7.74; N 6.77 %. UV-vis-NIR (THF) λ_{max}/nm (ε/M^{-1} cm^{-1}): 410 (3700), 890 (8400).

Synthesis of (ap^{ph})Ni(bpy^{t}Bu$_2$) (3.4). The complex (ap^{ph})Ni(bpy^{t}Bu$_2$) was prepared by the same method used to prepare **3.2**, using 134 mg of Ni(cod)$_2$ (0.5 mmol, 1 equiv), 134 mg of 4,4'-di-*tert*-butyl-2,2'-bipyridine (134 mg, 0.5 mmol), and 180 mg of 9,10-(2,6-diisopropylphenyl)iminophenanthrenquinone (0.5 mmol, 1 equiv). The product was isolated as black crystals in 81% yield (260 mg). X-ray quality crystals were grown by vapor diffusion of diethyl ether into a solution of **3.4** dissolved in benzene. ^{1}H NMR 500 MHz (C_6D_6) δ/ppm: 0.86 (*s*, 18H), 1.14 (*d*, J = 6.9 Hz, 6H) 1.31 (*d*, J = 6.9 Hz 6H,) 4.76 (*m*, 2H), 6.59 (*d*, J = 5.4 Hz, 2H,), 7.12 (*d*, J = 1.6 Hz, 2H), 7.18 (*m*, 2H,), 7.25 (*t*, J = 7.4 Hz, 1H), 7.37 (*d*, J = 7.7 Hz, 2H), 7.47 (*t*, J = 7.5 Hz, 1H), 7.55 (*t*, J = 7.6 Hz, 1H), 7.63 (*d*, J = 8.6 Hz, 1H), 7.83 (*t*, J = 7.4 Hz, 1H), 8.73 (*d*, J = 8.3 Hz, 1H), 8.79 (*d*, J = 8.2 Hz, 1H,), 9.16 (*d*, J = 8.1 Hz, 1H). ^{13}C NMR (126 MHz; C_6D_6) δ/ppm: 160.5 (N=*C*), 152.3 (*C*–O), 149.6 (aryl–*C*), 147.8 (aryl–*C*), 141.1 (aryl–*C*), 129.22 (aryl–*C*), 129.0 (aryl–*C*), 128.5 (aryl–*C*), 126.5 (aryl–*C*), 125.6 (aryl–*C*H), 125.2 (aryl–*C*H), 124.4 (aryl–*C*H), 124.1 (aryl–*C*H), 123.5 (aryl–*C*H), 123.4 (aryl–*C*H), 122.7 (aryl–*C*H), 121.1 (aryl–*C*H), 121.0 (aryl–*C*H), 120.6 (aryl–*C*H), 116.2 (aryl–*C*H), 30.5 (–C(*C*$H_3)_3$), 29.8 (–C$(CH_3)_3$), 28.6 (*C*H$(CH_3)_2$), 23.9 (CH(*C*$H_3)_2$), 23.8 (CH(*C*$H_3)_2$). Anal. calcd for $C_{44}H_{49}N_3ONi \bullet C_6H_6$: C, 77.72; H, 7.17; N, 5.44. Found: C, 77.43; H, 7.09; N, 5.24%. UV-vis-NIR (THF) λmax/nm (ε/M^{-1} cm^{-}1): 400 (18000), 955 (8100).

3.6 References

(1) McConnell, I.; Li, G.; Brudvig, G. W. *Chemistry & Biology* **2010**, *17* (5), 434–447.
(2) Kiang, N. Y.; Siefert, J.; Govindjee; Blankenship, R. E. *Astrobiology* **2007**, *7* (1), 222–251.
(3) Hanna, M. C.; Nozik, A. J. *J. Appl. Phys.* **2006**, *100* (7), 074510.
(4) Cook, T. R.; Dogutan, D. K.; Reece, S. Y.; Surendranath, Y.; Teets, T. S.; Nocera, D. G. *Chem. Rev.* 2010, 10, 6474-6502
(5) Ardo, S.; Meyer, G. J. *Chem. Soc. Rev.* **2008**, *38* (1), 115.
(6) Cummings, S. D.; Eisenberg, R. *J. Am. Chem. Soc.* **1996**, *118* (8), 1949–1960.
(7) O'Regan, B.; Grätzel, M. *Nature* **1991**, *353* (6346), 737–740.
(8) Paw, W.; and, W. P.; Eisenberg, R. *Inorg. Chem.* **1997**, *36* (11), 2287–2293.
(9) Han, Z.; Eisenberg, R. *Acc. Chem. Res.* **2014**, *47* (8), 2537–2544.
(10) Sik Min, K.; Weyhermüller, T.; Wieghardt, K. *Dalton Trans.* **2003**, No. 6, 1126–1132.
(11) Blackmore, K. J.; Sly, M. B.; Haneline, M. R.; Ziller, J. W.; Heyduk, A. F. *Inorganic Chemistry* **2008**, *47* (22), 10522–10532.
(12) Poddel'sky, A. I.; Cherkasov, V. K.; Abakumov, G. A. *Coord. Chem. Rev.* **2009**, *253* (3-4), 291–324.
(13) Brown, S. N. *Inorg. Chem.* **2012**, *51* (3), 1251–1260.
(14) Gorelsky, S. I.; Dodsworth, E. S.; Lever, A.; Vlcek, A. A. *Coord. Chem. Rev.* **1998,** 174, 469-494.
(15) Kramer, W. W.; Cameron, L. A.; Zarkesh, R. A.; Ziller, J. W.; Heyduk, A. F. *Inorg. Chem.* **2014**, 140806135722006.
(16) Biner, M.; Buergi, H. B.; Ludi, A.; Roehr, C. *J. Am. Chem. Soc.* **1992**, *114* (13), 5197–5203.
(17) Nishigaki, S.; Yoshioka, H.; Nakatsu, K. *Acta Crystallogr B Struct Crystallogr Cryst Chem* **1978**, *34* (3), 875–879.
(18) Chaudhuri, P.; Verani, C. N.; Bill, E.; Bothe, E.; Weyhermüller, T.; Wieghardt, K. *J. Am. Chem. Soc.* **2001**, *123* (10), 2213–2223.
(19) Juris, A.; Campagna, S.; Balzani, V.; Gremaud, G.; Zelewsky, Von, A. *Inorg. Chem.* **1988**, *27* (20), 3652–3655.
(20) Vlcek, A. A.; Dodsworth, E. S.; Pietro, W. J.; Lever, A. B. P. *Inorg. Chem.* **1995**, *34* (7), 1906–1913.
(21) McCusker, J. K. *Science* **2001**, *293* (5535), 1599–1601.
(22) Vlček, A., Jr. *Coord. Chem. Rev.* **2000**, *200-202*, 933–978.
(23) Gonçalves, L. M.; de Zea Bermudez, V.; Ribeiro, H. A.; Mendes, A. M. *Energy Environ. Sci.* **2008**, *1* (6), 655.
(24) Swierk, J. R.; Mallouk, T. E. *Chem. Soc. Rev.* **2013**, *42*, 2357–2387.
(25) Bozic-Weber, B.; Constable, E. C.; Housecroft, C. E. *Coord. Chem. Rev.* **2013**, *257* (21-22), 3089–3106.
(26) Grätzel, M. *Nature* **2001**, *414* (6861), 338–344.
(27) Abakumov, G. A. *Russ. Chem. Bull*. **2003**, 52, 712.
(28) Abakumov, G. A.; Cherkasov, V. K.; Druzhkov, N. O.; Kurskii, Y. A.; Fukin, G. K. Abakumova, L. G.; Kocherova, T. N. *Synth. Comm*. **2006**, 36, 3241.
(29) Gottlieb, H.; Kotlyar, V.; Nudelman, A. *J. Org. Chem.* **1999**, 62, 7512.

(30) N. G. Connelly, and W. E. Geiger, *Chem. Rev.*, **1996**, 96, 877.
(31) APEX2 Version 2013.6-2, Bruker AXS, Inc.; Madison, WI 2013.
(32) SAINT Version 8.32b, Bruker AXS, Inc.; Madison, WI 2012.
(33) Sheldrick, G. M. SADABS, Version 2012/1, Bruker AXS, Inc.; Madison, WI 2012.
(34) Sheldrick, G. M. SHELXTL, Version 2014/7, Bruker AXS, Inc.; Madison, WI 2014.
(35) International Tables for Crystallography, A. J. C. Wilson, Ed.; Kluwer Academic, Dordrecht, Netherlands, 1992, Vol. C.
(36) Farrugia,L. J. *J. Appl. Crystallogr*. **1997**, 30, 565.
(37) Tao, J.; Perdew, J. P.; Staroverov, V. N.; Scuseria G. E. *Phys. Rev. Lett*. **2003**, 91 146401.
(38) Schäfer, A.; Horn H.; Ahlrichs, R. *J. Chem. Phys.* **1992**, 97, 2571.
(39) Schäfer, A.; Huber, C.; Ahlrichs, R. *J. Chem. Phys. 1994*, 100, 5829.
(40) TURBOMOLE V6.3, Turbomole GmbH, Karlsruhe, 2011. http://www.turbomole.com.
(41) F. Furche, F.; Alrichs, R.; Hättig, C.; Klopper, W.; Sierka, M.; Weigend, F.; *WIREs Comp. Mol. Chem.* **2014**, 4, 91.

Chapter 4

Experimental and Computational Studies of Square-Planar (donor)Ni^{II}(acceptor) LL′CT Dyes Equipped With Carboxyl -Anchoring Groups

4.1 Introduction

Titanium dioxide (TiO_2) remains one of the most widely used metal oxides in photocatalytic and photovoltaic systems owing to its photo(electro)chemical stability, high energy conduction band, ease of availability, and low cost.[1,2] Once an electron is photo-excited into the conduction band, it possesses enough potential energy to generate an electrical current in photovoltaic systems (dye sensitized solar cells, DSSCs), or fuel a catalyst for artificial photosynthetic reactions.[3-7] The major drawback of TiO_2 is the lack of spectral response in the visible and NIR regions of the solar spectrum, making it inert to visible light excitation. Therefore, the surface of TiO_2 is commonly sensitized by molecular dyes, that when are excited by a visible photon access excited-state oxidation potentials potent enough to inject into the conduction band of TiO_2.

The most frequently employed photosensitizers have been the ruthenium polypyridyl family of dyes. When the acceptor ligands are functionalized with carboxyl anchoring groups and adsorb onto the metal oxide surface, charge-injection into the conduction band of TiO_2 takes place on a femtosecond time-scale.[8,9] Square-planar dyes have also been studied by Eisenberg and coworkers, where they employed (dithiolate)Pt^{II}(bipyridyl) complexes in photochemical hydrogen evolution (photo-HER) applications.[10-12] The development of less-costly alternatives to these noble-metal sensitizers is particularly important regarding the realization of sustainable, renewable energy. Earth-abundant charge-transfer chromophores can be equipped with carboxyl-anchoring groups for sensitization of large band-gap semiconductors. The LL′CT chromophores discussed in Chapter 3 are promising candidates as NIR light harvesters for TiO_2 sensitization because of their potent excited-state oxidation potentials. In this chapter,

two (donor)Ni^{II}(bipyridine) LL′CT chromophores are functionalized with anchoring groups capable of tethering to metal oxide surfaces. The thermodynamic characteristics of dyes with the general formula: (donor)Ni^{II}(bpy^{COOMe}) where donor = 3,5-di-*tert*-butyl-catecholate, $(cat)^{2-}$; and 2,4-di-*tert*-butyl-6-((2,6-diisopropylphenyl)amidophenolate, $(ap)^{2}$, and bpy^{COOMe} = dimethyl [2,2'-bipyridine]-4,4'-dicarboxylate are investigated spectroscopically, electrochemically, and computationally. The potential of the LL′CT dyes to be sensitizers for photovoltaic solar cells is investigated through preliminary binding studies onto metal oxide surfaces.

4.2 Results and Discussion

4.2.1 Synthesis and Characterization

4,4'-*di*-methyl-bipyridine (bpy^{Me}) was functionalized with two carboxyl anchoring groups at the 4 and 4′ positions via oxidation by $Cr(VI)O_3$ to yield, [2,2′-bipyridine]-4,4′-dicarboxylic acid (bpy^{COOH}). Due to the poor solubility of the bpy^{COOH} ligand, the carboxy-functional groups were methylated to yield to more soluble ester-protected derivative, *di*-methyl [2,2′-bipyridine]-4,4′-dicarboxylate (bpy^{COOMe}) in excellent yield (90%).

Square-planar Ni(II) donor-acceptor LL′CT chromophores equipped with carboxyl anchoring groups for tethering to metal oxide surfaces were achieved through treatment of a Ni(0) synthon, $Ni(cod)_2$ with the functionalized acceptor, dimethyl [2,2′-bipyridine]-4,4′-dicarboxylate. The reaction was stirred for 12 hours as outlined in **Scheme 4.** Metallation to the Ni(0) center was indicated by a drastic color change from yellow to dark purple. Subsequent addition of the $donor^{quinone}$ resulted in a two electron oxidation of the Ni(0) intermediate to Ni(II) and the reduction of $donor^{quinone}$ to $[donor^{cat}]^{2-}$; a two-electron redox

reaction indicated by an obvious color change from purple to dark blue (**4.1**) or green (**4.2**). The desired square-planar complexes, (cat)Ni(bpy^{COOMe}) (**4.1**) and (ap)Ni(bpy^{COOMe}) (**4.2**) were isolated in good yields and purity (76% and 90%).

Scheme 4-1 Synthetic procedure and donor and acceptor ligands used in this chapter.

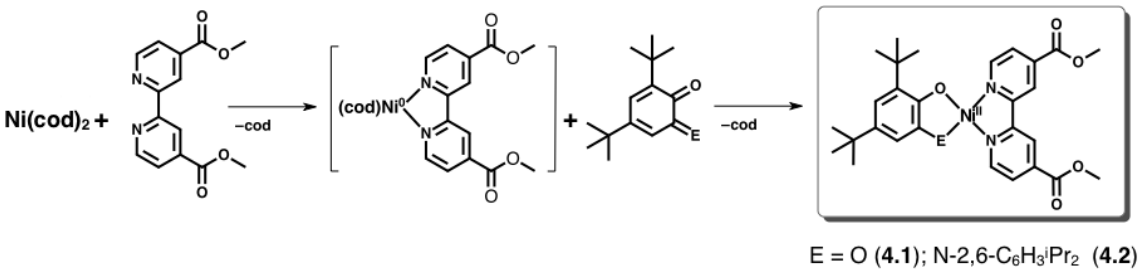

The square-planar D-A LL′CT Ni(II) dyes are diamagnetic and are confirmed unequivocally via ^{1}H NMR spectroscopy. The ^{1}H NMR spectrum of (cat)Ni(bpy^{COOMe}) (**4.1**) displayed a sharp singlet for the methoxy proton resonances of the bpy^{COOMe} ligand where there should be two, considering the unsymmetrical nature of 3,5-di-*tert*-butyl-1,2-catecholate. A high field NMR spectrometer did not resolve this resonance however, the Cs symmetry is apparent in the aromatic region. Between 8.86 and 7.19 ppm there are six singlet resonances corresponding to the chemically distinct aromatic protons on the bpy^{COOMe} ligand. The ^{1}H NMR of (ap)Ni(bpy^{COOMe}) (**4.2**) shows sharp and well resolved resonances for the aromatic protons of the donor (ap)$^{2-}$ ligand. The isopropyl groups give rise to a septet near 4.23 ppm for the methine proton and a pair of doublets near 1.7 and 1.4 ppm for the chemically different methyl protons, consistent with the Cs symmetry and the square-planar geometry indicated in the single-crystal X-ray structure. Similar to **4.1**, the methyl resonances of the bpy^{COOMe} ligand in **4.2** appear as a singlet at 3.34 ppm for (ap)Ni(bpy^{COOMe}) (**4.2**).

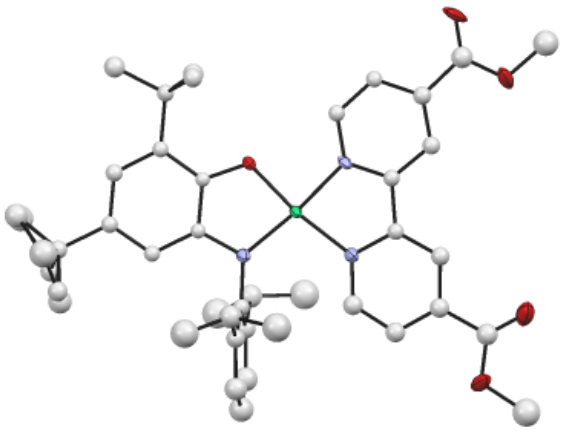

Figure 4.1 ORTEP Diagram of **4.2.** Thermal ellipsoids are shown at 50% probability. Hydrogen atoms and non-coordinated solvent molecules are omitted for clarity.

Table 4-1 Selected Bond Distances for **4.2** and MOS assignment.

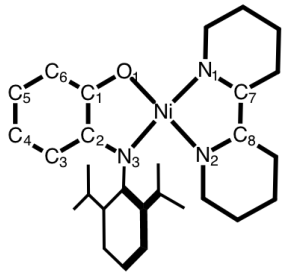

Bond Distances / Å	
Ni-O(1)	1.831
Ni–N(3)	1.862
Ni–N(1)	1.895
Ni–N(2)	1.926
N(3)–C(2)	1.396
C(1)–C(2)	1.404
C(2)–C(3)	1.399
C(3)–C(4)	1.400
C(4)–C(5)	1.410
C(5)–C(6)	1.411
C(1)–C(6)	1.409
N(2)–C(8)	1.363
N1–C7	1.347
C7–C8	1.457
MOS	**–1.77**

Single crystals of (ap)Ni(bpy^{COOMe}) were obtained by vapor diffusion of pentane into a solution of **4.2** in THF. The ORTEP diagram of **4.2** is shown in **Figure 4.1** and relevant bond lengths are listed in **Table 4-1**. Examination of the crystal structure reveals the Ni(II)

center is in a pseudo square-planar coordination environment with the bond angle between the two chelating nitrogen atoms of the acceptor ligand and the metal center N(1)–Ni–N(2) measuring 82.9°. The 4,4'-ester-functionalized bipyridine ligand is close to planar, with a dihedral angle of 11.43°, between the two pyridine rings. The bpy^{COOMe} ligand shows bridgehead C–C bond distance of 1.457 Å and C–N distances of 1.347 and 1.363 Å, consistent with neutral bipyridyl-type ligands.[15]

For the donor ligand, the bond angle between the two chelating oxygen and nitrogen atoms and the metal center N(1)–Ni–N(2) measures 85.8°. The C(1)–O(1) distance of the amidophenolate ligand measures 1.336 Å and is longer than observed distances of carbon-oxygen double bonds, 1.23 Å.[15] The C(2)–N(3) distance of the $(ap)^{2-}$ ligand measures 1.34 Å and is also longer than the 1.27 Å observed for the C=N bond in neutral quinone ligands and is consistent with carbon–nitrogen single bonds observed in dianionic amidophenolate ligands. The metrical oxidation state assignment for the donor ligand in **4.2** is –1.77, which corresponds to the dianionic, amidophenolate oxidation state.[16] The available structural data are consistent with a fully reduced donor and neutral acceptor

4.2.2 Electrochemistry

Cyclic voltammetry studies of all complexes were conducted in MeCN and THF solutions containing 0.10 M $[Bu_4N][PF_6]$ as the supporting electrolyte at a glassy carbon-working electrode. The results of the electrochemical experiments are summarized in **Table 4-2** (note: the potentials recorded in THF for **4.1** and **4.2** are in parenthesis). **Figure 4.2** shows the cyclic voltammograms of (cat)Ni(bpy^{COOMe}) and (ap)Ni(bpy^{COOMe}) taken in MeCN. The electrochemical behavior of the functionalized dyes shows two, one-electron

reduction events. The first, $E^{\circ\prime}_3$, corresponds to the reduction of the neutral bpy^{COOMe} to the monoanionic semiquinone (bpy$^{COOMe\bullet}$)$^{-}$; and the second, $E^{\circ\prime}_4$, corresponds to the reduction of (bpy$^{COOMe\bullet}$)$^{-}$ to the dianionic (bpy^{COOMe})$^{2-}$. The reduction event ($E^{\circ\prime}_3$) for **4.1** and **4.2** exhibit full reversibility (ipc/ipa ≅ 1) in MeCN and falls at –1.44 and –1.38 V vs. $[Cp_2Fe]^{+/0}$, for **4.1** and **4.2**, respectively. Considering the potentials recorded in THF (**Table 4-2**, values in parenthesis), we can make a direct comparison to the potentials of the same events of the non-functionalized dyes, **3.1** and **3.2** (introduced in Chapter 3). The values for the functionalized dyes are considerably less negative when compared to the non-functionalized derivatives in the same solvent. For example, $E^{\circ\prime}_3$ for (ap)Ni(bpy^{t}Bu$_2$) (**3.2**) is –2.15 V and when the acceptor ligand is functionalized with the ester-anchoring group (as is the case with **4.2**), $E^{\circ\prime}_3$ shifts anodically by 0.77 V to –1.58 V in THF. Likewise, the second reduction event, $E^{\circ\prime}_4$, shifts +0.61 V compared to the non-functionalized dye.

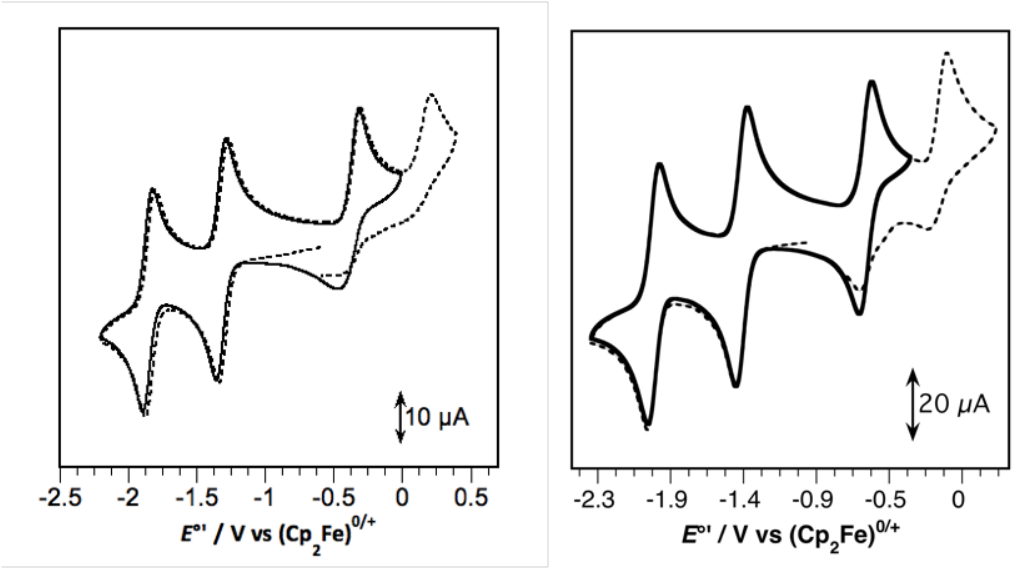

Figure 4.2 Cyclic voltammograms of (cat)Ni(bpy^{COOMe}), **4.1** (left) and (ap)Ni(bpy^{COOMe}), **4.2** (right) as 1 mM solutions in MeCN containing 0.1 M $[Bu_4N][PF_6]$ supporting electrolyte. Data were collected at a glassy carbon working electrode, with a platinum wire counter electrode, and a silver wire pseudo-reference electrode using a scan rate of 200 mV s^{-1}.

Table 4-2 Electrochemical Potentials of Complexes **4.1, 4.2**, 3.1*, and 3.2*.

***E*°' / V vs $[Cp_2Fe]^{+/0}$**

	$E°'_1$ $[Ni]^{2+/1}$	$E°'_2$ $[Ni]^{+/0}$	$E°'_3$ $[Ni]^{0/-}$	$E°'_4$ $[Ni]^{1-/2-}$	$E°'_2 - E°'_3$
4.1	–0.08	–0.43 (–0.45)	–1.38 (–1.46)	–1.93 (–2.07)	0.93(1.01)
4.2	–0.18	–0.65 (–0.6)	–1.44 (–1.58)	–2.01 (–2.19)	0.8 (0.98)
3.1*	0.13	–0.46	–2.01	–2.76	1.54
3.2*	–0.07	–0.73	–2.15	–2.80	1.42

**Included in table for comparison purposes. Potentials recorded in THF*

The reduction potentials of both the (cat)Ni(acceptor) complexes exhibits the same behavior where $E°'_3$ for (cat)Ni(bpy^{t}Bu$_2$) (**3.1**) is found at –2.01 V in THF and when the *tert*-butyl groups of the acceptor ligand is switched to the ester-functional groups, $E°'_3$ shifts anodically by 0.55 V to –1.46 V. The less negative reduction events exhibited by the bpy^{COOMe} acceptor in both complexes suggests that the electron withdrawing ester functionality lowers the energy of the ligand-localized LUMO, making the acceptor ligand easier to reduce. The oxidation potentials follow the same trend discussed throughout this dissertation, where the potentials are dependent on the identity of the donor ligand.

Complex **4.1**, with the catecholate donor, shows a first oxidation event ($E°'_2$) –0.43 V in MeCN (and –0.45 V in THF). This event appears to be only semi-reversible with a broad and cathodically shifted return wave, similar to its bpy^{t}Bu$_2$ derivative. The $(ap)^{2-}$ donor in **4.2**, exhibits the same event, $E°'_2$ at –0.65 V in MeCN (–0.65 V in THF). The less negative oxidation potential in **4.2** is indicative of a HOMO that is easier to oxidize, consequently due to the strongly reducing $(ap)^{2-}$. Nevertheless, the thermodynamic HOMO–LUMO gap ($E°'_3$ – $E°'_2$) of these complexes follows the same trend as the complexes in Chapter 3 where the

larger HOMO–LUMO gap is observed for the catecholate ligand ($E°'_3 - E°'_2$ = 930 mV) and the amidophenolate ligand shows a smaller gap of 800 mV.

4.2.3 Absorption Features

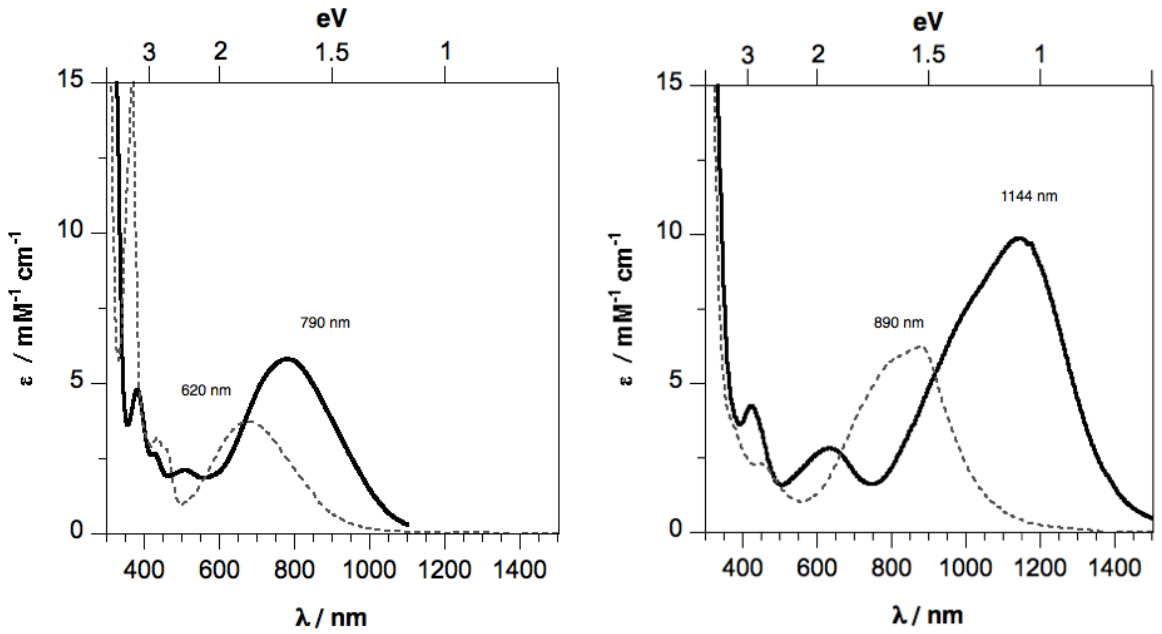

Figure 4.3 UV–vis–NIR absorption spectra of **4.1** (black line) and **3.1** (dotted grey line), left; and **4.2** (black line) and **3.2** (dotted grey line), right.

Complexes **4.1** and **4.2** are deeply colored in both the solid state and in solution, reflecting strong absorptive properties in the visible region of the electromagnetic spectrum. **Figure 4.3** shows the absorption spectra of (cat)Ni(bpy^{COOMe}) **4.1** and (ap)Ni(bpy^{COOMe}) **4.2** compared to their non-functionalized counterparts, (cat)Ni(bpy^{t}Bu$_2$) **3.1** and (ap)Ni(bpy^{t}Bu$_2$) **3.2**. The measurements were collected as solutions in THF at 298 K. The band maximum (λ_{max}), molar absorptivity (ε), estimated onset of LL′CT transition ($E_{LL'CT}$), and solvatochromic shift value (SS) of each complex are summarized in **Table 4-3**. Inspection of the absorption profiles of **4.1** and **4.2** illustrates the effect on the energy of the LUMO when the acceptor is functionalized with the electron-withdrawing anchoring-

group. For instance, (cat)Ni(bpy^{t}Bu$_2$) has a λ_{max} of 620 nm (2 eV) in THF. When the acceptor ligand is bpy^{COOMe}, the λ_{max} red-shifts to 790 nm (1.57 eV). Likewise, for the (ap)Ni(acceptor) complexes, the band maximum red-shifts 0.28 eV from 890 nm (1.39 eV) to 1120 nm (1.1 eV) with the incorporation of the ester-anchoring group. This red-shift in the lowest energy absorption can be attributed to the drop in the energy of the LUMO by –0.28 eV as the electron withdrawing anchoring groups lower the energy of the π* orbital, thus shrinking the HOMO–LUMO gap. This trend mirrors the trend from the electrochemical data, where the electron-withdrawing ester functionality yields more modest reduction potentials.

Table 4-3 LL'CT Absorption Maxima, Extinction Coefficients, Estimated Excited-State Energies, and Solvatochromic Shift Values for **4.1** and **4.2** compared to **3.1** and **3.2**.

	λ_{max} / nm	ε / M^{-1} cm^{-1}	$E_{LL'CT}$ / eV	Solvatochromic shift
4.1	790	6000	1.1	0.35
4.2	1140	10000	0.9	0.34
3.1	620	3600	1.52	0.45
3.2	890	6200	1.12	0.16

In addition to the shift in energy of the band maxima, **4.1** and **4.2** exhibit greater extinction coefficients (ε) when compared to the non-functionalized dyes. The probability of a promotion of an electron from the HOMO to the LUMO almost doubles when each complex is functionalized with the anchoring groups. The increase in molar absorptivity is indicative of the increased conjugation across the molecule, which could be a result of greater contribution of the acceptor to the HOMO (a concept investigated further in Section 4.2.4). Complex **4.1** exhibited a bathochromic shift in polar solvents, with a specific solvatochromic shift (SS) value of 0.35 (**Table 4-4**). Notably, this value is less than the SS value derived for complex **3.1** (SS = 0.45). Complex **4.2** exhibited the same negative

solvatochromic behavior as **4.1**, with a SS of 0.34. Interestingly, the SS value for **4.2** becomes larger when compared to the non-functionalized dye **3.2**, not smaller, as is the case for **4.1**. Such a result suggests that the incorporation of the electron-withdrawing anchoring group weakens the ground-state dipole in **4.1** and strengthens it in **4.2**.

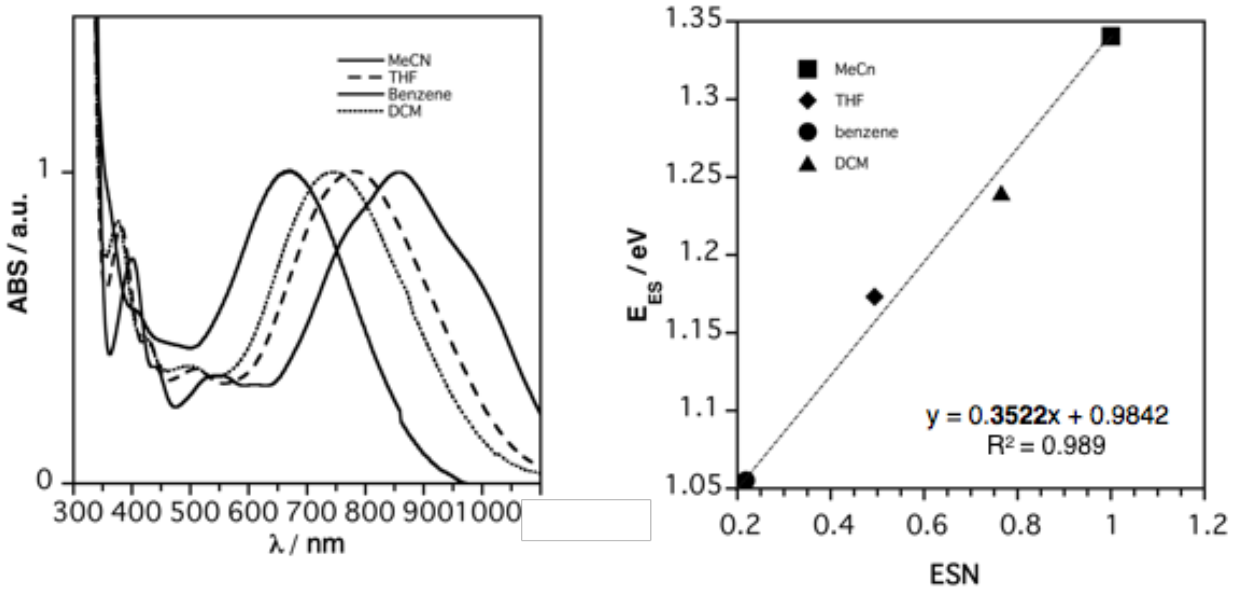

Figure 4.4 Normalized ground state electronic absorption spectra of **4.1** recorded in a variety of solvents (left) and Plot of the linear correlation between the energy of the charge transfer state and the solvent polarity, with a slope (solvatochromic shift) of 0.35 eV (2840 cm^{-1}) (right).

The charge-transfer nature of the lowest energy absorption band for each complex is further verified through solvatochromic studies. Previously, CT transitions of D-A LL'CT complexes have been shown to display negative solvatochromism; namely the shift of the LL'CT band maximum to higher energy in increasing solvent polarity.[17] This behavior is exemplified for **4.1** in **Figure 4.4**, where the electronic absorption spectrum is recorded in a variety of solvents. The red shift for the λ_{max} from 650 nm in MeCN to 790 nm in THF is indicative of the decrease in magnitude of the dipole moment of the LL'CT state.[18]

4.2.4 DFT

Density Functional Theory (DFT) computations were conducted to model the electronic properties of complexes **4.1** and **4.2**. The single-crystal structure of **4.2** was used as a starting point for geometry optimizations for both complexes. Before optimizations were calculated, the following structural simplifications were made using the program Avogadro: the *tert*-butyl groups of both donor ligands, the methyl substituents of the esters, and the isopropyl groups on the phenyl of the $(ap)^{2-}$ ligand were replaced with hydrogen atoms. Substitution of these bulky alkyl groups with hydrogen atoms was necessary in order to maintain tight convergence and has no affect on the outcome of the calculations. The simplified structures of **4.1** and **4.2** were initially refined at the TPSS/SVP level of theory with subsequent structural refinements carried out using the TZVP basis set.

Table 4-4 Metal and Ligand Contributions to the Frontier MO Manifold as Determined by Mulliken Population Analysis.

		Percent Contribution				
	Orbital	**Ni**	**donor ligand**	**bpy^{COOMe}**	**Energy / eV**	**ΔE / eV**
4.1	LUMO +1	2.5	0	**97.5**	–3.10	0.81
	LUMO	10.1	17.3	**72.5**	–3.72	
	HOMO	4.6	**75.3**	20.1	–4.53	
	HOMO –1	29.7	**70.3**	0	–5.25	
4.2	LUMO+1	**52.2**	26.6	21.1	–3.04	0.71
	LUMO	10.8	21.7	**67.4**	–3.52	
	HOMO	6.6	**66.5**	26.8	–4.23	
	HOMO –1	39.1	**60.9**	0	–5.43	

The calculated optimized bond lengths of **4.2** agreed well with the experimental X-ray data of **4.2** where the Ni–O, Ni–N, and intraligand bond distances were calculated within 0.04 Å of the solid-state data. **Figure 4.5** shows the frontier Kohn–Sham orbital diagrams for complexes **4.1** and **4.2** along with POV-Ray renderings of the HOMO and LUMO orbitals.

Table 4-4 contains the energies of these orbitals as well as the percent contribution of the metal, donor and acceptor ligands as determined by Mulliken population analysis. According to the MPA, the HOMO of complex **4.1** is calculated to be at –4.53 eV and localized predominantly on the donor ligand, with the specific contributions of 75.3% $(cat)^{2-}$, 4.6% Ni(II), and 20.1% bpy^{COOMe}. The LUMO of **4.1** is found at –3.72 eV and is localized mostly on the acceptor ligand, with specific contributions of, 72.5% bpy^{COOMe}, 17.3% Ni(II) , and 17.3% $(cat)^{2-}$. Likewise, the HOMO-1 and the LUMO+1 of (cat)Ni(bpy^{COOMe}) are comprised of mostly donor and acceptor ligand, respectively. The highest occupied MO to be primarily metal-based is the HOMO-2, which is localized in the dz^2 orbital and falls at –5.6 eV. The lowest unoccupied metal-based molecular orbital is the LUMO+2, which is localized on the $dx^2–y^2$ orbital, and falls at –3.02 eV. The splitting of the ligand field gives a 2.54 eV gap, where several ligand localized frontier orbitals have been electronically inserted. The HOMO of (ap)Ni(bpy^{COOMe}) (**4.2**) is +0.32 eV higher in energy that the catecholate HOMO of **4.1**, with a specific energy of –4.28 eV, which makes sense considering the one oxygen atom is replaced with nitrogen atom. Expectedly, it is localized mostly on the donor ligand with specific contributions of 66.5% $(ap)^{2-}$ ligand, 6.6% Ni(II), and 26.8% bpy^{COOMe}. Notably, there is a 10% increase in acceptor character in the HOMO of **4.2** compared to the HOMO of **4.1**. The LUMO of **4.2** is found at –3.52 eV. It is localized primarily on the acceptor ligand and specifically comprised of 64.5% bpy^{COOMe}, 17.3% Ni(II) and 17.3% $(cat)^{2-}$. The HOMO-1 for **4.2** is just like the HOMO-1 in **4.1** in that it is comprised of just metal and donor orbitals. The difference is (cat)Ni(bpy^{COOMe})'s HOMO-1 is 29.7% metal and 70.3% acceptor, while (ap)Ni(bpy^{COOMe})'s HOMO-1 contains about ten percent more metal character (39.1%) and about 10% less contribution from the acceptor ligand.

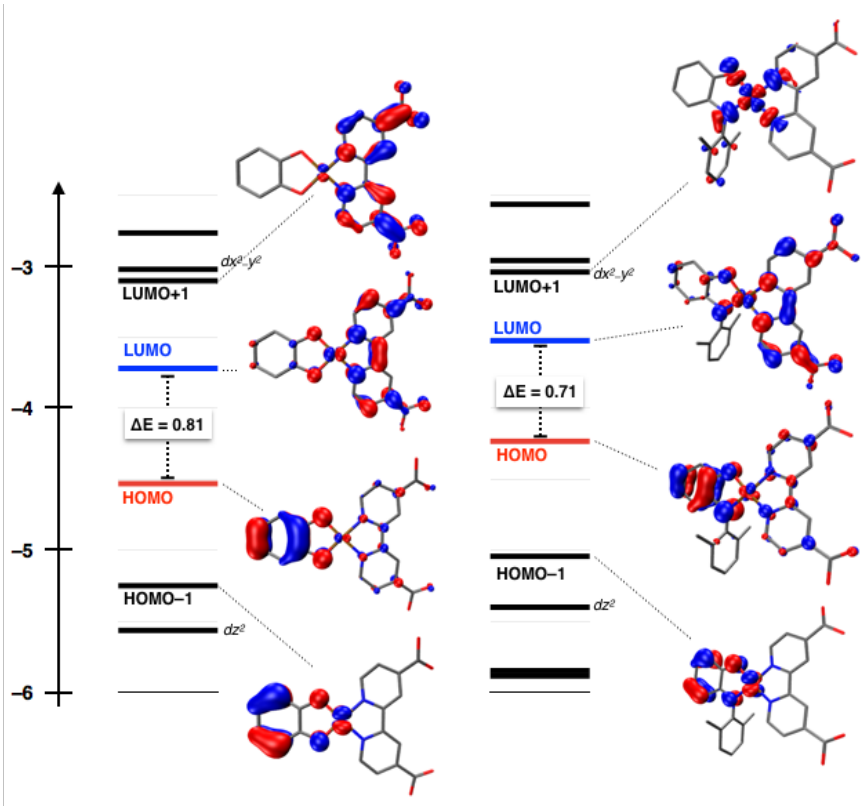

Figure 4.5 Frontier Kohn-Sham orbital diagram for (cat)Ni(bpy^{COOMe}), **4.1** (left) and (ap)Ni(bpy^{COOMe}), **4.2** (right) as determined by DFT computations at the TPSS/TZVP level of theory.

The compositions of the HOMO-1 to LUMO are generally the same for both complexes with the exception that there is more delocalization present in each orbital of (ap)Ni(bpy^{COOMe}) than in (cat)Ni(bpy^{COOMe}). The LUMO+1, however, does differ between complex **4.1** and **4.2**. The LUMO+1 for (cat)Ni(bpy^{COOMe}) (**4.1**) appears to be a bpy^{COOMe} π* orbital where it is comprised of 97.5% acceptor ligand. And the LUMO+2 (not shown) is the M-L σ* orbital. This is in contrast to **4.2**, where the LUMO+1 is the M-L σ* orbital with 52.2% metal character, 26.6% donor character, and 21.1% acceptor character. The LUMO+2 contains 95.8% acceptor character with the remaining 4.2% being contribution from the metal center. Where the M-L σ* orbital in **4.1** is above the second bpy^{COOMe} π*, it drops below the bpy^{COOMe} π* in complex **4.2**. This reflects the same trend discussed in

Chapter 3 where the catecholate complex provides a stronger ligand field than the amidophenolate ligand.

4.2.5 TD-DFT

With the prerequisite ground-state calculations in hand, time dependent DFT (TD-DFT) calculations (TPSS/TZVP+THF) were performed to find the characters and energies of the singlet low-lying excited states of complexes **4.1** and **4.2**. The energy of each excited state is the vertical excitation energy in electron-volts (eV) from the ground state.[21] The first five transitions with the greatest oscillator strengths for each complex are listed in **Table 4-5**, along with their energies, transitions, and character. This information is also presented graphically for all calculated excited-states in **Figure 4.6**. In complexes **4.1** and **4.2**, there are excited-states with significant oscillator strength throughout the 1.2-3 eV region, but the strongest are clustered around 1.25 eV. These transitions are reasonably strong with calculated oscillator strengths of 0.2124 for **4.1** and 0.1528 and 0.1048 for **4.2**. There were no calculated excitations below 1 eV in either complex. For some transitions in **Table 4-5**, a simplistic model of excited-state excitations can be applied where a transition corresponds to the promotion of an electron from an occupied MO (Φ_O) to an unoccupied MO (Φ_U). Some excited-states, however, show optical transitions that correspond to multi-electronic states, where a linear combination of two, occupied-to-unoccupied MO excitations comprise a given transition. The character of each excited-state was assigned according to the compositions of the occupied and unoccupied MOs of the dominant excitation(s). For example, for (cat)Ni(bpy^{COOMe}) (**4.1**) the first singlet excitation occurs at 1.24 eV and corresponds to a promotion from the HOMO, which is 75% donor ligand, to the

LUMO, which is 72% acceptor ligand. This first singlet excitation is designated LL'CT. The first singlet excitation for (ap)Ni(bpy^{COOMe}) (**4.2**) is the combination of two different transition: 56% of it corresponds to a transition from the HOMO which is 66% donor ligand, to the LUMO that is 67% acceptor ligand. This transition can be designated LL'CT. The second transition, which makes up 42% of the excitation corresponds to a promotion from the donor-based HOMO to the LUMO+1, which is 53% metal, and therefore can be assigned ligand-to-metal charge transfer (LMCT). With 56% being LL'CT and 42% being LMCT, the overall character of the excitation is designated: mixed LL'CT / LMCT.

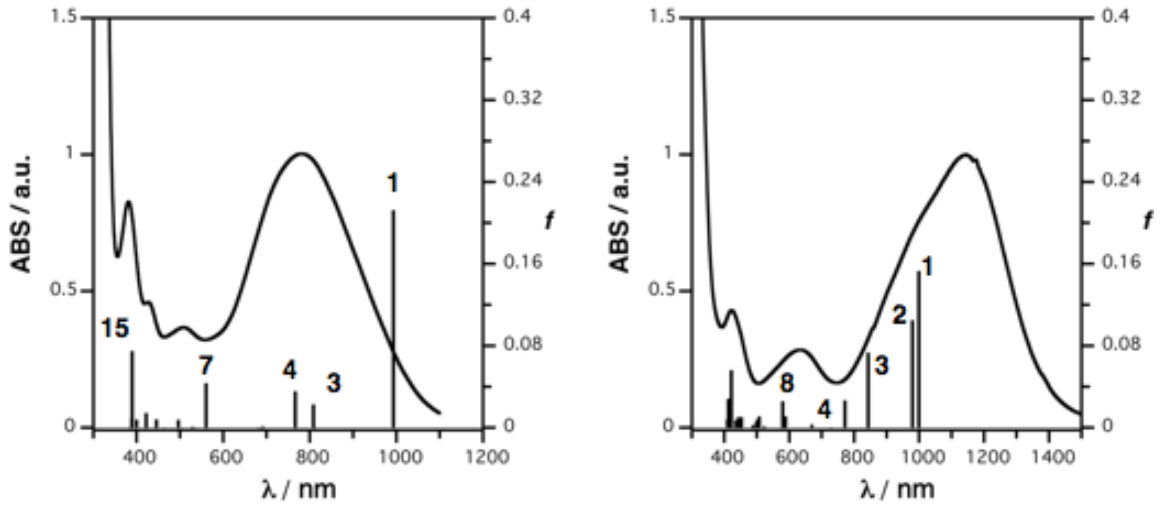

Figure 4.6 Calculated singlet excitations for **4.1** (left) and **4.2** (right) vs. oscillator strengths (*f*) overlaid against the normalized experimental spectra collected in THF at 298 K.

Table 4-5 Selected Calculated Singlet Excited States for **4.1** and **4.2**.

	State	E/eV(nm)	*f*	$\Phi_O \rightarrow \Phi_U$	Character
4.1	1	1.24 (993)	0.212	HOMO → LUMO	LL'CT
	3	1.53 (808)	0.023	HOMO → LUMO+1 (70%) HOMO-1 → LUMO (30%)	LL'CT
	4	1.61 (766)	0.356	HOMO-1 → LUMO (71%) HOMO → LUMO (29%)	LL'CT
	7	2.21 (560)	0.044	HOMO → LUMO+1	LL'CT
	15	2.95 (421)	0.143	HOMO-4 → LUMO+4 (54%) HOMO-2 → LUMO+2 (41%)	LL'CT / $dz^2 \rightarrow dx^2\text{-}y^2$

	1	1.24 (999)	0.1528	HOMO → LUMO (56%) HOMO → LUMO+1 (42%)	LL′CT / LMCT
4.2	2	1.27 (979)	0.1048	HOMO → LUMO+1 (55%) HOMO → LUMO (40%)	LMCT/ LL′CT
	3	1.47 (842)	0.0732	HOMO → LUMO+2	LL′CT
	4	1.61 (771)	0.0267	HOMO-1 → LUMO	LL′CT
	8	2.14 (580)	0.0258	HOMO-1→ LUMO+2	LL′CT

The calculated excitations agree with the experimental data (spectra of **4.1** and **4.2** taken in THF at 298K, **Figure 4.6**). For both complexes, the excitation that gives the highest oscillator strength is the lowest energy transition. For complex **4.1**, excitation to the first singlet excited-state corresponds to a promotion of an electron from the HOMO to the LUMO and is calculated to fall at 1.24 eV (993 nm). Although the strength of this excitation does not align with the molar absorptivity observed in the experimental data, the energy of it does align within the onset of lowest energy absorption. The second excitation calculated for **4.1** yielded an oscillator strength of zero and although present in the molecule's excite-state manifold, it does not contribute to the compound's absorption cross-section and thus is not considered further. The third excitation, calculated at 1.53 eV is a linear combination of two transitions, one from the HOMO to the LUMO+1 and the other from the HOMO-1 to the LUMO and are assigned as LL′CT. Transitions 4 and 7 are solely LL′CT, while transition 15 is mixed LL′CT, with 41% contribution from a $dz^2 \rightarrow dx^2\text{-}y^2$ transition (HOMO-2 to LUMO+2).

The weaker ligand field imposed by the $(ap)^{2-}$ donor ligand in **4.2** causes mixing of the metal $dx^2\text{-}y^2$ orbital into the two lowest energy transitions which fall at 999 nm and 979 nm. Both of these excitations are linear combinations of the transition between the

HOMO and LUMO, and HOMO to LUMO+1. Their compositions are inverse to each other, where the excitation at 999 nm is 56% HOMO to LUMO, the second excitation (808 nm) is 55% HOMO to LUMO+1. This mixing of metal-to-ligand charge-transfer transition into the LL'CT excitation is due to the LUMO+1 being M-L σ* in character. Transitions 3,4, and 8 are solely LL'CT and correspond to the transition from the donor localized HOMO or HOMO-1 to the acceptor localized LUMO or LUMO+2. The energy of these transitions and the oscillator strengths agree well with the experimental measurement.

The transitions that dominate the visible to NIR region of the electromagnetic spectrum of complexes **4.1** and **4.2** are majority LL'CT in nature. The lowest energy d→d transition for complex **4.1** is 1.71 eV above the energy of the ground state. In contrast, the weaker ligand field imposed on complex **4.2** gives a LUMO+1 that is M-L σ*character and causes some mixing in the two lowest energy transitions, making each posses considerable ligand-to-metal charge-transfer character.

4.2.6 Estimating the Excited State and Preliminary Binding Studies

Estimated excited-state redox potentials were determined for each complex based on the ground state electrochemical potentials (taken in THF) and estimated optical excitation energy, taken from **Table 4-3**, Section 4.2.3. The derived values for $E^{+/*}$ show that upon absorption of a low energy photon (0.9 and 1.2 eV), complexes **4.1** and **4.2** exhibit $E^{+/*}$ values of –0.99 and –0.94 V vs. SCE, respectively. Although these values are less negative and therefore less potent than $[Ru(bpy)_3]^{2+}$'s singlet excited state (^{1}MLCT = $E^{+/*}$ = –1.2), they are more negative than the triplet state, ^{3}MLCT = $E^{+/*}$= -0.86 V vs. SCE, which is still known to inject electrons into TiO_2. These estimations are at more negative potentials

than the conduction band of TiO_2 (–0.82 V vs SCE) and suggest electron injection is possible. Complexes **4.1** and **4.2** are estimated to access comparable excited-state oxidation potentials to the ^{3}MLCT of $Ru(bpy_3)^{2+}$ with considerably less energy (1.1 and 0.9 eV).

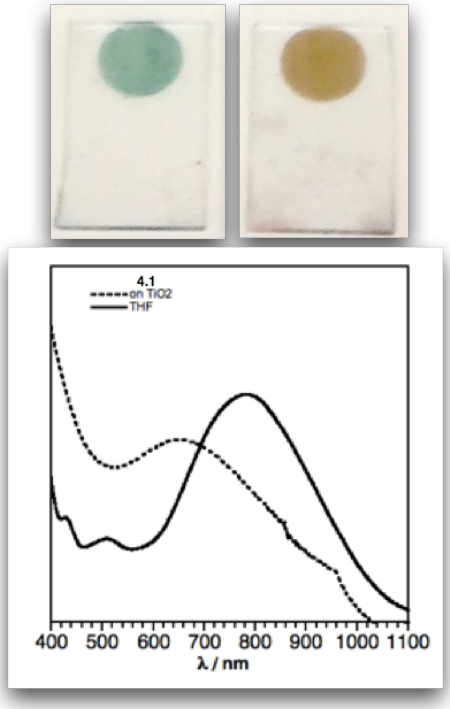

Figure 4.7 Thin films coated with dye **4.1** (top left) and **4.2** (top right) and UV–vis–NIR spectra of **4.1** in a THF solution (solid line), and when anchored to TiO^2 (dashed line).

The tethering of **4.1** and **4.2** to a TiO_2 surface requires the hydrolysis of the ester functionality so the carboxyl anchoring groups can interact with the Ti(3d) conduction band of the manifold. Common deprotection methods require acidic or basic conditions in aqueous solvents and because we assume **4.1** and **4.2** are not stable aqueous solutions, we sought a more benign pathway to deprotection and sensitization of TiO_2. Following the method introduced by Lindquist et al., freshly prepared thin films of nanocrystalline TiO_2 were base treated for 40 hours in 1M LiO^tBu/hexane solution. After forty-eight hours of

soaking, the thin films were quickly removed from solution, washed with hexanes, and immediately immersed in THF solutions of **4.1** and **4.2**. The resulting surface anions of the base-treated films reacted with the ester unit(s) of the Ni(II) dyes and led to an *in situ* de-esterification and the formation of the desired carboxylate unit(s), which could then bind to the TiO_2 surface.[22] After soaking the films for the appropriate amount of hours, a functionalized thin film of **4.1** resulted in a color change from white to an intense blue-green (**Figure 4.7**, *top left*) and an amber-brown color for **4.2** (**Figure 4.7**, *top right*). Several washings of the thin films with THF did not remove the color. This was encouraging as the color of the films closely matched the color of the dyes while in solution and suggested successful dye adsorption. The UV-vis-NIR absorption spectra of the thin film coated in **4.1** is shown in **Figure 4.7**, where it clearly shows a broad band in the region of 680-700 nm and on onset of 1000 nm. The absorbance feature corresponds to the LL'CT bands observed in the solution phase spectra, although being blue-shifted. The thin film coated in **4.2** although strongly colored, produced a less promising spectrum than non-tethered **4.2**, as the absorption features are minimal and degraded over a short period of time in air. Although **4.1** exhibited air stability long enough to take spectral measurements, it too degraded in air shortly thereafter.

4.3 Summary and Outlook

The square-planar Ni(II) D-A LL'CT dyes reported herein have been functionalized with two ester functionalities groups at the 4 and 4' positions of the bipyridine acceptor ligand for tethering to metal oxide surfaces. Upon optical excitation, the dyes are potent excited-state reductants and should be able to populate the conduction band of TiO_2.

Complexes **4.1** and **4.2** absorb strongly in the red and NIR portions of the electromagnetic spectrum and possess reversible, ligand-localized redox events. DFT calculations revealed the composition of the photoactive frontier molecular orbitals where in the case of **4.1**, the HOMO-1, HOMO, LUMO, and LUMO+1 are all ligand-based and any molecular orbitals with significant metal contribution have been pushed to lower and higher energies. In contrast, the weak ligand field imposed by the $(ap)^{2-}$ ligand in **4.2** results in greater contribution of the metal orbital mixing of the metal d orbitals throughout the pFMO set. Where the LUMO is predominately bpy^{COOMe} based, the LUMO+1 is the M-L σ* orbital and lies +0.48 eV from the LUMO.

TD-DFT calculations revealed the first lowest energy transitions of **4.1** are LL'CT transitions, while for **4.2,** the low-lying dx^2-y^2 orbital (the LUMO+1) causes the first two transitions to be mixed LL'CT and LMCT. It would be interesting to investigate whether this mixed LL'CT / LMCT transition would facilitate deactivation of the singlet excited-state, as this is a common occurrence with first row transition metal charge-transfer dyes.

Nevertheless, efforts to attached these dyes to nanocrystalline TiO_2 were performed by base-treating the TiO_2 surface using LiO^tBu to deprotonate and turn the surface hydroxyl groups (–OH) into oxygen anions (–O), thus making the surface more reactive toward the ester functionalities of the dye. Although dyes **4.1** and **4.2** appeared to adsorb to the TiO_2 surface, the resulting sensitized films degraded once exposed to air and rendered electron injection studies impossible. Although the air sensitivity of these dyes is problematic, future precautions such as air free studies can be made in order to test their efficacy to inject electrons into large band gap semiconductors.

4.4 Experimental

General Considerations. All compounds and reactions reported below show various levels of air- and moisture-sensitivity, so all manipulations were carried out using standard vacuum-line, Schlenk-line and glovebox techniques. Solvents were sparged with argon before being deoxygenated and dried by passage through Q5 and activated alumina columns, respectively. To test for effective oxygen and water removal, aliquots of each solvent were treated with a few drops of a purple solution of sodium benzophenone ketyl radical in THF. The reagents $Ni(cod)_2$ (Strem) and 3,5-di-*tert*-butyl-1,2-quinone (Aldrich) where reagent grade or better and used as received. The iminoquinone, 3,5-di-*tert*-butyl(2,6-diisopropylphenyl) orthoiminoquinone[32] was prepared according to literature procedure. The diimine ligand, 4,4'-di-methyl-bipyridine (Aldrich), was oxidized and then methylated to yield: dimethyl 2,2'-bipyridyl-4,4'-dicarboxylate.

Spectroscopic Measurements. NMR spectra were collected at 298 K on a BrukerAvance 400 MHz or 500 MHz spectrometer in dry, degassed C_6D_6 or $CDCl_3$. ^1H NMR spectra were referenced to tetramethylsilane (TMS) using the residual ^1H impurities of the deuterated solvent. All chemical shifts are reported using the standard δ notation in parts per million; positive chemical shifts are to a higher frequency of TMS. Electronic absorption spectra were recorded with a PerkinElmer Lamda 900 UV-vis-NIR Spectrometer using one-centimeter path-length cells at ambient temperature (20-24 °C).

Electrochemical Methods. Electrochemical experiments were recorded on a Gamry Series G300 potentiostat/galvanostat/ZRA (Gamry Instruments, Warminster, PA) using a 3.0 mm glassy carbon working electrode, a platinum wire auxiliary electrode, and a silver wire pseudo-reference electrode. Reversibility of a redox process was judged based on the

ratio of the anodic to the cathodic current being close to unity (ipa/ipc ≅ 1) for a given process. Electrochemical experiments were performed at ambient temperature (20-24 °C) in a nitrogen-filled glovebox using THF solutions containing 1 mM analyte and 100 mM $[NBu_4][PF_6]$ as the supporting electrolyte. All potentials are referenced to $[Cp_2Fe]^{+/0}$ using ferrocene or decamethylferrocene (−0.49 V vs $[Cp_2Fe]^{+/0}$)[26] as internal standards. Ferrocene and decamethylferrocene (Acros) were purified by sublimation under reduced pressure and tetrabutylammonium hexafluorophosphate (Acros) was recrystallized from ethanol three times and dried under vacuum.

X-ray Data Collection and Reduction. X-ray diffraction data for all complexes were collected on single crystals mounted on either a glass fiber or a cryoloop and coated with oil. Data were acquired using a Bruker SMART APEX II diffractometer at 143 K using Mo Kα radiation (λ = 0.71073 Å). The APEX2[27] program package was used to determine unit-cell parameters and for data collection. The raw frame data were processed using SAINT[28] and SADABS[29] to yield the reflection data file. Subsequent refinement cycles were carried out using the SHELXTL program suite.[30] Analytical scattering factors for neutral atoms were used throughout the analyses.[31] ORTEP diagrams were generated using ORTEP-3 for Windows.[32] Diffraction data for **4.2** is given in **Table 4-6**.

Density Functional Theory Computations. Calculations were performed in the Molecular Modeling Facility in the Department of Chemistry at UC Irvine. Calculations were performed employing Meta-GGA functional TPSS.[32] Geometry optimizations were initiated using a split-valence plus polarization basis set (def2-SVP)[33] and further refine using the polarized triple-ζ basis set def2-TZVP.[34] The structure of **4.2** obtained from single-crystal X-ray diffraction experiments were used as the starting points for geometry optimizations;

no molecular symmetry was imposed. For complexes **4.1** and **4.2**, molecular geometries and orbital energies were evaluated self-consistently to tight convergence criteria (energy converged to 0.1 μHartree, maximum norm of the Cartesian gradient ≤ 10−4 a.u.). Mulliken population analyses were obtained at TPSS/TZVP theory level; the contour values were 0.03 for the molecular orbital plots. All calculations were performed using the quantum chemistry program package TURBOMOLE.[35,36]

Table 4-6. X-ray diffraction data collection and refinement parameters for (ap)Ni(bpy^{COOMe})•2 C_4H_8O

	4.2
empirical formula	$C_{40}\ H_{49}\ N_3\ Ni\ O_3$
formula weight	710.53 + (2*72.11) = 854.75
crystal system	Monoclinic
space group	$P2_1/c$
a / Å	10.2568(9)
b / Å	19.4457(18)
c / Å	15.3511(14)
α / deg	90
β / deg	107.5750(12)
γ / deg	90
V / Å^3	2918.9(5)
Z	4
refl. collected	35094
indep. refl.	7204 [R(int) = 0.0419]
R1 ($I > 2\sigma$)[a]	0.0337 (0.0505)
wR2 (all data)[b]	0.0731 (0.0794)

TiO_2 Binding Studies. The binding of anchor-functionalized 2,2'-bipyridine complexes was studied using 6 μm thick films of nanocrystalline anatase TiO_2 (20 nm average particle size) on glass slides prepared according to a literature procedure.[37] The TiO_2 films were soaked in 0.5 mM solutions of the complex dissolved in diethyl ether or THF. To check for binding the films were removed from the solution, rinsed with clean solvent, and the UV-vis-NIR spectra were recorded. UV-vis-NIR spectra of films were

recorded on a Perkin-Elmer Lambda 950 spectrophotometer equipped with a 60 mm integrating sphere.

Synthesis of (cat)Ni(bpy^{COOMe}) (4.1). Complex **4.1** was prepared by treatment of a $Ni(cod)_2$ (69 mg, 0.25 mmol, 1 equiv) THF solution with one equivalent of dimethyl 2,2'-bipyridyl-4,4'-dicarboxylate (68 mg, 0.25 mmol, 1 equiv) to generate a purple solution. After 20 minutes of stirring, the putative (cod)Ni(bpy^{COOMe}) intermediate was then treated with a solution of quinone (55 mg, 0.25 mmol, 1 equiv) and stirred for 24 hours. The volume of the resulting brown solution was reduced; ether was added and cooled to –35 ºC. The solid was collected over a frit and washed with cold ether to yield **4.1** as a blue green microcrystalline solid (114 mg, 76% yield). ^{1}H NMR 400 MHz (C_6D_6): δ/ppm 1.58 (s,9H), 1.71 (s, 9H), 1.47 (9H), 3.47 (s, 6H), 6.59 (d, J = 9.8 Hz, 2H), 7.19 (s, 4H), 7.44 (s, 1H), 7.52 (s, 1H), 7.52 (s, 1H), 7.95 (s, 1H), 8.35 (s, 1H), 8.87 (s, 1H). UV–vis–NIR [THF; λ_{max}/nm (ε/$M^{-1}cm^{-1}$)]: 314 (19000), 800 (5800).

Synthesis of (ap)Ni(bpy^{COOMe}) (4.2). Complex **4.2** was prepared by treatment of a $Ni(cod)_2$ (69 mg, 0.25 mmol, 1 equiv) THF solution with one equivalent of dimethyl 2,2'-bipyridyl-4,4'-dicarboxylate (68 mg, 0.25 mmol, 1 equiv) to generate a purple solution. After 20 minutes of stirring, the putative (cod)Ni(bpy^{COOMe}) intermediate was then treated with a chilled solution of iq (95 mg, 0.25 mmol, 1 equiv) and stirred for 24 hours. The volume of the resulting green solution was reduced; pentane was added and cooled to –35 ºC. The solid was collected over a frit and washed with cold ether to yield **4.2** as a green microcrystalline solid (160 mg, 90%). ^{1}H NMR 400 MHz (C_6D_6): δ/ppm 1.18-1.14 (m, 18H), 1.44 (s, 9H), 1.93 (s, 9H), 3.33 (s, 6H), 4.24-4.22 (m, 2H), 6.36 (s, 1H), 7.04 (s, 1H), 7.29 (s,

3H), 7.35 (d, J = 0.6, 3H), 7.40 (d, J = 6.4, 1H), 7.70 (s, 2H). UV–vis–NIR [THF; λ_{max}/nm (ε/M^{-1} cm^{-1})]: 314 (3000), 1140 (10000).

4.5 References

(1) Scanlon, D. O.; Dunnill, C. W.; Buckeridge, J.; Shevlin, S. A.; Logsdail, A. J.; Woodley, S. M.; Catlow, C. R. A.; Powell, M. J.; Palgrave, R. G.; Parkin, I. P.; *et al. Nature Materials* **2013**, *12*, 798–801.

(2) Chen, X.; Mao, S. S. *Chem. Rev.* **2007**, *107*, 2891–2959.

(3) Zhang, G.; Kim, G.; Choi, W. *Energy Environ. Sci.* **2014**, *7*, 954–966.

(4) O'Regan, B.; Grätzel, M. *Nature* **1991**, *353*, 737–740.

(5) Ellingson, R. J.; Asbury, J. B.; Ferrere, S.; Ghosh, H. N.; Sprague, J. R.; Lian, T. A.; Nozik, A. J. *J. Phys. Chem. B* **1999**, *102*, 6455-6458.

(6) Hagfeldt, A.; Grätzel, M. *Acc. Chem. Res.* **2000**, *33*, 269-277.

(7) Ardo, S.; Meyer, G. J. *Chem. Soc. Rev.* **2008**, *38*, 115.

(8) Juris, A.; Balzani, V.; Barigelletti, F.; Campagna, S.; Belser, P.; Zelewsky, von, A. *Coord. Chem. Rev.* **1988**, *84*, 85–277.

(9) Nazeeruddin, M. K.; Péchy, P.; Renouard, T.; Zakeeruddin, S. M.; Humphry-Baker, R.; Comte, P.; Liska, P; Cevey, L.; Costa, E.; Shklover, V. *J. Am. Chem. Soc.* **2001**, 123, 1616-1624.

(10) Han, Z.; Eisenberg, R. *Acc. Chem. Res.* **2014**, *47*, 2537–2544.

(11) Zheng, B.; Sabatini, R. P.; Fu, W.-F.; Eum, M.-S.; Brennessel, W. W.; Wang, L.; McCamant, D. W.; Eisenberg, R.. *Proc. Natl. Acad. Sci. U.S.A.* **2015**, *112*, E3987–E3996.

(12) Zhang, J.; Du, P.; Schneider, J.; Jarosz, P.; Eisenberg, R. *J. Am. Chem. Soc.* **2007**, *129*, 7726–7727.

(13) William B Connick; David Geiger, A.; Eisenberg, R. *Inorg. Chem.* **1999**, 38, 3264-3265.

(14) Zhao, J.; Wu, W.; Sun, J.; Guo, S. *Chem. Soc. Rev.* **2013**, *42*, 5323–5351.

(15) a) Biner, M.; Buergi, H. B.; Ludi, A.; Roehr, C. *J. Am. Chem. Soc.* **1992**, *114* (13), 5197–5203. b) Chaudhuri, P.; Verani, C. N.; Bill, E.; Bothe, E.; Weyhermüller, T.; Wieghardt, K. *J. Am. Chem. Soc.* **2001**, *123* (10), 2213–2223.

(16) a) Brown, S. N. *Inorg. Chem.***2012**, *51*, 1251–1260. b) Sik Min, K.; Weyhermüller, T.; Wieghardt, K. *Dalton Trans.* **2003**, 1126–1132.

(17) Kramer, W. W.; Cameron, L. A.; Zarkesh, R. A.; Ziller, J. W.; Heyduk, A. F. *Inorg. Chem.* **2014**, 140806135722006.

(18) Miller, T. R.; Dance, I. G. *J. Am. Chem. Soc.* **1973**, *95*, 6970–6979.

(19) Manuta, D. M.; Lees, A. J. *Inorg. Chem.* **1986**, *25*, 3212–3218.

(20) Cummings, S. D.; Eisenberg, R. T. *J. Am. Chem. Soc.* **1996**, *118*, 1949–1960.

(21) Monat, J. E.; Rodriguez, J. H.; McCusker, J. K. *J. Phys. Chem. A* **2002**, *106*, 7399–7406.

(22) He, J.; Hagfeldt, A.; Lindquist, S.-E.; Grennberg, H.; Korodi, F.; Sun, L.; Åkermark, B. *Langmuir* **2001**, *17*, 2743–2747.

(23) G. A. Abakumov, *Russ. Chem. Bull*., 2003, **52**, 712.

(24) G. A. Abakumov, V. K. Cherkasov, N. O. Druzhkov, Y. A. Kurskii, G. K. Fukin, L. G. Abakumova, and T. N. Kocherova, S*ynth. Comm*., **2006**, 36, 3241.
(25) H. Gottlieb, V. Kotlyar, A. Nudelman, *J. Org. Chem*., **1999**, 62, 7512.
(26) N. G. Connelly, and W. E. Geiger, *Chem. Rev*., **1996,** 96, 877.
(27) APEX2 Version 2013.6-2, Bruker AXS, Inc.; Madison, WI 2013.
(28) SAINT Version 8.32b, Bruker AXS, Inc.; Madison, WI 2012.
(29) Sheldrick, G. M. SADABS, Version 2012/1, Bruker AXS, Inc.; Madison, WI 2012.
(30) Sheldrick, G. M. SHELXTL, Version 2014/7, Bruker AXS, Inc.; Madison, WI 2014.
(31) International Tables for Crystallography, A. J. C. Wilson, Ed.; Kluwer Academic, Dordrecht, Netherlands, **1992**, Vol. C.
(32) L. J. Farrugia, *J. Appl. Crystallogr*., **1997**, 30, 565.
(33) J. Tao, J. P. Perdew, V. N. Staroverov, and G. E. Scuseria, *Phys. Rev. Lett*., **2003**, 91, 146401.
(34) A. Schäfer, H. Horn, and R. Ahlrichs, *J. Chem. Phys*., **1992**, 97, 2571.
(35) A. Schäfer, C. Huber and R. Ahlrichs, *J. Chem. Phys*., **1994**, 100, 5829.
(36) TURBOMOLE V6.3, Turbomole GmbH, Karlsruhe, 2011. http://www.turbomole.com.
(37) F. Furche, R. Alrichs, C. Hättig, W. Klopper, M. Sierka and F. Weigend, WIREs *Comp. Mol. Chem*., **2014**, 4, 91.
(38) Ito, S.; Murakami, T. N.; Comte, P.; Liska, P.; Grätzel, C.; Nazeeruddin, M. K.; Grätzel, M. *Thin Solid Films* 2008, 516, 4613-4619.

Chapter 5

Octahedral Donor-Acceptor Complexes of Ru(II) Supported by the Redox-Active $N_2N_2^q$ Ligand

5.0 Introduction

Photosensitizers dominated by interligand photo-induced charge transfer i.e., ligand-to-ligand charge transfer (LL'CT) transitions are classically exemplified by square-planar complexes of group 10 metals with the general formulation: (donor)M(acceptor), where donor = catecholate, dithiolate, or amidophenolate; M = Ni(II), Pd(II), or Pt(II); and acceptor = α-diimine.[1-4] The square-planar geometry is ideal because it arranges the ligand-based donor and acceptor orbitals co-planar to one another, ensuring optimal electronic overlap of the photo-active frontier molecular orbitals (pFMOs) while providing the delocalized electronic pathway required to facilitate charge-transfer upon photo-excitation. Although ideal in geometry, the two vacant axial coordination sites make square-planar coordination compounds prone to decomposition through associative ligand-exchange pathways. Another drawback to square-planar photosensitizers is that their planarity has shown to promote π-stacking interactions, both in solution and on metal oxide surfaces, which can compromise efficacy of charge injection through self-quenching pathways.[5,6] In order to realize a more robust LL′CT dye for solar energy conversion strategies it would be advantageous to design a coordinately saturated complex where the geometry and steric interactions inhibits π stacking in solution and on a metal oxide surface.

Octahedral donor-acceptor (D-A) LL′CT complexes have been documented by Lever and coworkers, where they paired two bipyridine acceptor ligands with a series of *ortho*-phenylene donor ligands (*ortho*-phenylene = catecholate, amidophenolate, and *ortho*-phenylenediimine).[7] Their investigations into these complexes illustrated the importance of the co-planar arrangement of donor and acceptor ligands where the resulting LL′CT

transitions were reportedly weak ($\varepsilon \leq 4000\ M^{-1}\ cm^{-1}$) due poor orbital overlap between the donor and acceptor orbitals. [8]

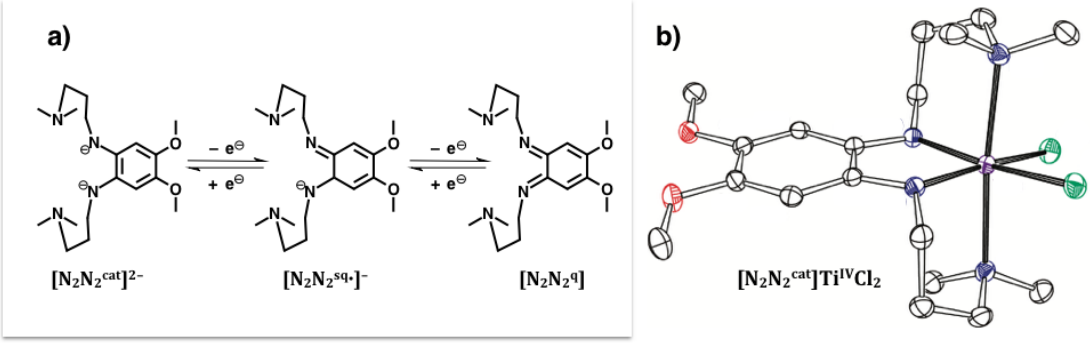

Figure 5.2 a) Oxidation states accessible to the N_2N_2 ligand and b) Crystal structure of $[N_2N_2^{cat}]TiCl_2$. Thermal ellipsoids are drawn at the 50% probability level.[9]

The design and synthesis of octahedral LL′CT chromophores where the respective donor and acceptor ligands are arranged in the basal plane of the octahedron, and thus co-planar to one another should be possible. The redox-active, tetradentate ligand, N,N′-bis-(3-dimethylaminopropyl)-4,5-dimethoxy-benzene-1,2-diiminoquinone ($N_2N_2^q$) could provide the structural ligand platform to achieve this particular coordination environment (**Figure 5.1a**). Developed previously in our lab, the N_2N_2 ligand is redox-active and when coordinated to a transition metal ion can access the three oxidation states inherent to *ortho*-diiminoquinone-type ligands (**Figure 5.1a**).[9] The crystal structure obtained in this study (**Figure 5.1b**) showed the *ortho*-phenylenediamine core occupied two of the four coordination spheres of the basal plane and the tertiary amines arms occupied the two axial positions. This particular arrangement allows for the co-planar installation of another redox-active to realize a LL′CT octahedral dye. This chapter details the synthesis and investigation of octahedral Ru(II) charge-transfer chromophores with the general formulation: (donor)$Ru^{II}(N_2N_2^q)$, where donor = 2 Cl^- (**5.1**); tetrabromocatecholate,

$(catBr_4)^{2-}$ (**5.2**); and 3,5-di-*tert*-butyl-catecholate, $(cat)^{2-}$ (**5.3**). These complexes are investigated spectroscopically, electrochemically, and computationally where I attempt to elucidate the complicated electronic nature of the excited-state manifold.

5.2 Results and Discussion

5.2.1 Synthesis and Characterization

Octahedral ruthenium(II) complexes with the general formulation (donor)Ru($N_2N_2^q$), where donor = $(cat)^{2-}$, $(catBr_4)^{2-}$, and 2 Cl^- were prepared as outlined in **Scheme 5-1**. The ruthenium(II) starting material, $Ru(DMSO)_4Cl_2$ was obtained by the single electron reduction of $RuCl_3 \bullet nH_20$ in refluxing DMSO.[10] A $Ru(DMSO)_4Cl_2$ and toluene slurry was combined with $[N_2N_2^{cat}]H_2$ and excess triethylamine and heated to reflux under inert atmosphere for three days to yield, Ru($N_2N_2^q$)Cl_2 (**5.1**) as a bright-red powder. Installation of the $(catBr_4)^{2-}$ and $(cat)^{2-}$ donor ligands occurred by reacting their catechol derivatives with excess KH to form the di-potassium salt. After removal of unreacted KH by filtration through a glass frit, the solution was combined with one equivalent of **5.1** and stirred at ambient temperature for 24 hours. Displacement of the chloride ligands by the coordination of the $(catBr_4)^{2-}$ or $(cat)^{2-}$ donor ligand was indicated by a drastic color change from red to dark blue or green. The potassium chloride salt was removed by filtration through a glass frit and removal of solvent by vacuum gave the desired complexes, $(catBr_4)$Ru($N_2N_2^q$) (**5.2**) and (cat)Ru($N_2N_2^q$) (**5.3**) in good yields and purity (70-74%).

Scheme 5-2 Synthetic method used in this study.

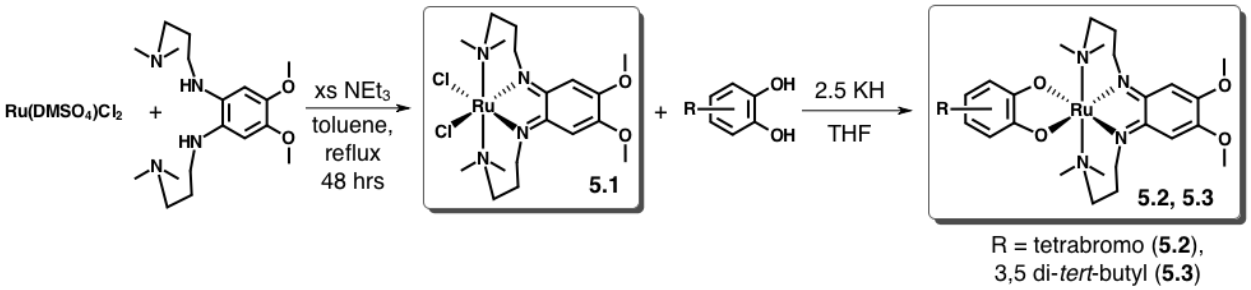

High-quality, single crystals of $Ru(N_2N_2)Cl_2$ (**5.1**) and $(cat)Ru(N_2N_2^q)$ (**5.3**) complexes were obtained by layering a toluene or THF solution with pentane. The confirmed structures are shown as ORTEP diagrams in **Figure 5.2** and the relevant distances are listed in **Table 5-1**. In both cases, the Ru(II) center displayed pseudo-octahedral geometry with the tertiary amine arms of the N_2N_2 ligand occupying the axial positions of the octahedron.

Considering the redox non-innocence of the N_2N_2 ligand, metal center, and (in the case of **5.3**) catecholate ligand, the elucidation of their oxidation states is necessary. Evaluation of key bond lengths within the primary coordination sphere of the Ru(II) ion and within the ligand platforms suggest that both complexes consist of a Ru(II) ion coordinated to the N_2N_2 ligand in it's neutral, diiminoquinone form. This was surprising considering the N_2N_2 ligand was installed in the $[N_2N_2^{cat}]^{2-}$ oxidation state. Nevertheless, C=N bonds for **5.1** and **5.3** measure an average 1.34 Å, which is shorter than 1.5 Å observed for carbon-nitrogen single bonds within the same complex but slightly longer than observed carbon-nitrogen double bonds of exo-cyclic α-diimines (average 1.30 Å).[2,11] This lengthening of the C=N bonds could be indicative of $[semiquinonate]^-$ character within the N_2N_2 ligand or it could be a result of π back donation from the Ru(II) center as the $N_2N_2^q$ ligand is a π accepting ligand. There are two kinds of Ru-N bonds within **5.1** and **5.3** – the

axial ruthenium to amine bond (Ru-N(2,3)), and the ruthenium to diimine bond (Ru-N(4,1)). In both complexes the Ru-N(2,3) bonds are longer (2.2 Å) than the Ru-N(4,1) bonds (average 1.98 Å). This shortening of the Ru-N(4,1) bonds suggest π back donation from the metal center into the empty π* orbitals of the N_2N_2 ligand.[11] While this back donation shortens the Ru-diimine bonds, it causes a slight lengthening of the C=N bonds in both complexes.

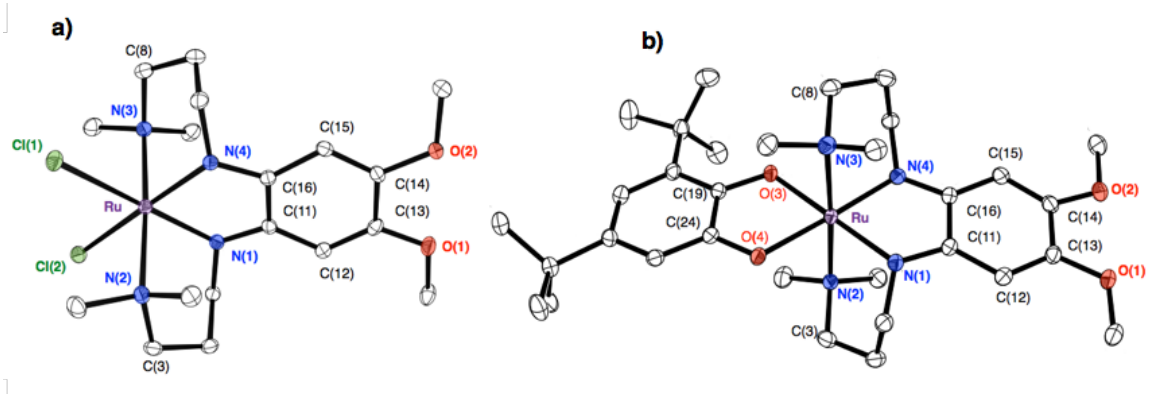

Figure 5.3 ORTEP diagrams of a) Ru($N_2N_2^q$)Cl_2 (**5.1**) and b) (cat)Ru($N_2N_2^q$) (**5.3**). Ellipsoids are shown at 50% probability. Hydrogen atoms and solvent molecules have been omitted for clarity.

For the donor ligand in (**5.3**), the O(3,4)-C(19,24) distances average 1.34 Å and are slightly shorter than the 1.36 Å measured for the other carbon-oxygen single bonds but not short enough for the semiquinonate oxidation state assignment (1.29 Å).[12] Furthermore, localized carbon-carbon double bond character was not observed within the carbon ring. The slight shortening of the carbon-oxygen single bond of the catecholate ligand in **5.3** is reflected in the metrical oxidation state assignment of –1.68. If the catecholate ligand were to be considered in its semiquinonate oxidation state, the MOS value would be closer to –1 than –2. Overall, the crystallographic data support the formal assignment of ruthenium(II) ions coordinated to a neutral $N_2N_2^q$ ligand, and for **5.3**, one dianionic catecholate ligand.

Table 5-1 Selected Metrical Parameters for the Solid-State Structures of $Ru(N_2N_2^q)Cl_2$ (**5.1**) and $(cat)Ru(N_2N_2^q)$ (**5.3**).

$Ru(N_2N_2^q)Cl_2$ (5.1)		**$(cat)Ru(N_2N_2^q)$ (5.3)**	
Bond	**Length (Å)**	**Bond**	**Length (Å)**
Ru-Cl(1)	2.464(5)	Ru-N(1)	1.9899(15)
Ru-Cl(2)	2.448(5)	Ru-N(4)	1.9718(15)
Ru-N(1)	1.980(15)	Ru-N(2)	2.2021(16)
Ru-N(4)	1.990(15)	Ru-N(3)	2.1818(16)
Ru-N(2)	2.211(15)	Ru-O(3)	2.0403(13)
Ru-N(3)	2.218(15)	Ru-O(4)	2.0532(13)
N(1)-C(11)	1.339(2)	N(1)-C(11)	1.346(2)
N(4)-C(16)	1.338(2)	N(4)-C(16)	1.342(2)
N(2)-C(3)	1.513(2)	N(2)-C(3)	1.507(3)
N(3)-C(8)	1.509(2)	N(3)-C(8)	1.499(2)
C(11)-C(16)	1.437(3)	O(3)-C(19)	1.341(2)
C(11)-C(12)	1.431(3)	O(4)-C(24)	1.337(2)
C(12)-C(13)	1.362(3)	O(1)-C(13)	1.360(2)
C(13)-C(14)	1.450(3)	O(2)-C(14)	1.369(2)
C(14)-C(15)	1.363(3)	C(19)-C(24)	1.431(3)
C(15)-C(16)	1.432(2)	C(19)-C(20)	1.408(3)
		C(20)-C(21)	1.400(3)
		C(21)-C(22)	1.402(3)
		C(22)-C(23)	1.394(3)
		C(23)-C(24)	1.396(3)
		C(11)-C(16)	1.443(3)
		C(11)-C(12)	1.422(3)
		C(12)-C(13)	1.369(3)
		C(13)-C(14)	1.422(3)
		C(14)-C(15)	1.362(3)
		C(15)-C(16)	1.422(3)
		MOS	**–1.68**

The NMR spectra of **5.1** and **5.3** are consistent with their solid state structures, and indicative of closed-shell, low-spin, octahedral ruthenium(II) complexes. The C_2 symmetry observed in the solid-state structure of **5.1** is roughly preserved in solution by showing broad, yet discernable peaks within the appropriate regions of the NMR spectrum. The aromatic protons of the diimine backbone and the methoxy protons appear as sharp singlets at 6.92 and 3.89 ppm, respectively. The methylene resonances of the amine arms are split into two sets of three diastereotopic pairs: the down-field and more resolved

resonances at 5.7, 4.6, 3.9 ppm; and the up-field and broadened resonances at 2.2, 1.5, and 1.25 ppm. Similarly, the N-methyl protons appear as two broad singlets at 1.67 and 0.82, respectively. The NMR spectrum of **5.3** is much more resolved and indicative of the C_1 symmetry observed in the solid-state structure. Where the methoxy and N-methyl resonances appear as singlets integrating to 6 protons each for **5.1,** the same resonances are split into two distinct singlets integrating to 3 protons each for complex **5.3** as result of descending in symmetry**.** Likewise, the methylene resonances that appeared as 6 different diastereotopic multiplets in **5.1**, due to the inversion center of the C_1 appear as three different multiplets in **5.3**.

5.2.2 Absorption Profiles

All ruthenium(II) complexes in this series are highly colored in both the solid state and in solution reflecting their intense spectral response in the visible region. The absorption spectra of complexes **5.1**–**5.3** in THF were collected at 298 K and are shown in **Figure 5.3**. Since the acceptor ligand and the metal center are the same in each complex, we can attribute the differences of the absorption profiles to the nature of the donor ligands. The lowest energy transition for $Ru(N_2N_2^q)Cl_2$ (**5.1**) is at 500 nm (2.48 eV, 20 000 cm^{-1}) and is assigned as a MLCT transition, where an electron from the filled metal orbital populates an empty π* orbital on the $N_2N_2^q$ ligand. A modest extinction coefficient of 2800 M^{-1} cm^{-1} for this transition suggests there is weak electronic overlap between the HOMO-localized metal and the acceptor orbitals.

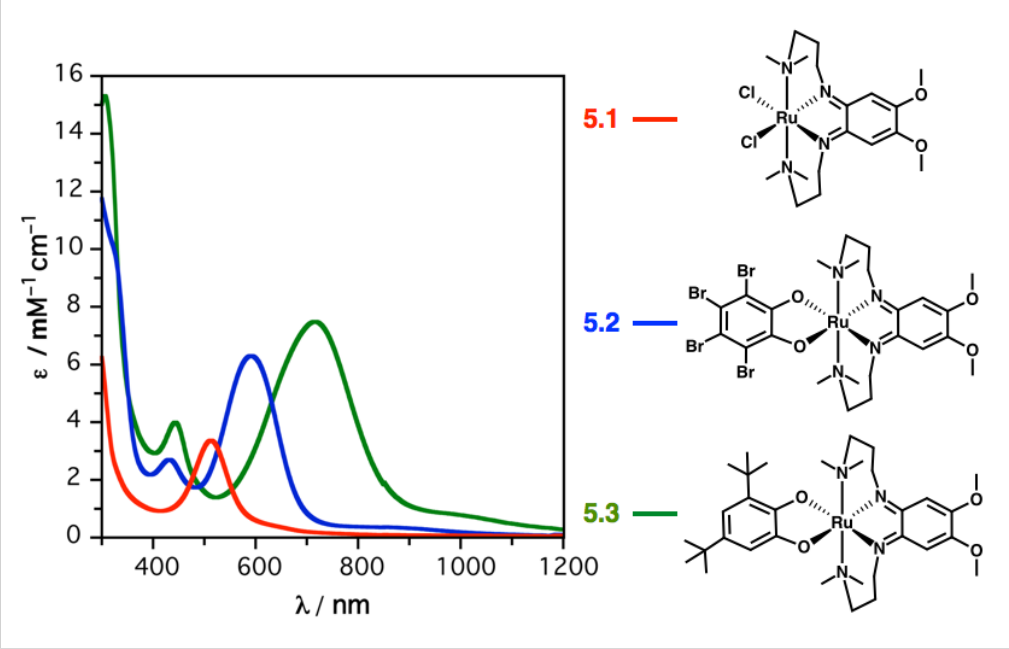

Figure 5.4 UV-vis-NIR absorption spectra of $Ru(N_2N_2^q)Cl_2$ (**5.1**), $(catBr_4)Ru(N_2N_2^q)$ (**5.2**), and $(cat)Ru(N_2N_2^q)$ (**5.3**) taken in THF at 298 K.

When the 2 Cl^- anions are replaced with the $(catBr_4)^{2-}$ donor ligand, as is the case with **5.2**, a new, lower energy absorption band appears at 600 nm and the MLCT transition blue-shifts to 440 nm (from 500 nm). The band maxima of **5.2** is tentatively assigned as a LL'CT owing to the promotion from the HOMO localized on the $(catBr_4)^{2-}$ ligand to the empty π* of the $N_2N_2^q$ acceptor ligand. The MLCT state blue-shifts from 2.48 eV (complex **5.1**) to 2.81 eV. This is reasonable considering that $(catBr_4)^{2-}$ is a much weaker π donor than the chloride anions and the energy of this orbital is stabilized by the removal of the chloride π donor ligands. The LL'CT transition in **5.2** gives a stronger extinction coefficient (6500 M^{-1} cm^{-1}) than the lowest energy absorption for **5.1** (2800 M^{-1} cm^{-1}) indicating better electronic coupling between the donor and acceptor orbitals.

When the electron-withdrawing donor ligand, $(catBr_4)^{2-}$ is swapped for the stronger donor, 3,5-di-*tert*-butyl-catecholate $(cat)^{2-}$ as is the case in **5.3**, another red-shift of the

lowest energy transition to 720 nm (1.72 eV, 13 890 cm^{-1}) occurs. The energy of the MLCT transition (band at 450 nm) is unaltered by the incorporation of the $(cat)^{2-}$ ligand and appears at close to the same energy as **5.2** (440 nm).

5.2.3 Electrochemistry

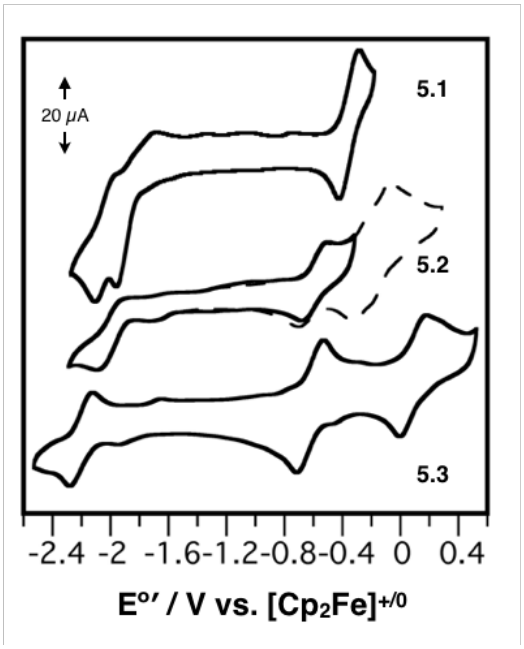

Figure 5.5 Cyclic voltammograms of $Ru(N_2N_2^q)Cl_2$ (**5.1**), $(catBr_4)Ru(N_2N_2^q)$ (**5.2**), and $(cat)Ru(N_2N_2^q)$ (**5.3**). Measurements taken as 1 mM solutions in THF containing 0.1 M $[Bu_4N][PF_6]$ supporting electrolyte. Data were collected at a glassy carbon working electrode, with a platinum wire counter electrode, and a silver wire pseudo-reference electrode using a scan rate of 200 mV s^{-1}.

The ground-state redox behavior of complexes **5.1**-**5.3** was probed by cyclic voltammetry and the results are shown in **Figure 5.4**. Formal potentials referenced against the $[CpFe]^{+/0}$ redox couple are given in **Table 5-2**. The cyclic voltammogram of $Ru(N_2N_2^q)Cl_2$ displays a reversible one-electron event at –0.32 V, assigned as the $Ru^{3+/2+}$ couple. Two irreversible one-electron events at –1.99 and –1.83 V are likely the stepwise reduction of the $N_2N_2^q$ ligand, first to the $[N_2N_2^{sq\bullet}]^-$, and then to the $[N_2N_2^{cat}]^{2-}$ oxidation

state. The lack of reversibility of these events is most likely due to the dissociation of a chloride ligand upon electrochemical reduction.

Table 5-2 Reduction Potentials (V vs. $[Cp_2Fe]^{+/0}$) for Complexes **5.1-5.3** at 298 K in THF.

	E°' / V vs $[Cp_2Fe]^{+/0}$				
	$E°'_1$	**$E°'_2$**	**$E°'_3$**	**$E°'_4$**	**$E°'_2 - E°'_3$**
5.1	NA	–0.32	–1.8	–1.99	1.48
5.2	–0.22	–0.58	–1.9	NA	1.32
5.3	–0.05	–0.64	–2.2	NA	1.56

When the chloride ligands are substituted for the $(catBr_4)^{2-}$ ligand in **5.2**, the first oxidation cathodically shifts from –0.32 V to –0.58 V vs $[Cp_2Fe]^{+/0}$ and is most likely the $Ru^{3+/2+}$ couple. The cathodic shift observed for this event is likely due to replacement of the π donor Cl^- ligands with the $(catBr_4)^{2-}$ ligand which subsequently lowers the energy of the filled metal orbital, making is harder to oxidize. A second oxidation event is observed at –0.22 V and appears to be a two-electron event likely corresponding to the first and second oxidation of the catecholate ligand. Scanning cathodically reveals an irreversible event at –1.9 V vs. $[Cp_2Fe]^{+/0}$ that can be assigned as the first reduction of the $N_2N_2^q$ ligand.

The electrochemical events observed for the (cat)Ru($N_2N_2^q$) (**5.3**) complex reveals a semi-reversible, first oxidation event at –0.64 V and a second, semi-reversible event at –0.05 V. Comparison between the oxidations of **5.2** and **5.3** suggest the –0.64 V event is localized on the metal center, while the second oxidation is most likely localized on the donor ligand. These observations suggest a HOMO localized on the ruthenium center rather than the donor ligands. The electrochemical HOMO-LUMO gap does not follow the same trend observed in the UV–vis–NIR data and suggest that further investigation using

computational methods is needed to elucidate the frontier electronic structure of complexes **5.1**-**5.3**.

5.2.4 DFT

Density functional theory (DFT) computations were conducted to model the electronic properties of complexes **5.1**–**5.3**. The single-crystal structures of **5.1** and **5.3** were used as a starting point for geometry optimizations (**5.3** was used for **5.2**). Geometry optimizations for **5.1**–**5.3** were initially refined at the TPSS/SVP level of theory with subsequent structural refinements carried out using the TZVP basis set. **Figure 5.5** shows the frontier Kohn–Sham orbital diagrams for complexes **5.1**–**5.3** along with POV-Ray renderings of the photoactive frontier molecular orbitals (HOMO+1 through LUMO–1). **Table 5-3** contains the energies of these orbitals as well as the percent contribution of the metal, donor and acceptor ligands as determined by Mulliken population analysis.

Table 5-3 Metal and ligand contributions to the frontier MO manifold as determined by Mulliken population analysis. **5.1–5.3.**

	Orbital	Ru^{2+}	Donor ligand	$N_2N_2^q$	Energy / eV	ΔE / eV
5.1	LUMO +1	**64.16**	6.2	29.64	-1.04	0.617
	LUMO	35.57	4.95	**59.47**	-2.94	
	HOMO	**69.31**	17.64	13.05	-3.55	
	HOMO –1	**74.53**	20.63	4.84	-3.80	
5.2	LUMO+1	0	100	0	-1.33	0.855
	LUMO	31.78	12.36	**55.85**	-2.88	
	HOMO	**72.45**	9.68	17.87	-3.73	
	HOMO –1	5.04	**69.63**	25.33	-4.02	
5.3	LUMO+1	63.31	4.56	32.13	-0.538	0.848
	LUMO	32.00	18.16	49.84	-2.52	
	HOMO	73.26	9.56	17.18	-3.36	
	HOMO –1	3.09	67.69	29.22	-3.57	

According to the population analysis, the HOMO and HOMO-1 of $Ru(N_2N_2^q)Cl_2$ (**5.1**) is expectedly the π*-metal orbital with 75-70% metal character and 20% contribution from

the donor chloride ligands. Removal of the π-donor chloride ligands and incorporation of the redox-active $(catBr_4)^{2-}$ ligand in **5.2** causes a stabilization of both the HOMO and HOMO-1 by –0.2 eV. We expected the HOMO of **5.2** to be localized on the donor ligand, but the calculation predicted 75% contribution from the metal center and only 9 percent contribution from the $(catBr_4)^{2-}$ ligand. The HOMO-1 of **5.2**, however, is comprised of mostly donor ligand (69.6%), with a smaller contribution from the acceptor ligand (25.3%), and limited involvement from the metal center (5%). Swapping the $(catBr_4)^{2-}$ donor ligand with the $(cat)^{2-}$ ligand in **5.3**, causes a destabilization of the HOMO and HOMO-1 orbitals by +0.4 eV. Both of which are calculated to have almost identical composition as those of **5.2**, where the HOMO is 73% localized on the dz^2 orbital of the metal center and the HOMO-1 is 70% localized on the donor ligand. The orbital parentage of the each LUMO is consentient throughout the series with the majority of the contribution originating from the $N_2N_2^q$ acceptor ligand in the order of **5.1** > **5.2** > **5.3**, and within a range of 59-49%. The energies calculated for the LUMO of each complex align well with the ground-state electrochemical potentials observed in Section 5.2.3, where the highest energy LUMO gave the most negative reduction potential. The metal-localized HOMO calculated for **5.2** and **5.3** is an unexpected result considering the trends observed in the electrochemical and spectroscopic data. Consequently, a closer look into the singlet excited-state manifold using TD-DFT calculations will be discussed in the next section.

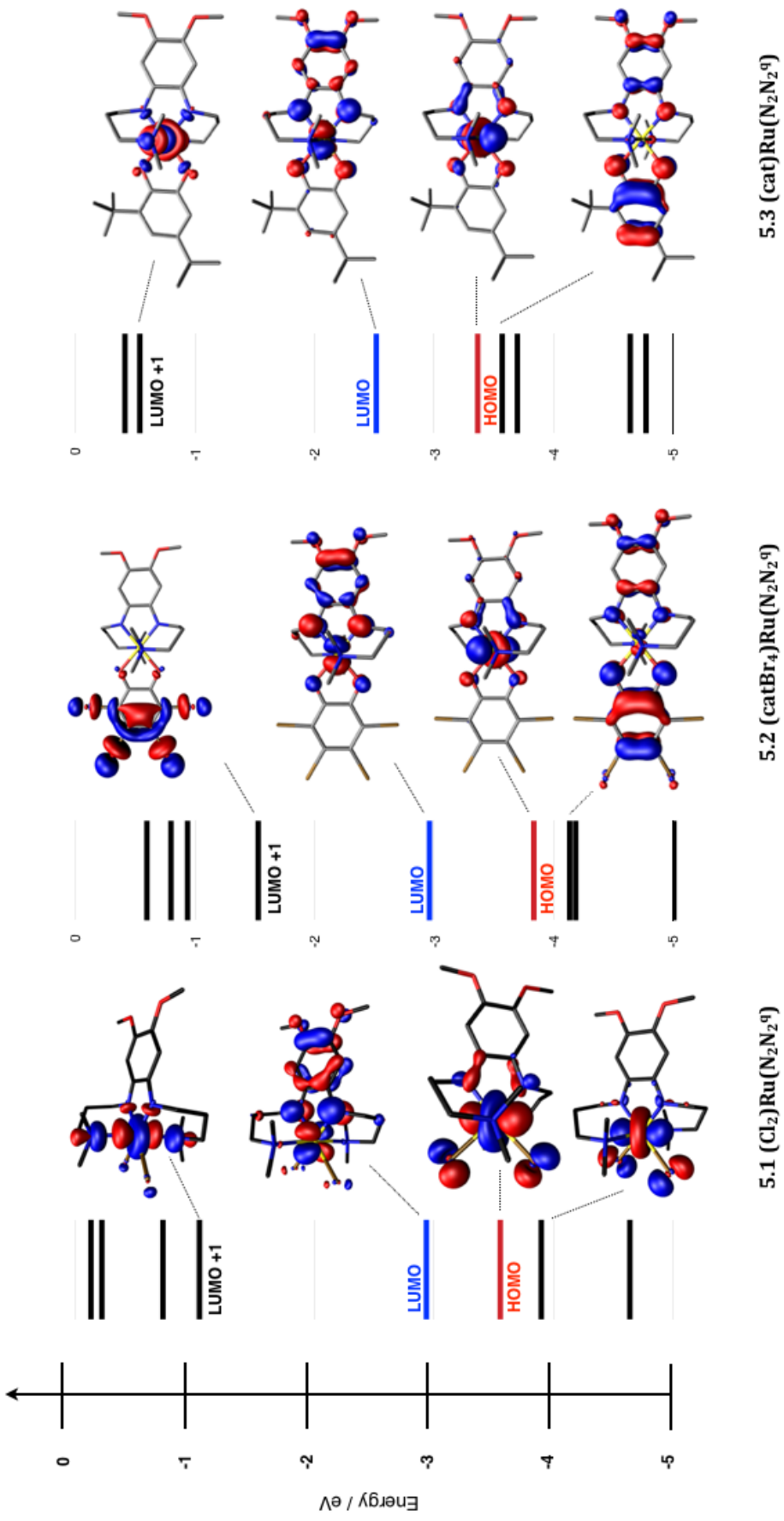

Figure 5.6 Frontier Kohn-Sham orbital diagram for $Ru(N_2N_2^q)Cl_2$, **5.1** (left), $(catBr_4)Ru(N_2N_2^q)$, **5.2** (middle), and $(cat)Ru(N_2N_2^q)$, **5.3** (right) as determined by DFT computations at the TPSS/TZVP level of theory.

5.2.5 TD-DFT

With the prerequisite ground-state calculations in hand, gas-phase time-dependent DFT (TD-DFT) calculations were employed to evaluate the characters and energies of the lowest-lying singlet excited-states of complexes **5.1-5.3.** The first five calculated transitions along with the first five transitions that gave the greatest oscillator strengths for each complex are listed in **Table 5-4**, along with their energies, transitions, and character. This information is also presented graphically for all calculated singlet excited-states in **Figure 5.6**. For all complexes, the two lowest energy transitions calculated are MLCT transitions, corresponding to the promotion of an electron from a metal-localized orbital to the empty π* orbital on the $N_2N_2^q$ acceptor ligand. In the absorption spectra neither of these low-energy MLCT transitions is observed, coinciding with the zero oscillator strength calculated for them; this is most likely due to the transition being Laporte forbidden.

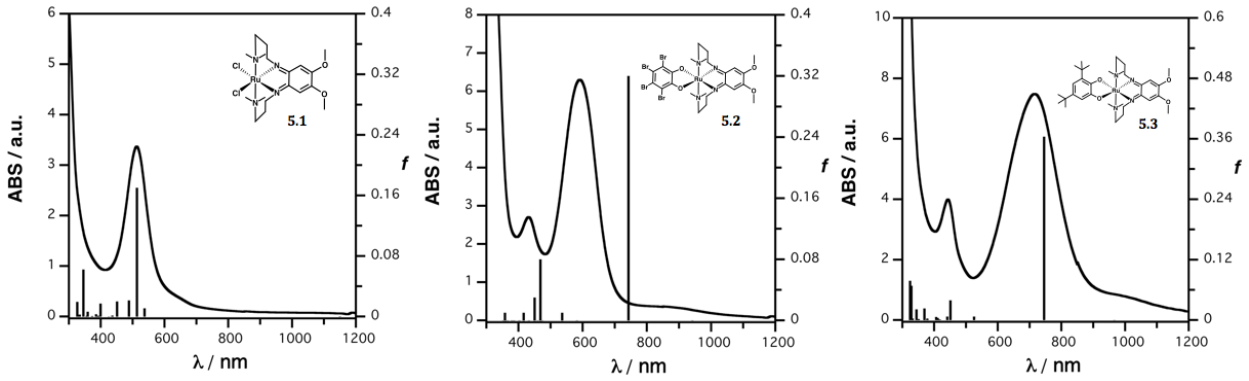

Figure 5.7 Calculated singlet excitations for **5.1** (left), **5.2** (center), and **5.3** (right) vs. oscillator strengths (*f*) overlaid against the normalized experimental spectra collected in THF at 298 K.

In general, the energies of the calculated transitions with the highest oscillator strengths agreed well with the experimental data in **Figure 5.6**. For complex **5.1** the transition that gave the highest oscillator strength is a mixture of two different transitions:

76% is HOMO-2 → LUMO and is MLCT in character and 24% is a HOMO → LUMO+2 transition that is d→d in character. This transition is calculated to fall at 513 nm and aligns perfectly with the experimental band maximum observed for **5.1**.

Table 5-4 Relevant Calculated Singlet Excited States for **5.1–5.3.**

	State	E/eV(nm)	f	$\Phi_O \rightarrow \Phi_U$	Character
5.1	1	0.67 (1862)	0	HOMO→LUMO	MLCT
	2	1.08 (1150)	0	HOMO-1→ LUMO	MLCT
	3	2.31 (537)	0.011	HOMO-3 → LUMO	LMCT
	4	2.42 (513)	0.169	HOMO-2 → LUMO (76%) HOMO → LUMO+1 (24%)	MLCT / d → d
	5	2.54 (488)	0.021	HOMO → LUMO+1 (70%) HOMO-1 → LUMO+1 (29%)	d → d
	6	2.75 (451)	0.019	HOMO-4 → LUMO	LLCT
	9	3.1 (400)	0.017	HOMO-4 → LUMO+4 (54%) HOMO-2 → LUMO+2 (41%)	LL′CT LL′CT
5.2	1	0.978 (1297)	0	HOMO → LUMO	MLCT
	2	1.32 (941)	0	HOMO-2 → LUMO	MLCT
	3	1.67 (742)	0.320	HOMO-1 → LUMO	LL′CT
	5	2.31 (535)	0.012	HOMO → LUMO+1	MLCT
	7	2.65 (468)	0.076	HOMO-2 → LUMO+1 (70%) HOMO-4 → LUMO (30%)	MLCT
	9	2.75 (450)	0.034	HOMO-4 → LUMO (55%) HOMO-2 → LUMO+1 (45%)	LLCT/MLCT
	11	2.98 (416)	0.005	HOMO-6 → LUMO	MLCT
5.3	1	0.95 (1302)	0	HOMO → LUMO	MLCT
	2	1.28 (966)	0	HOMO-2 → LUMO	MLCT
	3	1.66 (745)	0.364	HOMO-1 → LUMO	LL′CT
	5	2.74 (451)	0.039	HOMO-3 → LUMO (60%) HOMO → LUMO+1 (40%)	LLCT/ d → d
	13	3.35 (370)	0.023	HOMO-2 → LUMO+2(80%)	LL′CT
	18	3.78 (328)	0.068	HOMO-1 → LUMO	LL′CT
	20	3.83 (324)	0.078	HOMO-1→ LUMO+2	LL′CT

For complex **5.2**, the third excitation gave the strongest oscillator strength and corresponds relates to the promotion of an electron from the donor-localized HOMO-1 to the acceptor localized LUMO and therefore can be characterized as LL′CT. The energy of this transition is calculated to fall at 1.67 eV (742 nm). Although the strength of this

transition does align with the molar absorptivity of the experimental band maximum, the energy of the excitation is 0.4 eV lower than the transition observed in THF. It is worth mentioning that a strong ground-state dipole moment of 11 Debye is predicted for **5.2** and the inconsistency of the calculated vs. experimental LL′CT transition could be a result of using gas-phase TD-DFT calculations. The fourth and fifth calculated excitations are MLCT in nature and give negligible oscillator strengths; this is most likely due to the orbitals lacking the appropriate symmetry.

The calculated singlet excited-state manifold for **5.3** is dominated by a low-energy LL′CT transition. The third excited state is calculated to fall only 0.05eV from the experimentally observed band maximum. This transition is also calculated to originate from a pFMO that is primarily localized on the donor ligand (HOMO-1) to the LUMO, which is mostly acceptor in character.

5.3 Summary and Conclusion

The redox-active, tetradentate acceptor ligand, N,N′-bis-(3-dimethylamino-propyl)-4,5-dimethoxybenzene1,2-iminoquinone ($N_2N_2^q$), was paired with a Ru(II) ion to generate a series of six-coordinate donor-acceptor charge-transfer complexes. The $N_2N_2^q$ ligand occupies four out of the six coordination spheres of an octahedron, in a facial arrangement allowing for the incorporation of a catecholate donor ligand trans and coplanar to the redox-active diimine core. Similar to *ortho*-quinones ability to act as a two-electron oxidant, the $N_2N_2^q$ ligand was installed in its catecholate form: $[N_2N_2^{cat}]^{2-}$ where upon coordination to a $Ru(DMSO)_4Cl_2$ precursor in refluxing toluene, the ligand underwent a two-electron oxidation to generate, $Ru(N_2N_2^q)Cl_2$ (**5.1**). The mechanism behind this redox

reaction has not been determined. Regardless, installation of two different catecholate ligands, one electron-rich and the other electron-poor onto the dichloride precursor yielded (catBr$_4$)Ru(N$_2$N$_2^q$) (**5.2**) and (cat)Ru(N$_2$N$_2^q$) (**5.3**). X-ray quality single crystals of **5.1** and **5.3** confirmed the ruthenium ion is in the +2 oxidation state, coordinated to a fully oxidized N$_2$N$_2^q$ ligand and placed co-planar to a fully-reduced (cat)$^{2-}$ donor ligand. The spectroscopic data shows the energies of the charge-transfer bands are heavily dependent on the nature of the donor ligands and illustrates the influence of the donor ligand on the spectroscopic HOMO-LUMO gap. However, the electrochemical data suggests a HOMO localized on the ruthenium center and the DFT calculations support this observation by predicting, for each complex, a HOMO localized on the Ru(II) center and a LUMO localized mainly on the N$_2$N$_2^q$ acceptor ligand. TD-DFT calculations clarified the inconsistency between the spectroscopic and electrochemical HOMO-LUMO gap by revealing that any low-energy MLCT transitions yielded negligible oscillator strengths and although present in the molecule's excite-state manifold, do not contribute to the compound's absorption cross-section. In fact, the lowest energy transitions with the highest oscillator strengths of **5.2** and **5.3** are between the ligand-localized HOMO-1 and LUMO, aligning with the observed spectroscopic data and suggesting the lowest energy transitions are LL'CT in nature.

These new octahedral D-A Ru(II) charge-transfer complexes demonstrate that the tetradentate N$_2$N$_2^q$ acceptor ligand, when coordinated to a d^6 metal ion, allows for the co-planar installation of a redox-active donor ligand. Future studies should be conducted in order to further elucidate the nature of the lowest energy transition. Lifetimes should be measured for this dyes to see if exhibit suitable excited-states for bimolecular reactions.

Variable temperature emission studies as well as transient absorption spectroscopy will be helpful experiments to map out the complicated excited-state manifold. Thus far, our findings suggest that the optical and ground-state redox properties of dyes based on a d^6 metal ion and the N_2N_2 ligand can be tuned through ligand variation. This may open up new areas of research where, instead of a precious heavy metals, such as ruthenium, the earth abundant Fe(II) ion could be used to realized a truly robust and tunable earth abundant charge-transfer photosensitizer.

5.4 Experimental

General Considerations. All compounds and reactions reported below show various levels of air- and moisture-sensitivity; so all manipulations were carried out using standard vacuum-line, Schlenk-line, and glovebox techniques. Solvents were sparged with argon before being deoxygenated and dried by passage through Q5 and activated alumina columns, respectively. To test for effective oxygen and water removal, aliquots of each solvent were treated with a few drops of a purple solution of sodium benzophenone ketyl radical in THF. The reagent: $RuCl_3 \bullet nH_20$ (Sigma); tetrabromocatecholate, $(catBr_4)H_2$ (Sigma); and 3,5 di-*tert*-butyl-catecholate, $(cat)H_2$ (Strem) were reagent grade or better and used as received. The $[N_2N_2(cat)]H_2$ was prepared according to according to published procedures.[9]

Spectroscopic Measurements. NMR spectra were collected at 298 K on a BrukerAvance 400 MHz or 500 MHz spectrometer in dry, degassed, $CDCl_3$. ^1H NMR spectra were referenced to tetramethylsilane (TMS) using the residual ^1H impurities of the deuterated solvent. All chemical shifts are reported using the standard δ notation in parts

per million; positive chemical shifts are to a higher frequency of TMS. Electronic absorption spectra were recorded with a PerkinElmer Lamda 900 UV-vis-NIR Spectrometer using one-centimeter path-length cells at ambient temperature (20-24 °C).

Electrochemical Methods. Electrochemical experiments were recorded on a Gamry Series G300 potentiostat/galvanostat/ZRA (Gamry Instruments, Warminster, PA) using a 3.0 mm glassy carbon working electrode, a platinum wire auxiliary electrode, and a silver wire pseudo-reference electrode. Reversibility of a redox process was judged based on the ratio of the anodic to the cathodic current being close to unity (ipa/ipc ≅ 1) for a given process. Electrochemical experiments were performed at ambient temperature (20-24 °C) in a nitrogen-filled glovebox using THF solutions containing 1 mM analyte and 100 mM $[NBu_4][PF_6]$ as the supporting electrolyte. All potentials are referenced to $[Cp_2Fe]^{+/0}$ using ferrocene or decamethylferrocene (−0.49 V vs $[Cp_2Fe]^{+/0}$)[13] as internal standards. Ferrocene and decamethylferrocene (Acros) were purified by sublimation under reduced pressure and tetrabutylammonium hexafluorophosphate (Acros) was recrystallized from ethanol three times and dried under vacuum.

X-ray Data Collection and Reduction. X-ray diffraction data for all complexes were collected on single crystals mounted on either a glass fiber or a cryoloop and coated with oil. Data were acquired using a Bruker SMART APEX II diffractometer at 143 K using Mo Kα radiation (λ = 0.71073 Å). The APEX2[14] program package was used to determine unit-cell parameters and for data collection. The raw frame data were processed using SAINT[15] and SADABS[16] to yield the reflection data file. Subsequent refinement cycles were carried out using the SHELXTL program suite.[17] Analytical scattering factors for neutral atoms were

used throughout the analyses.[18] ORTEP diagrams were generated using ORTEP-3 for Windows.[19] Diffraction data for **5.1** and **5.3** is given in **Table 5-5.**

Table 5-5 Diffraction Data for Complexes **5.1** and 5.3**.**

	$Ru(N_2N_2^q)Cl_2$ **5.1**	$(cat)Ru(N_2N_2^q)$ **5.3**
empirical formula	$C_{18}H_{32}Cl_2N_4O_2Ru$	$C_{32}H_{52}N_4O_4Ru$
formula weight	508.44	657. 84
crystal system	Monoclinic	Triclinic
space group	$P2_1/c$	$P\bar{1}$
a/ Å	10.9873(4)	10.4646(11)
b/ Å	8.7036(3)	11.6441(12)
c/ Å	22.2278(8)	13.9539(15)
α/deg	90.00	97.9360(13)
β/deg	102.9678(4)	90.0901(13)
γ/deg	90.00	109.6263(12)
V /Å^3	2071.41(13)	1584.1(3)
Z	4.00	2.00
refl collected	24926	18812
indep refl	5209	7439
R_1	0.0328	0.0351
wR_2	0.0584	0.0779

Density Functional Theory Computations. Calculations were performed in the Molecular Modeling Facility in the Department of Chemistry at UC Irvine. Calculations were performed employing Meta-GGA functional TPSS.[20] Geometry optimizations were initiated using a split-valence plus polarization basis set (def2-SVP)[21] and further refined using the polarized triple-ζ basis set def2-TZVP.[22] Structures obtained from single-crystal X-ray diffraction experiments were used as the starting points for geometry optimizations; no molecular symmetry was imposed. Mulliken population analyses were obtained at TPSS/TZVP theory level; the contour values were 0.03 for the molecular orbital plots. All

calculations were performed using the quantum chemistry program package TURBOMOLE.[23,24]

Synthesis of $Ru(N_2N_2^q)Cl_2$ (5.1): Complex **5.1** was prepared by treating $Ru(DMSO_4)Cl_2$ (121 mg, 0.25 mmol, 1 equiv) with one equivalent of N,N′-bis-(3-dimethylaminopropyl)-4,5-dimethoxy-benzene-1,2-di-iminoquinone ($N_2N_2^q$) (85 mg, 0.25 mmol, 1 equiv) and excess triethylamine in refluxing toluene for two days to generate a dark red heterogeneous solution. Solid was separated from filtrate through filtration using glass frit. Subsequent washings with THF, ether, and pentane yielded **5.1** as a bright-red fine powder. The filtrate was collected, concentrated down to a saturated solution; pentane was added to yield a second crop of **5.1**. Layering a toluene solution of **5.1** with pentane grew X-ray quality crystals. (76 mg, 60% yield). ^{1}H NMR (400 MHz; $CDCl_3$) δ/ppm: 0.815 (br *s*, N-Me, 6H), 1.25 (br *m*, CH_2, 2H), 1.47 (br *m*, CH_2, 2H), 1.67 (br *s*, N-Me, 6H), 2.16 (br *m*, CH_2, 2H), 3.88 (*s*, -O-Me, 6H), 3.91 (*m*, CH_2, 2H), 4.61 (*m*, CH_2, 2H), 5.69 (*m*, CH_2, 2H), 6.92 (*s*, aryl–H, 2H), 4.61 (*d*, J=Hz, 2H), 5.23 (*q*, J=Hz, 4H), 6.73 (*s*, aryl-H, 2H), 7.32 (*s*, aryl-H, 1H), 7.91 (*s*, aryl-H, 1H). ^{13}C NMR (126 MHz; $CDCl_3$) δ/ ppm: 163.1 (*C*=N), 152.9 (*C*–O), 149.2 (aryl–*C*), 147.0 (aryl–*C*), 128.9 (aryl–*C*), 124.5(aryl–*C*), 124.2 (aryl–*C*), 122.3(aryl–*C*), 120.4 (aryl–*C*), 119.7 (aryl–*C*), 116.8 (aryl–*C*), 135.4 (–*C*(CH_3)$_3$), 130.3 (–C(*C*H_3)$_3$). UV-vis-NIR [THF; λ_{max}/nm (ε/M^{-1} cm^{-1})]: 520 (3350).

Synthesis of $(catBr_4)Ru(N_2N_2^q)$ (5.2). Complex **5.2** was prepared by treating a THF solution of $(catBr_4)H_2$ (106 mg, 0.25 mmol, 1 equiv) with KH (25 mg, 0.625 mmol, 2.5 eq) and stirred at room temperature, under a nitrogen atmosphere for 24 hours. The resulting pale yellow solution was filtered through a glass frit to remove unreacted KH and then immediately added – drop wise – to a THF solution of **5.1** (127 mg, 0.25 mmol, 1 equiv) and

stirred for two days. Upon addition of 2K(catBr$_4$), the reaction mixture turned from dark red to dark blue. After 48 hours of stirring, the reaction mixture was filtered through a glass frit to remove precipitated KCl and the filtrate was dried under vacuum. The residue was re-dissolved in benzene, and stirred for an additional 24 hours followed by a second filtration though a glass frit. The filtrated was dried under vacuum to yield **5.2** as a dark blue microcrystalline solid (163.4 mg, 76% yield). UV–vis–NIR [THF; λ_{max}/nm (ε/M^{-1} cm^{-1})]: 440 (2500), 600 (6500).

Synthesis of (cat)Ru(N$_2$N$_2$^{q}) (**5.3**). Complex **5.3** was prepared using the same method as **5.2** where (cat)H$_2$ (104 mg, 0.25 mmol, 1 equiv) was dissolved in THF and stirred with 2.5 equivalents of KH (25 mg, 0.625 mmol, 2.5 eq) followed by treatment with **5.1** (127 mg, 0.25 mmol, 1 equiv) to yield a dark green microcrystalline solid (164 mg, 81% yield). ^{1}H NMR (400 MHz; CDCl$_3$) δ/ppm: 0.185 (*s*, N-Me, 3H), 0.236 (*s*, N-Me, 3H), 1.27 (*s*, N-Me, 3H), 1.34 (*s*, *N*-Me, 3H), 1.68 (*s*, ^{t}Bu, 9H), 2.19 (*s*, ^{t}Bu, 9H), 3.40 (*s*, -O-Me, 3H), 3.44 (*s*, -O-Me, 3H), 3.98 (*m*, CH$_2$, 4H), 4.57 (*d*, J=Hz, 2H), 4.61 (*d*, J=Hz, 2H), 5.23 (*q*, J=Hz, 4H), 6.73 (*s*, aryl–H, 2H), 7.32 (*s*, aryl–H, 1H), 7.91 (*s*, aryl–H, 1H). ^{13}C NMR (126 MHz; d_8-THF) δ/ppm: 166.3 (*C*=N), 152.2 (*C*–O), 142.6 (aryl–*C*), 142.1 (aryl–*C*), 136.7 (aryl–*C*), 131.6 (aryl–*C*), 131.4 (aryl–C), 129.9 (aryl–*C*), 129.3 (aryl–*C*), 128.8 (aryl–*C*), 128.1 (aryl–*C*), 127.3 (aryl–*C*), 125.5 (aryl–*C*), 124.6 (aryl–*C*), 122.3 (aryl–*C*), 121.9 (aryl–*C*), 121.7 (aryl–*C*), 120.0 (aryl–*C*), 20.5 (*p*–*C*H$_3$), 17.9 (*o*–*C*H$_3$). UV–vis–NIR [THF; λ_{max}/nm (ε/M^{-1} cm^{-1})]: 328 (25 054), 1310 (9920).

5.5 References

(1) Cummings, S. D.; Eisenberg, R. *J. Am. Chem. Soc.* **1996**, *118*, 1949–1960.
(2) Kramer, W. W.; Cameron, L. A.; Zarkesh, R. A.; Ziller, J. W.; Heyduk, A. F. *Inorg. Chem.* **2014**, 140806135722006.
(3) Cameron, L. A.; Ziller, J. W.; Heyduk, A. F. *Chem. Sci.* **2016**, *7* (3), 1807-1814
(4) Herebian, D.; Bothe, E.; Bill, E.; Weyhermüller, T.; Wieghardt, K. *J. Am. Chem. Soc.* **2001**, *123*, 10012–10023.
(5) William B Connick; David Geiger, A.; Eisenberg, R. *Inorg. Chem.* **1999**, 38, 3264-3265.
(6) Sabatini, R. P.; Zheng, B.; Fu, W. F.; Mark, D. *J. Phys. Chem. A.* **2014**, 118, 10663-10672
(7) Masui, H.; Lever, A. B. P.; Auburn, P. R. *Inorg. Chem,* **1991**, *30*, 2402–2410.
(8) Haga, M.; Dodsworth, E. S.; Lever, A. B. P. *Inorg. Chem.* **2002**, *25*, 447–453.
(9) Szigethy, G.; Heyduk, A. F. *Inorg. Chem.* **2011**, *50*, 125–135.
(10) Alessio, E.; Mestroni, G.; Nardin, G.; Attia, W. M.; Calligaris, M.; Sava, G.; Zorzet, S. *Inorganic Chemistry* **1988**, *27*, 4099–4106.
(11) Pyle, A. M.; Chiang, M. Y.; Barton, J. K. *Inorg. Chem.* **1990**, *29*, 4487–4495.
(12) Brown, S. N. *Inorg. Chem.* **2012**, *51*, 1251–1260.
(13) N. G. Connelly, and W. E. Geiger, *Chem. Rev*., **1996,** 96, 877.
(14) APEX2 Version 2013.6-2, Bruker AXS, Inc.; Madison, WI 2013.
(15) SAINT Version 8.32b, Bruker AXS, Inc.; Madison, WI 2012.
(16) Sheldrick, G. M. SADABS, Version 2012/1, Bruker AXS, Inc.; Madison, WI 2012.
(17) Sheldrick, G. M. SHELXTL, Version 2014/7, Bruker AXS, Inc.; Madison, WI 2014.
(18) International Tables for Crystallography, A. J. C. Wilson, Ed.; Kluwer Academic, Dordrecht, Netherlands, **1992**, Vol. C.
(19) L. J. Farrugia, *J. Appl. Crystallogr*., **1997**, 30, 565.
(20) J. Tao, J. P. Perdew, V. N. Staroverov, and G. E. Scuseria, *Phys. Rev. Lett*., **2003**, 91, 146401.
(21) A. Schäfer, H. Horn, and R. Ahlrichs, *J. Chem. Phys*., **1992**, 97, 2571.
(22) A. Schäfer, C. Huber and R. Ahlrichs, *J. Chem. Phys*., **1994**, 100, 5829.
(23) TURBOMOLE V6.3, Turbomole GmbH, Karlsruhe, 2011. http://www.turbomole.com.
(24) F. Furche, R. Alrichs, C. Hättig, W. Klopper, M. Sierka and F. Weigend, WIREs *Comp. Mol. Chem*., **2014**, 4, 91.

Appendix I

Geometry Considerations for LL′CT Complexes

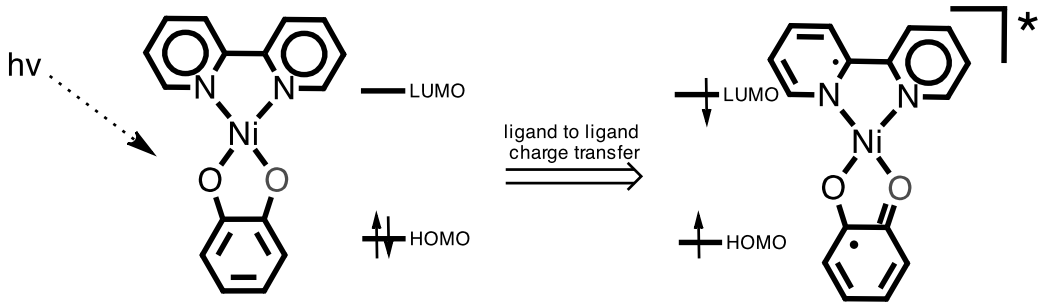

Figure A.1 General depiction of molecular dye displaying ligand to ligand charge transfer transition upon optical excitation.

A charge-transfer transition is the spatial redistribution of a compound's valence electrons upon optical excitation. The basic requirements for a charge-transfer transition in a molecule are as follows [1-8]

1) The HOMO and the LUMO are located on different parts of the molecule.
2) There is an asymmetric charge distribution in the ground state (or in the excited -state).
3) The HOMO and LUMO are (to an extent) delocalized such that there is a pathway for transition i.e, the overlap integral $\langle HO|LU\rangle \neq 0$

Requirements 1-3 are exemplified by the *Probability of transition:*

$$\mathbf{\langle \Psi_{(vib)}|\Psi_{(vib)}^{*}\rangle^{2} \langle \Psi_{(orbital)}|\mu(x,y,z)|\Psi_{(orbital)}^{*}\rangle^{2} \langle \Psi_{(spin)}|\Psi_{(spin)}^{*}\rangle^{2}}$$

Where $\langle \Psi_{(vib)}|\Psi_{(vib)}^{*}\rangle$ is the Frank-Condon factor, and governs the vibrational selection rule; $\langle \Psi_{(spin)}|\Psi_{(spin)}^{*}\rangle$ is the spin overlap integral that governs the spin selection rule; and $\langle \Psi_{(orbital)}|\Psi_{(orbital)}^{*}\rangle$ is the electronic orbital integral, which governs the symmetry selection rule, and $\mu_{(x,y,z)}$ is the dipole moment operator. All three integrals must be non-zero for transition to occur.[1-4]

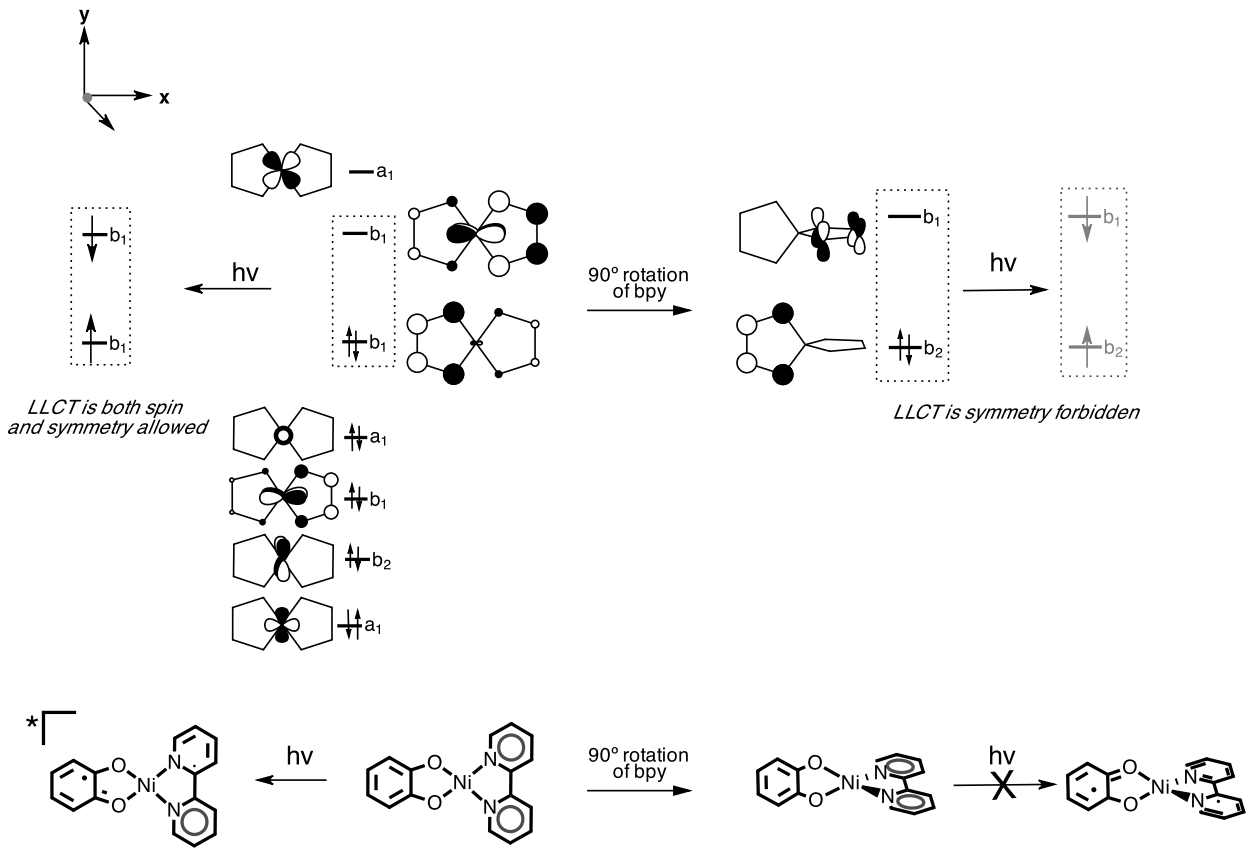

Figure A.2 Frontier molecular orbital diagram of square planar (donor)Ni(acceptor), *left*; tetrahedral, *right*. Symmetry labels taken from the C_{2v} point group.

Rationale behind dye design:

(Regarding parameters 1 and 2) Ligand-to-ligand charge transfer complexes have a ligand-localized donor HOMO and a ligand-localized acceptor LUMO that are in a fully reduced and oxidized form, respectively. This redox asymmetry provides an asymmetric electron configuration in the ground state.[6,9-12]

(Regarding parameter 3) Quantum mechanics states that the intensity (molar extinction coefficient) and rate of the optical transition is directly proportional to the amount of positive overlap of the donor and acceptor orbitals. The coplanar arrangement of the two bidentate ligands around the metal center resembles a conjugated electron

pathway and provides the delocalization needed to facilitate an optical transition. The purpose of the metal center is to electronically couple and physically fix the interacting π systems of the HOMO and the LUMO in a coplanar fashion so the torsional angle is as close to 0º as possible.[4,7] The symmetry selection rule shows the consequence of coplanar vs orthogonal ligand orbitals. [1-4, 13]

The symmetry of the excited state is given by the direct product of the symmetries of the partially occupied orbitals: $(HO)^2(LU)^0 \rightarrow (HO)^1(LU)^1$ so, $(HO)^1(LU)^1 = (b_1)^1(b_1)^1$ and $(b_1)^1 \times (b_1)^1 = {}^1A_1$ and ${}^3A_1$. The possible transitions are: ${}^1A_1 \rightarrow {}^{1,3}A_1$. ${}^1A_1 \rightarrow {}^3A_1$ violates the spin selection rule ($\langle \Psi_{(spin)} | \Psi_{(spin)}^* \rangle$) and therefore is forbidden. ${}^1A_1 \rightarrow {}^1A_1$ is spin allowed. The orbital selection rule: $\langle \Psi_{(orbital)} | \mu_{(x,y,z)} | \Psi_{(orbital)}^* \rangle$ states that an electronic transition is orbitally allowed if and only if the triple direct product contains the totally symmetric irreducible representation of the point group of the molecule: $\Gamma\, \Psi_{(orb)} \times \Gamma_{\mu(x,y,z)} \times \Gamma\, \Psi_{(orb)}^* = {}^1A_1 \times \Gamma_{\mu(x,y,z)} \times {}^1A_1$. The ${}^1A_1 \rightarrow {}^1A_1$ transition is orbitally-allowed because the triple direct product contains a_1 (z) for C_{2v}.

A rotation of one of the coplanar ligands 90º around the x axis (Figure 2 *right*) would make the two π systems orthogonal to one another. No longer coplanar, the delocalization of the π system is severed across the molecule leaving the HOMO localized solely on the donor ligand and the LUMO solely on the acceptor ligand. Although still spin allowed, this LL'CT transition violates the $\langle \Psi_{(orbital)} | \mu_{(x,y,z)} | \Psi_{(orbital)}^* \rangle$ selection rule: $(b_1)^2(b_2)^0 \rightarrow (b_1)^1(b_2)^1$ therefore ${}^1A_1 \rightarrow {}^{1,3}A_2$. Transition: ${}^1A_1 \rightarrow {}^3A_2$ is spin forbidden. ${}^1A_1 \rightarrow {}^1A_2$ is spin allowed, but fails the symmetry test because ${}^1A_1 \times {}^1A_2$ yields a_1, which is not a representation of x, y, or z in C_{2v} symmetry.

Ligand-to-ligand charge transfer complexes have a ligand-localized donor HOMO and a ligand-localized acceptor LUMO. The frontier π systems are fixed in a coplanar fashion and electronically coupled by the metal center. The redox sites of the complex reside on the ligands and therefore the metal based d orbitals must be moved out of the frontier orbital set to avoid low-energy, metal-based, excited states that can deactivate the desired charge transfer excited state. We achieve this by using a Ni(II) ion, whose low-spin d^8 electron configuration strongly favors a square planar geometries.[14]

A.1 References

(1) Gispert, J. R. *Coordination Chemistry*, Wiley: Weinheim, 2008.
(2) Miessler, G. L.; Tarr, D. A. *Inorganic Chemistry*, 4th ed.; Prentice Hill, 2011.
(3) Harris, D. C.; Bertolucci, M. D. *Symmetry and Spectroscopy: An Introduction to Vibrational and Electronic Spectroscopy,* 1st ed.; Dover Books on Chemistry, 1978.
(4) Turro, N. J.; Ramamurthy, V.; Scaiano, J. C. *Principles of Molecular Photochemistry: An Introduction,* 1st ed.; University Science Books, 2008.
(5) Balzani, V.; Bergamini, G.; Campagna, S.; Puntoriero, F. *Topics in Current Chemistry;* Springer Berlin Heidelberg: Berlin, Heidelberg, 2007; Vol. 280, pp. 1–36.
(6) Vogler, A.; Kunkely, H. *Comments on Inorganic Chemistry* **1990**, *9*, 201–220.
(7) Barbara, P. F.; Meyer, T. J.; Ratner, M. A. *J. Phys. Chem.* **1996**, *100*, 13148–13168.
(8) Sýkora, J.; Šima, J. *Coord. Chem. Rev.* **1990**, *107*, 1–212.
(9) Kramer, W. W.; Cameron, L. A.; Zarkesh, R. A.; Ziller, J. W.; Heyduk, A. F. *Inorg. Chem.* **2014**, 140806135722006.
(10) Vogler, A.; Kunkely, H. *Coord. Chem. Rev.* **2007**, *251*, 577–583.
(11) Vogler, A.; Kunkely, H.; Hlavatsch, J.; Merz, A. *Inorg. Chem.* **1984**, *23*, 506–509.
(12) Billig, E.; Williams, R.; Bernal, I.; Waters, J. H.; Gray, H. B. *Inorg. Chem.***1964**, *3*, 663–666.
(13) Benedix, R.; Hennig, H.; Kunkely, H.; Vogler, A. *Chem. Phys. Lett.* **1990**, *175*, 483–487.
(14) Cirera, J.; Alemany, P.; Alvarez, S. *Chem. Eur. J.* **2004**, *10*, 190–207.